Turbulent Taylor-Couette Flow based on LDV Measurement — Investigation on the Flow Field

by

Yicong Wang

A thesis submitted in partial fulfillment of the requirements for the degree of

Master of Science

Department of Mechanical Engineering
University of Alberta

Abstract

The flow structure in turbulent Taylor vortex flow (TTV) was investigated in Newtonian and shear-thinning fluids. The radius ratio of the investigated case is $\eta = 0.76$, and the aspect ratio of the experimental setup is 10.32.

First, detailed velocity measurements of the time-averaged azimuthal and axial components were performed with a Newtonian fluid (glycerin-water mixture). Radial profiles were obtained at the midheight of the cylinder, and axial profiles were obtained at three different radial positions. In $Re = 1100 \sim 3200$, all the results of the two velocity components showed the same periodicity in the axial profiles, indicating the ubiquitous existence of the Taylor vortex structure in TTV (Turbulent Taylor vortex flow). Radial jet flows resulted in the transport of angular momentum, and some differences in the vortex structure were also found by comparing TTV with TVF. The local Reynolds number was analyzed with the help of the radial profiles, and the rationality of an alternative definition of the Reynolds number was evaluated by considering the real local Reynolds number.

Similar measurements were performed for the aqueous solution of Xanthan gum, which is strongly shear thinning and weakly elastic, with two different concentrations. The results also revealed the Taylor vortex in the flow field in the investigated range. Unlike the Newtonian case, TTV with shear-thinning fluids exhibited different modes with ununified Taylor vortex wavelengths. For the case of low-concentration shear thinning, two distinctly different distributions were discovered in the radial profiles, which were directly resulted by the two opposite directions of the jet flow in different modes.

Preface

This thesis is an original work by Yicong Wang.

Acknowledgments

First, I would like to express my sincere gratitude to my supervisor, Dr.Brian Fleck. I appreciate his support and guidance throughout my three-year master program. His supervision style gives maximum freedom that makes me no longer a mere student but a self-responsible and motivated investigator, which would be a long-term benefit for me more than in acadamics.

I would like to thank my co-supervisor, Dr. David Nobes, for his generous support in my experimental work. Also, thanks to Dr.Guilherme Bessa, Dr.Lisa Kinsale, and other colleagues in the Optical Diagnostics Group for their warm-hearted help. Working with them was a valuable experience for me.

Thanks to my lovely friends who make my life in Canada memorable, and to Animenz, whose amazing work always reminds me of praticing.

Grateful appreciation to my parents for their unconditional support and indulgence. My gratitude for them is beyond words.

Last but not least, I would especially like to thank a very important person. I always feel like my time stops just before the pandamic. The Christmas of 2019 is the most precious treasure for me and I cherish every moment to be with you. Thanks for letting me know myself better and now I am much more determined. I truly hope that happiness will always accompany your future.

Table of Contents

List of Tables

List of Figures

List of Symbols

Constants

c	Speed of light.

Latin

$_{\theta,z,r}$	Azimuthal, axial and radial component
Δs	Separation between two measurement volumes
Δx	Displacement of the laser probe
$\vec{l}$	Direction of laser
$\vec{u}_p$	Velocity of the moving particle
$\vec{u}_s$	Velocity of the moving light source
a	Length of the measurement volume
C_θ	Correction factor
d	Width of the annulus
d_{mv}	Diameter of measurement volume
k	Flow consistency index
N	Number of fringes in measurement volume
n	Shear thinning index
R_i	Radius of the inner cylinder
R_o	Radius of the outer cylinder

s Displacement of the measurement volume

$U_{\theta,i}$ Azimuthal velocity of the inner cylinder

$U_{\theta,o}$ Azimuthal velocity of the outer cylinder

Greek

α_i Exit angle at the outer surface of the outer cylinder

α_o Incident angle at the outer surface of the outer cylinder

β_i Exit angle at the inner surface of the outer cylinder

β_o Incident angle at the inner surface of the outer cylinder

$\dot{\gamma}$ Shear rate (strain rate)

η Ratidus ratio

Γ Aspect ratio

λ_0 Initial wavelength of laser

λ_1 Wavelength of laser after reflection

μ Dynamic viscosity

μ_{ref} Viscoisty reference scale

ν_D Doppler frequency

ν_s Shift frequency

ν_0 Frequency of the inititial laser

ν_1 Frequency of the received laser

ω_θ Azimuthal angular velocity

$\tau_{r\theta}$ Stress tensor

θ Half of the included angle

Abbreviations & Acronyms

LDV Laser Doppler velocimetry.

MWVF Modulatec wavy vortex flow.

PIV Particle image velocimetry.

TC flow Taylor Couette flow.

TTV Turubulent vortex flow.

TVF Taylor vortex flow.

WVF Wavy vortex flow.

XG Xanthan gum.

Chapter 1

Introduction

1.1 Background and literature review

Taylor-Couette(TC) flow, the flow confined in the annulus between two concentric cylinders, with the inner andor outer inner cylinder(s) able to rotate. The earliest reference to TC flow can be traced back to Newton's *Principia* in 1667.

Maurice Couette announced his first instrument in 1890, which consisted of a pair of cylinders, the outer rotating and the inner suspended to measure torque. This instrument was thought to be the first viscometer, and a series of studies on viscosity was continued on the basis of that. Today, this viscometer with rotating cylinder is known as the Couette viscometer.

Almost 30 years later, G. I. Taylor published his paper in 1923, which discovered the existence of the "Taylor vortex" and presented the photograph for the first time using ink visualization.

In the common case and in the current study, the radius of the inner rotating cylinder is R_i, and R_o for the outer stationary cylinder. Then the radius ratio would be

$$\eta = R_i/R_o. \tag{1.1}$$

The annulus width d

$$d = R_o - R_i, \tag{1.2}$$

usually, it is much smaller than the axial length (or height) of the cylinder l.

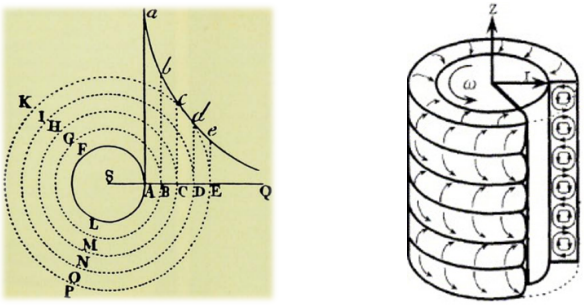

(a) (b)

Figure 1.1: Comparison between the basic laminar flow (a) as depicted by Newton in *Principia* in 1667 and (b) Taylor vortex flow as described by Taylor.

Therefore, the aspect ratio

$$\Gamma = l/d, \tag{1.3}$$

is much larger than 1 ($\Gamma >> 1$).z

The basic laminar TC flow, or may be called the circular Couette flow (CCF) in some papers, is defined as a stationary axisymmetric laminar flow with a purely azimuthal velocity field ($u_r = 0, u_\theta = u_\theta(r), u_z = 0$). All profiles of the basic laminar TC flow are functions of only the radial position r and are analytically accessible.

1.1.1 TC flow transition and Taylor vortex of Newtonian fluids

In [1], it is shown that as inertia dominates the flow over viscosity (larger Re), the basic laminar TC flow tends to be unstable, and Taylor vortices stacked along the axial direction appear. The common definition of the Reynolds number of an incompressible Newtonian flow is

$$Re = U_{\theta,i} d/\mu, \tag{1.4}$$

where μ is the kinematic viscosity of the fluid. Re_c would be denoted as the critical value of the onset of TVF. Burkhalter [2] conducted a detailed measurement of the wavelength and size of the Taylor vortex cell, with the help of the flow visualization method. The results showed that the Taylor vortex wavelength remains constant as long as it stays in TVF.

For a large radius ratio, TVF enters the wavy vortex flow (WVF) at $Re_s = 1.05Re_c$ ($\eta = 0.95$, $\Gamma = 60$, [3]). Coles experimentally studied the structure of TVF and WVF, and the bifurcation from TVF to WVF was discovered ([3, 4]). For $\Gamma \geq 40$, Re_s does not change obviously, but increases with a reduction of Γ below 40. The variation in azimuthal wavenumber could be observed with different approaches to Re_s [3–5]. Coles[3] also found that multiple stable flow states could be reached by a given Re, and the non-uniqe flow states are sensitive to the used setup. For a smaller radius ratio, $\eta < 0.75$, an apparent increase in Re_s is observed with decreasing η [6]. In this numerical work, $\Gamma = \infty$ was assumed. The results agree well with the experiments with large Γ. It should be noted that for the radius ratio $\eta < 0.75$, the variation in the axial wavelength of the vortices could be significant. The end effect in finite cylinders on the transition from TVF to WVF was also discussed. Especially for $\Gamma < 30$, the damping of the wavy flow could be quite significant.

Wereley[7] conducted the experiment of imposing pressure-driven flows on the TC flow. The velocity fields were drawn on the basis of PIV in the meridional plane. It is suggested that this combined flow is essentially the linear superposition of the TC flow and the imposed axial flow, at least for the TVF and WVF.

When Re increases further, the transition from WVF to modulated WVF, which is characterized by two incommensurate temporal frequencies [8]. As Re continues to increase, the flow soon becomes chaotic and turbulent [9], which is called the turbulent Taylor vortex flow (TTV).

1.1.2 TC flow of shear-thinning fluids

Shear-thinning behavior is a quite common characteristic among the various non-Newtonian fluids, which exhibits a non-linear decrease in viscosity with increasing shear rate. In polymer solutions, this behavior is pretty common when the polymer is above a certain concentration. At the same time, these solutions are also viscoelastic. However, in the current study, we focus only on shear thinning behavior, for which

elasticity does not dominate. As reported by [10], polymer solutions, such as the Xanthan gum solution, show significant shear thinning behavior, while the elasticity can be negligible.

In shear-thinning TC flow, the Reynolds number defined on the basis of Newtonian fluid eq. (1.4) needs modification: viscosity requires proper specification. Usually, the viscosity of the nominal mean shear rate across the annulus is the common choice. Therefore,

$$Re = U_{\theta,i} d/\mu_{ref} \tag{1.5}$$

where $\mu_{ref} = \mu(\dot{\gamma})|_{U_{\theta,i}/d}$.

Some researchers also used other different definitions of the Reynolds number. Masuda[11] used an average viscosity weighted by the squared shear rate. Guzel[12] used an average Reynolds number, which is defined as the radial average of the local Reynolds number through the annulus. Due to the lack of real profiles of the local Reynolds number, Elcicek[13] suggested using the profiles of the basic laminar TC flow to calculate the average Reynolds number as an approximation of Guzel's method[12]. Different selections of the reference viscosity to define the Reynolds number might simply be a matter of choice. However, it changes the conclusions regarding the effects of shear thinning and Reynolds number. Therefore, the definition of Reynolds number should always be clearly emphasized, especially in non-Newtonian flows.

The main difference in the basic laminar flow of the shear thinning fluid is characterized by stratification of the viscosity in the annulus. This stratification becomes much more significant with a stronger shear-thinning effect and a smaller radius ratio. These will also be discussed in detail later in this thesis.

Similarly to the Newtonian case, the onset of the instability of TC flow with non-Newtonian fluids was investigated by researchers at first. In shear-thinning fluids with negligible viscoelasticity, the mechanism of the onset of the instability is found to be the same as the Newtonian fluids, and also leads to axisymmetric counter-rotating Taylor vortices in pairs. However, the critical conditions of the shear-thinning TC flow

are still different, which are assumed to be the result of stratification of the radial viscosity and, therefore, the modified radial distribution of azimuthal velocity and shear stress. Coronado[14] indicated that Re_c in shear thinning fluids would decrease compared to the Newtonian case by theoretical predictions. The experimental results of Ashrafi[15], Alibenyahia[16] and Calgney[17], numerical results of Lockett[18] validate Coronado's prediction.

Concerning the Taylor-vortex structure in the TC flow, most of the work focused on the TVF regime: the theoretical results of Alibenyahia, Agbessi, Topayev[16, 19, 20], and the experimental results of Escudier, Cagney, Topayev[17, 20–22] indicate the considerable change resulting from the shear thinning effect. Escudier[23] conducted a detailed measurement of the Taylor vortex structure based on LDV. The velocity contours showed that the shear thinning effect leads to asymmetry in the Taylor vortex structure. Generally, in shear-thinning TVF: (1) radially, the vortex eye is closer to the inner cylinder, where the viscosity is lower due to viscosity stratification; (2) axially, the vortex eye is closer to the outward jet flow; (3) the strength of the vortices is weaker than that of Newtonian TVF.

Cagney[17, 22] combined PIV and flow visualization to investigate TC flow with xanthan gum solution. A series of experiments including Newtonian and three non-Newtonian fluids with various flow indices. The results indicated that the shear thinning effect was associated with an increase in the axial wavelength of the Taylor vortex.

More recently, Elcicek[13] experimentally investigated the effect of shear thinning on flow structure and transition thresholds from basic laminar TF to WVF. The working fluids are also Xanthan gum aqueous solutions, at 1000 ppm and 2000 ppm. A direct transition from TVF to modulated WVF is observed, and a non-axisymmetric mod is found.

1.1.3 Taylor vortex structure in turbulent Taylor vortex flow

In the turbulent regime of the TC flow, the Taylor vortex structure is found to be ubiquitous. Lewis[24] studied the statistics of velocity fluctuations in the TV flow for Re up to 5×10^5 for the only inner cylinder rotation TC flow. The results suggested that Taylor vortices remained even at their highest investigated Re. Lathrop[25] also observed Taylor vortices, but the flow structures seem to have disappeared at $Re = 1.22 \times 10^5$.

Koschmieder[26] measured the wavelengths of Taylor vortices in TTV (the length of a pair of adjacent Taylor vortices) at $\eta = 0.727$ and 0.896, and found that the wavelength was larger than that in TVF. The hot wire measurements for $\eta = 0.667$ by Smith[27] showed that Taylor vortices encircling the inner cylinder always dominated the flow for $Ta < 3 \times 10^5 Ta_c$. Where Ta is the Taylor number, Ta_c is the critical value at which the basic laminar TC flow transitions to TVF and $Ta = Re^2(\eta^{-1} - 1)$. It is also suggested that these Taylor vortices were superimposed on a background of irregular turbulent motions. Beyond $5 \times 10^5 Ta_c$, the Taylor vortices became fragmented and lost regularity, indicating that the flow became completely turbulent.

Barcilon[28] studied the flow structure of the TTV with flow visualization and observed a herringbone-shaped pattern of streaks at the outer cylinder wall. It is conjectured that these streaks were the inflow and outflow boundaries of Gortler vortices.

Several simulation studies have been carried out in turbulent regimes[29, 30]. More recently, Bilson[31] simulated at $Re = 3200$ with $\eta = 0.617$ using a second-order finite volume method. Dong[32] performed three-dimensional direct numerical simulations at $Re = 1000 \sim 8000$. The time-averaged velocity field clearly reveals the organized Taylor vortex structure underlying the turbulent flow in TTV, and the instantaneous flow is supposed to be a superposition of turbulent fluctuations on these organized structures. Taylor vortex structures were also observed, up to $Re \sim 10^6$[33, 34].

Therefore, it is clear from the above literature review that additional experimental work in TTV, especially with shear-thinning fluids, is needed to investigate the Taylor vortex structure in TTV and its influence on the flow field.

1.2 Objectives

The overall objective of this study is to investigate the turbulent Taylor vortex flow field of Newtonian fluids and shear thinning fluids, with $\eta = 0.76$. A series of LDV measurements were conducted with three different fluids: a Newtonian fluid (glycerin-water mixture), two shear thinning fluids (0.1 and 0.4 wt.% Xanthan gum aqueous solution) in the TTV regime.

The experiment consists mainly of two parts: (1) obtain the radial profiles at the midheight of the flow. In this part, the azimuthal velocity, shear rate, and viscosity radial profiles are obtained, and the distribution difference between Newtonian and shear thinning is analyzed; (2) obtain the axial profiles at three different radial positions. The axial profiles reveal the Taylor vortex structure and the radial jet flows in the flow. Different flow modes are observed, and they are found to have a direct connection with the different behaviors observed in the radial profiles.

1.3 Outline

This thesis is structured into five chapters as follows:

Chapter 1 (the current chapter) introduces the background of TC flow and some important work in history. The work related to Taylor vortex structure in TCF and TTV, with Newtonian and shear-thinning fluids, is then reviewed.

Chapter 2 provides an overview of the apparatus and methodology used in this study, including the TC flow setup, the LDV device, and the working fluids.

Chapter 3 focuses on the radial profiles of the flow. The discussion begins with the basic laminar TC flow to investigate the change caused by the shear thinning effect,

the radius ratio, and the rheology model. The results of the radial measurement of TTV are presented as profiles. Differences in radial profiles between Newtonian TTV and shear thinning are discussed.

Chapter 4 talks mainly about the axial profiles of the flow. The Taylor vortex structure is determined by the axial profiles, and different flow modes are observed. The relationship between the Taylor vortex structure and the distribution of velocity, turbulence strength, etc. is analyzed.

Chapter 2

Methods and apparatus

2.1 Experiment setup

2.1.1 Structure of Taylor-Couette setup

A Taylor-Couette (TC) setup with two concentric cylinders was used in the experiment. Two concentric cylinders were both made of transparent cast acrylic. The outer cylinder was stationary and had a radius $R_o = 7.9375$ cm. The inner cylinder connected to a shaft was rotational and had radius $R_i = 6.0325$ cm, height $L = 19.6$ cm. Therefore, the annulus width, radius ratio, and the aspect ratio of the TC chamber were $d = 1.9$ cm, $\eta = 0.76$ and $\Gamma = 10.32$, respectively. Both cylinders were made of transparent cast acrylic, which allowed direct observation and laser measurement. Burin 2006[35] observed an end effect caused by Ekman circulation, which became obvious for the cases with a small aspect ratio ($\Gamma < 10$), so a space of 4.25 cm, larger than the annulus gap, was provided between the two cylinders' bases to diminish this end effect.

The inner cylinder was fixed to the inner shaft by two stainless steel shaft collars. Two double-sealed ball bearings on the top and bottom plates separately supported the shaft. To avoid leakage, a graphite-reinforced polytetrafluoroethylene (PTFE) seal with good wear resistance and low friction coefficient was installed outside each ball bearing. The top plate and the outer cylinder were firmly held onto the bottom plate with threaded tie rods, and the bottom plate was fixed to the machine table

with bolts and nuts.

A tachometer was fixed on the top of the shaft to monitor the rotation speed of the inner cylinder, and at the bottom of the shaft it was connected to the shaft of a DC motor (*Amatek Inc.*) using an Oldham type shaft coupling (*Misumi Inc.*). A reaction torque sensor(*Futek Inc.*) was fixed beneath the motor to measure the torque acting on the inner cylinder. The schematic diagram of the setup structure is shown in Figure 2.1.

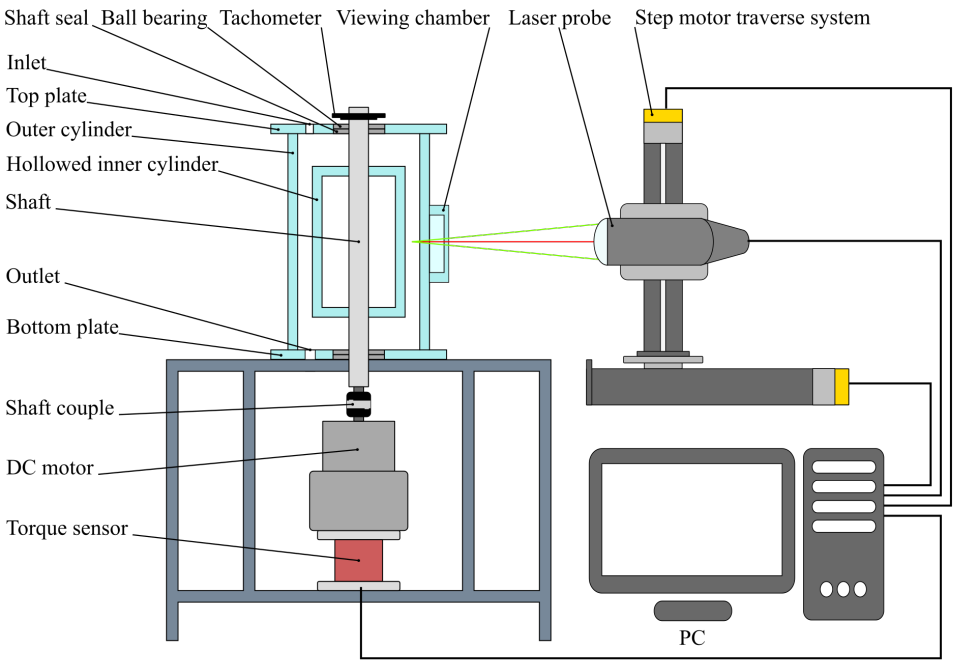

Figure 2.1: Schematic diagram of the setup.

2.1.2 Motor

A 3485-MAV5115 DC motor with speed control (*Amatek Inc.*) was used and its specifications are listed in Table 2.1. This motor incorporates a single-quadratic drive with closed-loop velocity control via the motor's internal Hall sensors, which help adjust the power to maintain at a certain speed. Therefore, this motor can provide the speed control of a DC motor with the convenience of an AC power supply.

Specification	Value (Unit)
Continuous torque	0.734 N·m
Input Current	4 Amps
Rated Speed	3450 RPM
Rated Power	265 watts
Frame size	NEMA 34
Shaft diameter	12.70 mm

Table 2.1: Specifications of the motor

2.1.3 Torque sensor

Compared with rotary torque sensors, reaction sensors do not require alignment or additional parts, such as bearings and slip rings. Therefore, in this study, a reaction torque sensor based on a strain gauge (FSH04381-TFF425, *FUTEK Advanced Sensor Technology, Inc.*) was selected to measure the torque in the inner rotational cylinder. Table 2.2 shows the relevant specifications for this device. The device was calibrated by FUTEK Advanced Sensor Technology, Inc. at 5 different points ranging from 0 to 7 N·m in both rotatory directions. The maximum system error of this device was reported to be 0.02% of the rated output.

An in-line USB digital amplifier and supplementary cable(USB220, 4Pin Lemo To Cable Assembly, *FUTEK Advanced Sensor Technology, Inc.*) were used for analog output voltage digitization and connection to a PC. It provided a sampling rate of up to 4800 Hz and up to 17.8 bits of noise-free resolution. Torque measurements were recorded using the SENSIT Test and Measurement software.

Specification	Value(Unit)
Rated Output(R.O.)	2 mV/V
Capacity	1000 in-oz
Hysteresis	$-0.2 \sim 0.2\%$ of R.O.
Nonlinearity	$-0.2 \sim 0.2\%$ of R.O.
Non-repeatability	$-0.05 \sim 0.05\%$ of R.O.
Output Resistance	350 Ω

Table 2.2: Specification of torque sensor

2.2 Laser Doppler Velocimetry

2.2.1 Introduction

Common traditional flow measurement methods

Measurements of the flow field are based on measurements of pressure or velocity. Traditionally, Pitot and Prandtl tubes have been used quite frequently for pressure measurements. However, this method is not applicable to obtain data from turbulence or other high-frequency flow fluctuations. Its poor response is mainly caused by the delay in the pressure signal in the tubes. Additionally, the transformation from measured pressure fluctuation to velocity fluctuation is not simple.

Compared to Pitot and Prandtl tubes for pressure, hot-wire anemometers are more widely used for direct velocity measurements. They measure the flow velocity of the heat transfer from the thin hot wire surface. This device is small in size and has a rapid response, allowing turbulent flows to be measured. However, the disadvantage is that the hot wire needs careful calibration before each experiment. Additionally, fragile hot wire cannot withstand high-speed flows or flows that contain hard materials. In addition, a joint shortcoming of the above traditional methods is that all of them require insertion into the flow, which means inevitable disturbances to the original flow field.

Laser methods and LDV

The development of laser techniques applied to flow measurement greatly improved the accuracy and informativity of the measurement results. Moreover, the integrated miniaturization of the laser measurement devices makes them easier to move and arrange, greatly expanding their applications. Among these laser measurement methods, Particle Image Velocimetry (PIV) and Laser Doppler Velocimetry (LDV) are the most widely used for velocity measurements.

Both methods require seeding particles suspended in the flow, but PIV illuminates the particles using a laser sheet and measures their displacements based on image processing to obtain the particles' corresponding velocities. PIV is efficient in visualizing the flow pattern, flow separation, and eddies while simultaneously providing quantitative measurement data, which is not possible by smoke or dye.

Laser Doppler Velocimetry (LDV) utilizing the Doppler effect could be the most effective and widely applied non-intrusive method in experimental investigations of flows and flow dynamics, usually with high accuracy[36].

2.2.2 Doppler Effect

As indicated by the name Laser Doppler Velocimetry, the Doppler effect is the basic principle behind this method and the technique is based on Doppler shift of the light reflected from a moving seeding particle.

This principle is depicted in Figure 2.2 where a moving light source and a fixed receiver are shown. According to the Lorenz-Mie scattering theory, light should be scattered in all directions at the same time, but here only the direction towards the receiver $\vec{l}$ is considered.

The initial distance between the light source point A and the receiver is s. The speed of the laser is c and the initial wavelength is λ_0. The time it takes for light to travel this distance is t, which means $s = ct$, and therefore the wavenumber along this distance is s/λ_0.

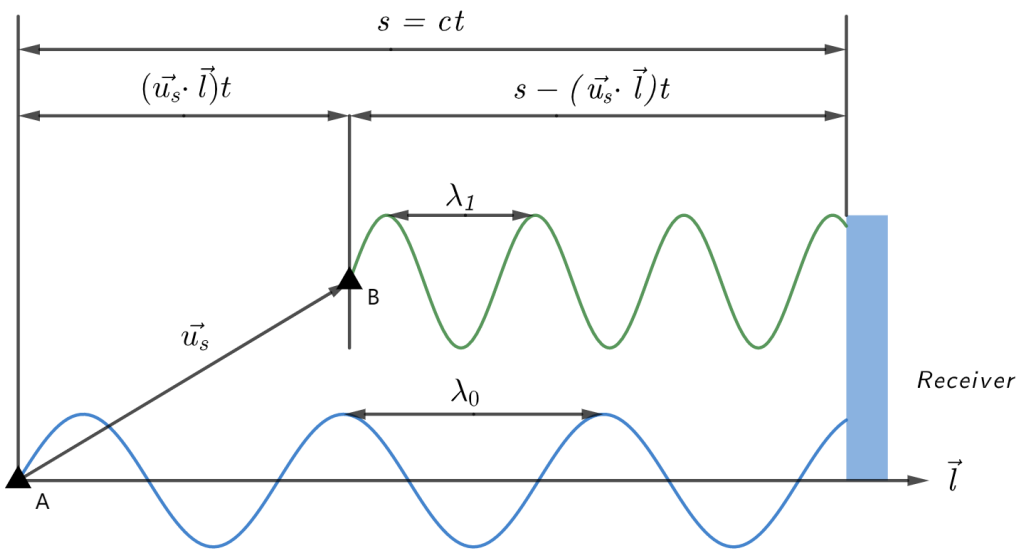

Figure 2.2: Schematic diagram of the Doppler effect with a moving light source.

Assuming that the light source is moving at a velocity of $\vec{u_s}$, the light source moves for a distance of $\left(\vec{u}_s \cdot \vec{l}\right) t$ and the rest distance is $s - \left(\vec{u}_s \cdot \vec{l}\right) t$. The light velocity is not relevant to the movement of the light source and is much higher than the movement velocity of the light source. Therefore, the wavenumber along this path remains constant. The wave seems to be squeezed, and the wavelength is shortened, from λ_0 to λ_1, as shown in the figure.

According to the constant wavenumber:

$$\frac{ct}{\lambda_0} = \frac{ct - \left(\vec{u}_\mathrm{s} \cdot \vec{l}\right) t}{\lambda_1} \tag{2.1}$$

yields the observed frequency ν_1 at the receiver:

$$\nu_1 = \nu_0 \frac{1}{1 - (\vec{u}_\mathrm{s}/c) \cdot \vec{l}} \tag{2.2}$$

Taking into account $\vec{u}_\mathrm{s}/c \ll 1$, Eq.2.2 could be simplified by only keeping the first two terms of the corresponding Taylor series as:

$$\nu_1 = \nu_0 (1 + \frac{\vec{u}_\mathrm{s}}{c} \cdot \vec{l}) \tag{2.3}$$

Similarly, if the light source is fixed while the receiver is moving, the observed fre-

quency has the same relationship when $\vec{u}_s$ is replaced by $-\vec{u}_r$ in Eq.2.3:

$$\nu_1 = \nu_0(1 - \frac{\vec{u}_\mathrm{r}}{c} \cdot \vec{l}) \tag{2.4}$$

In this study, a backward-scattering LDV system is used. This system consists of a fixed laser source, which also functions as a receiver. The laser with a frequency of ν_o is observed by a moving particle with a velocity of $\vec{u_p}$, and the observed frequency is ν_1. Then, part of the laser is reflected back to the stationary receiver in a certain direction $\vec{l_2}$, with a final received frequency of ν_2. The relationships between ν_o, ν_1 and ν_2 are shown below:

$$\nu_1 = \nu_0(1 - \frac{\vec{u}_\mathrm{p}}{c} \cdot \vec{l}_1) \tag{2.5}$$

$$\nu_2 = \nu_1(1 + \frac{\vec{u}_\mathrm{p}}{c} \cdot \vec{l}_2) \tag{2.6}$$

Substituting Eq.2.5 into Eq.2.6 yields the following.

$$\nu_2 = \nu_0(1 - \frac{\vec{u}_\mathrm{p}}{c} \cdot \vec{l})(1 + \frac{\vec{u}_\mathrm{p}}{c} \cdot \vec{l}_2) \tag{2.7}$$

This can be further simplified to a linear relation because $\vec{u_p}/1 \ll 1$ is always satisfied:

$$\nu_2 = \nu_0(1 - \frac{\vec{u}_\mathrm{p}}{c} \cdot \vec{l}_1 + \frac{\vec{u}_\mathrm{p}}{c} \cdot \vec{l}_2) \tag{2.8}$$

The final shifted frequency ν_2 is only a function of the velocity of the seeding particles, and Eq.2.8 is the basic formula of LDV. However, the shifted frequency ν_2 is in the order of 10^14 Hz and is too high to be measured effectively. In reality, the LDV system used in this study applied a dual-laser configuration to overcome this difficulty, which has become the standard of LDV instruments today. The related details will be described in the next section.

2.2.3 LDV principle of dual-beam configuration

Considering a dual-beam LDV configuration, two laser beams with the same frequency transmit in the direction of $\vec{l}_{1A}$ and $\vec{l}_{1B}$, respectively. The area where the two beams

intersect is the measurement volume, and the included angle between the two beams is 2θ, as shown in Figure 2.3. Particles passing the measurement volume scatter the light from both beams, but result in different Doppler effect shifted frequencies from each beam.

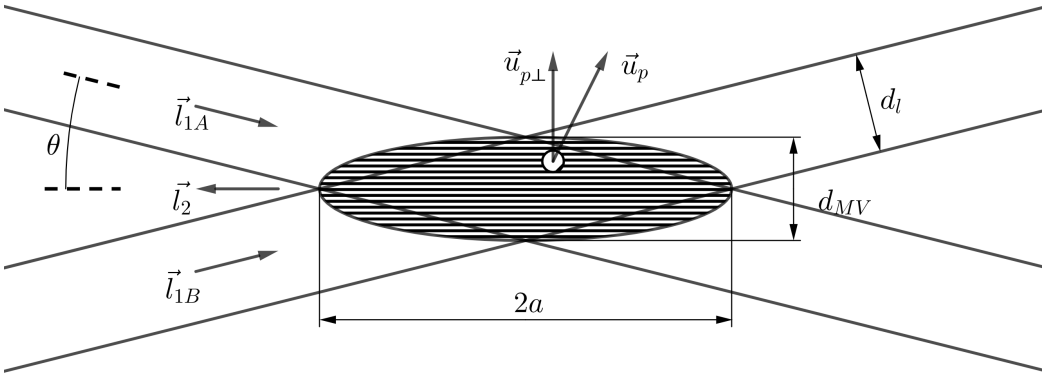

Figure 2.3: Measurement volume formed by the dual-beam configuration.

Assuming that a particle with velocity $\vec{u}_{p\perp}$ is crossing the measurement volume and part of the light is scattered in the direction of $\vec{l}_2$, which towards the receiver, the two frequencies detected by the receiver are given according to Eq.2.8 by:

$$\nu_{2A} = \nu_0(1 - \frac{\vec{u}_\mathrm{p}}{c} \cdot \vec{l}_{1A} + \frac{\vec{u}_\mathrm{p}}{c} \cdot \vec{l}_2) \tag{2.9}$$

and

$$\nu_{2B} = \nu_0(1 - \frac{\vec{u}_\mathrm{p}}{c} \cdot \vec{l}_{1B} + \frac{\vec{u}_\mathrm{p}}{c} \cdot \vec{l}_2) \tag{2.10}$$

The receiver detects a resultant light wave superimposed by the two waves mentioned above. This resultant light wave exhibits a low frequency, which is called the beat frequency, and equals the difference between the two composed waves. This beat frequency is called the Doppler frequency ν_D in the terminology of the LDV measurement technique and can be calculated by:

$$\begin{aligned} \nu_D &= |v_{2A} - v_{2B}| \\ &= \frac{v_0}{c} \left| \vec{u}_p \cdot \left(\vec{l}_{1A} - \vec{l}_{1B} \right) \right| \\ &= \frac{2 \sin\theta}{\lambda_0} u_{p\perp} \end{aligned} \tag{2.11}$$

This equation shows that the Doppler frequency is simply proportional to the particle velocity component, which is perpendicular to the bisector of the two incident beams. Furthermore, the measured Doppler frequency is independent of the position of the receiver. With the assumption that the particle exactly represents the velocity of the local flow, the velocity component can be obtained by measuring the Doppler frequency:

$$u_{\perp} = \frac{\lambda_0}{2\sin\theta}\nu_D \tag{2.12}$$

It is implied that there is no system calibration for LDV and the coefficient $2\sin\theta/\lambda_0$ is determined by the LDV specification and optical geometry.

However, the measured Doppler frequency described in this section is always positive and cannot deal with the velocity direction yet. A method to resolve this ambiguity will be discussed in the next section.

2.2.4 Frequency shift method for flow direction identification

To remove direction ambiguity from the Doppler frequency, the frequency of one laser beam is slightly shifted in each laser pair. This technique is widely applied and has become a standard[36]. This frequency shift is created by Bragg cells, which add a constant frequency shift of ν_s to the initial laser. This shift is set to be much lower than the laser frequency ν_o, while sufficiently higher than the Doppler frequency ν_D. For example, the frequency shift is 40 MHz in this study. Thus, this moderate shift now alters the frequency detected by the receiver:

$$\nu_{2A} = (\nu_0 + \nu_s)(1 - \frac{\vec{u}_{\mathrm{p}}}{c}\cdot\vec{l}_{1A} + \frac{\vec{u}_{\mathrm{p}}}{c}\cdot\vec{l}_2) \tag{2.13}$$

and ν_{2B} keeps the same as in Eq.2.10:

$$\nu_{2B} = \nu_0(1 - \frac{\vec{u}_{\mathrm{p}}}{c}\cdot\vec{l}_{1B} + \frac{\vec{u}_{\mathrm{p}}}{c}\cdot\vec{l}_2) \tag{2.14}$$

The current Doppler frequency is obtained as follows:

$$\nu'_D = \nu_s + \frac{v_0}{c}\left|\vec{u}_p\cdot\left(\vec{l}_{1A} - \vec{l}_{1B}\right)\right| + \frac{v_s}{c}\left|\vec{u}_p\cdot\left(\vec{l}_{1A} - \vec{l}_2\right)\right| \tag{2.15}$$

Taking into account $\nu_s \ll \nu_o$, the third term is negligible compared to the second term, and the second term exactly equals ν_D which yields:

$$\nu'_D = \nu_s + \nu_D = \nu_s + \frac{2\sin\theta}{\lambda_0} u_\perp \tag{2.16}$$

The velocity component of the flow is calculated as follows:

$$u_\perp = \Delta x(\nu'_D - \nu_s) \tag{2.17}$$

in which

$$\Delta x = \frac{\lambda_0}{2\sin\theta} \tag{2.18}$$

Therefore, the direction of the velocity can be determined by the sign of $\nu'_D - \nu_s$. Δx is also known as the fringe spacing of the measurement volume, a physical parameter formed by the interference of two overlapping light waves. In practice, the calculated fringe spacing can be used to assess the proper diameter of the particle. The particle diameter should be comparable to or smaller than the fringe spacing. Otherwise, large particles can still scatter light even if their centers are outside the measurement volume, leading to an undesired increase of the effective measurement volume[36]. In this study, the fringe space is approximately 2.5 μm, and particles with diameters, which are 2 μm, smaller than the fringe space are selected to avoid this effect.

2.2.5 Measurement volume size

The size of the measurement volume is finite relative to the measurement performance. Therefore, it is necessary to evaluate it properly. In general, the measurement volume created by the overlap of two crossing beams is approximated as an ellipsoid, as shown in Figure 2.3. The diameter of the measurement volume can be calculated by the diameter of the laser:

$$d_{\text{mv}} = \frac{d_l}{\cos\theta} \tag{2.19}$$

Similarly, the length of the measurement volume also depends on the diameter of the beam and the included angle:

$$2a = \frac{d_l}{\sin\theta} = \frac{d_{\mathrm{mv}}}{\tan\theta} \tag{2.20}$$

Moreover, the number of fringes in the measurement volume can be obtained from the measurement volume diameter and fringe spacing:

$$N = \frac{d_{\mathrm{mv}}}{\Delta x} = 2\frac{d_l}{\lambda_0}\tan\theta \tag{2.21}$$

2.2.6 Dantec LDV Device

With the development of the laser measurement technique, LDV systems have become integrated products that include transmitting and receiving units that are commercially available. A typical backward scattered Dantec LDV system used in this study is shown in Figure 2.4, and the work process is briefly described as follows.

The laser probe containing the Bragg cell and the optical front lens integrate both the transmitting and receiving functions. The laser from the fiber is split into a pair, and one of the beam's frequencies is shifted by the Bragg cell by 40 MHz to resolve the velocity directions. As a dual-component LDV system with the advantage of the integrated laser probe, the perpendicularity between two pairs of the laser beams and intersection of the measurement volumes are strictly guaranteed.

The light scattered backward by the particles passes through the front lens again and is collected by the photomultipliers, which convert the light signal into the electronic signal. Finally, the signal processor and the PC resolve the velocity of the electronic signal.

Considering the standard LDV system manufactured by Dantec, which is used in this study, several parameters like focal length, beam wavelength, and beam incident angle are determined by the pre-set optical configuration. Table 2.3 lists the relevant parameters of this system. However, refraction and other optical aberrations should

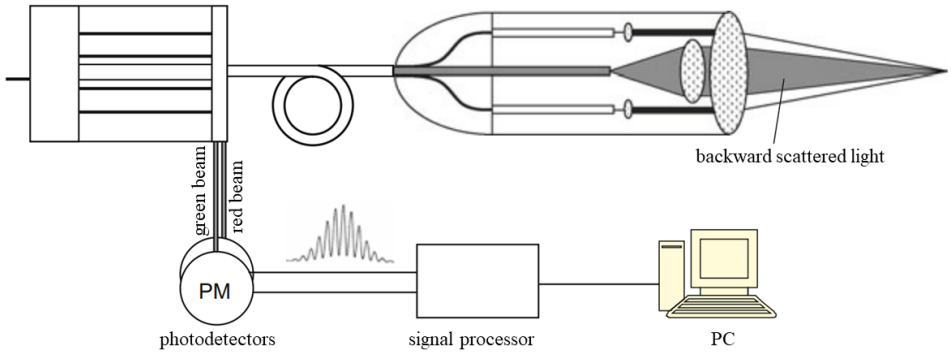

Figure 2.4: Schematic diagram of the *Dantec* backward scattering LDV system, modified from [36]

Figure 2.5: Picture of the integrated laser probe unit

be considered if the laser transmits multiple medium interfaces. This part will be described in Section 2.3

2.2.7 3-dimentional positioning of laser probe

To achieve accurate positioning and motion control of the laser probe and measurement volume, a 3-axis configuration positioning system was utilized. Three single-

Property	Value
Focal length f	160 mm
Wavelength of red beams λ_{red}	632.8 nm
Wavelength of green beams λ_{green}	532.0 nm
Gaussian beam diameter	2.2 mm
Beam separation 2d	38.4 mm
Beam intersection angle 2θ	13.54 degree
Beam waist radius	0.024 mm
Measurement volume diameter d_{MV}	0.05 mm
Measurement volume length $2a$	0.43 mm

Table 2.3: Optical configurations and geometry properties of measurement of the Laser probe (*Dantec Dynamics, Inc.*)

axis slides were assembled to provide movement in three directions (MN10–Precision Lead Screw, *BiSlide*, *Velmex, Inc*). Every slide was driven by a stepper motor(Vexta PK264, *Velmex, Inc*). A damper (D6CL-6.3F, *VEXTA, ORIENTAL MOTOR CO, LTD.*) was installed on each stepper motor to absorb the motor's vibration. All the motors were connected to one controller (VXM-3, *Velmex, Inc*) which enabled PC control.

2.3 Separation of measurement volumes

2.3.1 Separation of measurement volumes due to optical aberration

For a dual-beam configuration LDV system, each pair of laser beams travels through the setup's outer cylinder and intersects inside the working solution. During this process, each laser's direction altered 2 times, at the air-acrylic interface and the acrylic-solution interface, respectively.

Owing to the symmetrical condition of the laser light paths, only one beam and part of the geometry is considered here and drawn in the figures. Consider a pair of red

laser beams for measuring the circumferential velocity (u_ϕ), transmitting through the outer cylinder, as shown in Figure 2.6a. The two refraction interfaces are concentric cylindrical surfaces, shown as two concentric arcs in the schematic diagram of the cylinder's horizontal cross-section. Thus, the two incident angles (α_o and α_i in Figure 2.6a) all depend on the local position of the measurement volume inside the flow.

However, another pair of green laser beams to measure the axial velocity, as shown in Figure 2.6b, refracts at two parallel flat surfaces, shown as two parallel lines in the vertical cross-section in the figure. Therefore, the two incident angles α_o and α_i are always consistent (α_o and α_i in Figure 2.6b), and the shift of the real position is simply proportional to the displacement of the laser probe.

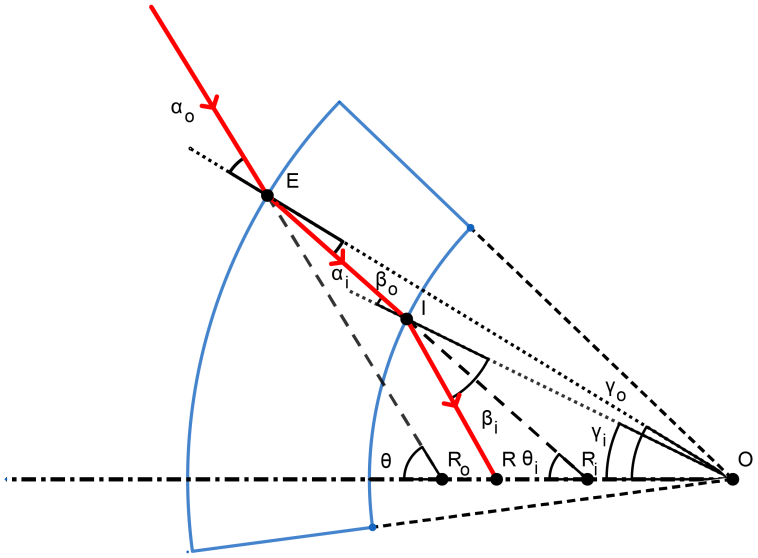

(a) Laser transmitting a cylinder in horizontal cross-section view

The relationship of the measurement volume shift and separation between the two pairs of beams could be obtained for the present case by the calculation described in the following:

For the red beams measuring the circumferential velocity component shown in Figure 2.6a), the laser incidents with the angle of α_o and refracted at points E and I, respectively. The measurement volume is then formed at the real intersection

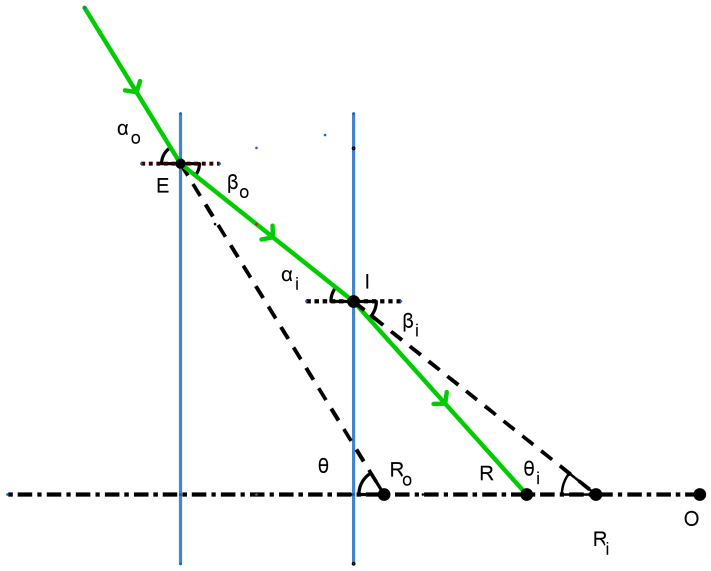

(b) Laser transmitting a cylinder in vertical cross-section view

Figure 2.6: Schematic diagram of the laser path. Only one beam and part of the geometry are shown in the figure, and θ does not represent the incident angle of the real laser beams.)

point R, on the symmetrical axis. The dashed lines are paths without refraction, and hence R_o and R_i are two virtual measurement volume positions formed by previous paths. $\triangle OER_o$ is easily obtained by the LDV probe. Applying the sine law yields the following:

$$\frac{\sin\beta_o}{OR_i} = \frac{\sin\theta_i}{OE} \tag{2.22}$$

$$\frac{\sin\gamma_i}{IR_i} = \frac{\sin\theta_i}{OI} \tag{2.23}$$

$$\frac{\sin\beta_i}{OR} = \frac{\sin(\beta_i+\gamma_i)}{OI} \tag{2.24}$$

in which,

$$\theta_i = \theta - \alpha_o + \beta_o$$

$$\gamma_i = \theta_i - \alpha_i$$

The Snell's Law in this case is given by:

$$n_{air} \sin \alpha_o = n_{acrylic} \sin \beta_o \tag{2.25}$$

$$n_{acrylic} \sin \alpha_i = n_{solution} \sin \beta_i \tag{2.26}$$

These equations provide basic solutions to the real position of the measurement volume and the measurement volume shift (R_oR). For given virtual measurement volume positions OR_o, the calculation process can be performed in this sequence:

$$ER_o \Longrightarrow OR_o \Longrightarrow OR_i \Longrightarrow IR_i \Longrightarrow OR \Longrightarrow R_oR \tag{2.27}$$

The green beams that measure the axial velocity component are shown in Figure 2.6b, because the incident angles are consistent, the relationship between the virtual measurement volume position and the real measurement position is easily obtained. Similarly, we apply the sine law again:

$$\frac{ER_o}{\sin \theta_i} = \frac{R_iE}{\sin \theta} \tag{2.28}$$

$$\frac{R_iI}{R_iE} = \frac{ER_o \cos \theta - (R_o - R_i)}{R_iE \cos \theta} \tag{2.29}$$

$$\frac{RR_i}{\sin(\beta_i - \alpha_i)} = \frac{R_iI}{\sin \beta_i} \tag{2.30}$$

in which,

$$\theta_i = \beta_o$$

The Snell's Law in this case is given by:

$$n_{air} \sin \alpha_o = n_{acrylic} \sin \beta_o \tag{2.31}$$

$$n_{acrylic} \sin \alpha_i = n_{solution} \sin \beta_i \tag{2.32}$$

The basic calculation process sequence is as follows:

$$ER_o \Longrightarrow IR_i \Longrightarrow RR_i \Longrightarrow R_oR \tag{2.33}$$

2.3.2 Compensating method of the separation measurement volumes

According to the previous section, the two measurement volumes separate due to different refraction geometries, and this situation deteriorates as the measurement volumes approach the inner rotating cylinder.

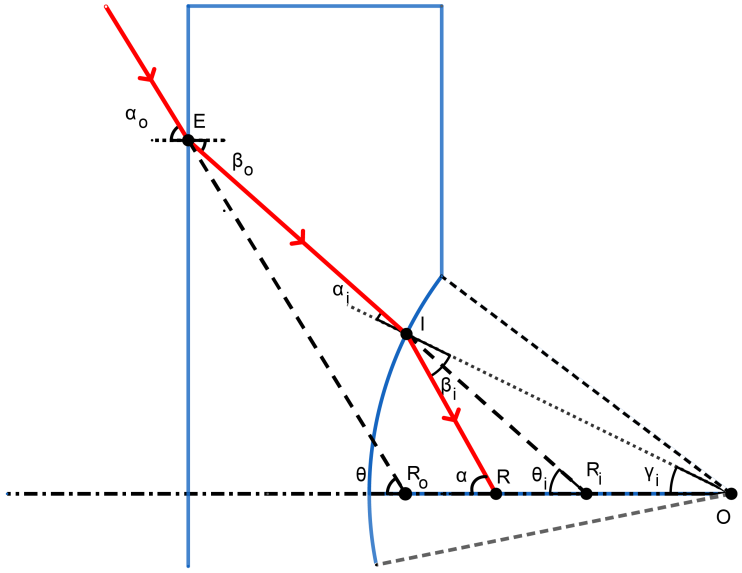

Figure 2.7: Laser transmitting a cylinder with flat outer surface in horizontal cross-section view

To compensate for this optical aberration caused by curved interfaces in the horizontal direction, Zhang[37] suggested modifying the outer surface of the cylinder to be flat, as shown in Figure 2.7. In addition to reducing the separation between two measurement volumes, this method also simplifies the calculation of the real measurement volume position. Compared to Figure 2.6a, the outer interface is modified to be flat, while the inner interface remains the same as the original. According to the sine law:

$$\frac{ER_o}{\sin\theta_i} = \frac{R_iR_o}{\sin(\alpha_o - \theta_o)} \tag{2.34}$$

$$\frac{RR_i}{\sin(\beta_i - \alpha_i)} = \frac{IR_i}{\sin(\beta_i - \alpha_i + \theta_i)} \tag{2.35}$$

and cosine law:

$$IR_i{}^2 = OI^2 + OR_i{}^2 - 2\cos(\pi - \theta_i)OI \cdot R_iO \tag{2.36}$$

also:

$$\sin\gamma_i = \frac{IR_i \sin\theta_i}{OI} \tag{2.37}$$

in which:

$$\theta_i = \beta_o \tag{2.38}$$

$$\alpha_i + \gamma_i = \theta_i \tag{2.39}$$

$$n_{air}\sin\alpha_o = n_{acrylic}\sin\beta_o \tag{2.40}$$

$$n_{acrylic}\sin\alpha_i = n_{solution}\sin\beta_i \tag{2.41}$$

The sequence of the calculation process in this case is as follows:

$$ER_o \Longrightarrow R_oR_i \Longrightarrow OR_i \Longrightarrow IR_i \Longrightarrow \gamma_i \Longrightarrow RR_i \Longrightarrow R_oR \tag{2.42}$$

To evaluate the compensating effect of the flat outer surface, Figure 2.8 compares the position of the measurement volume s of each pair of beams as a function of the displacement of the laser probe Δx. It is observed that the curve of the original horizontal beams' measurement volume (red dashed line) has a larger divergence compared to the other two curves.

Figure 2.9 shows the real position of the measurement volume inside the flow of the original green beams and the compensated red beams (dashed line), and the

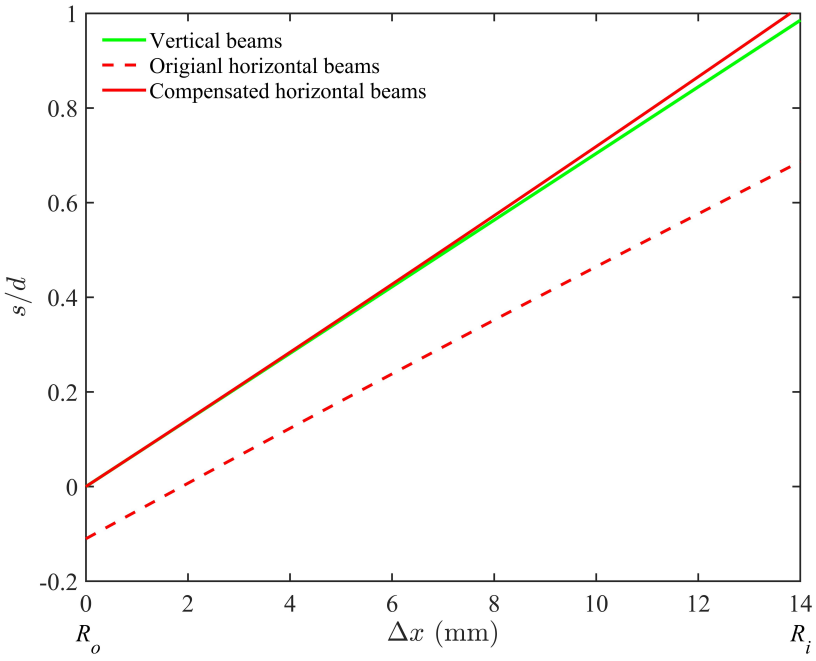

Figure 2.8: Real measurement volume position versus displacement of the laser probe. The position s is normalized by the annulus width d. The negative value of the position means that the horizontal measurement volume is inside the transparent wall with respect to the position of the laser probe. With increasing displacement of the probe Δx, the measurement volumes move from the outer cylinder R_o to the inner cylinder R_i.

original red beams (solid line). In the original case, the two measurement volumes never coincide due to the finite thickness of the cylinder. The separation distance ranges from 11.1% to 30.0% of the annulus width. However, the separation distance is compensated well when a flat outer surface is provided. Specifically, the maximum value is restricted to 2.9% of the width of the gap, validating a good compensating result.

Additionally, by decreasing the magnitude of the optical aberration, this compensating method also decreases the dislocation of the laser beam waists from the measurement volumes. Therefore, the light intensity in the measurement volume is also improved, which contributes to better signal quality, especially in xanthan gum aqueous solutions, which are not fully transparent.

However, it should be mentioned that the compensating method cannot completely

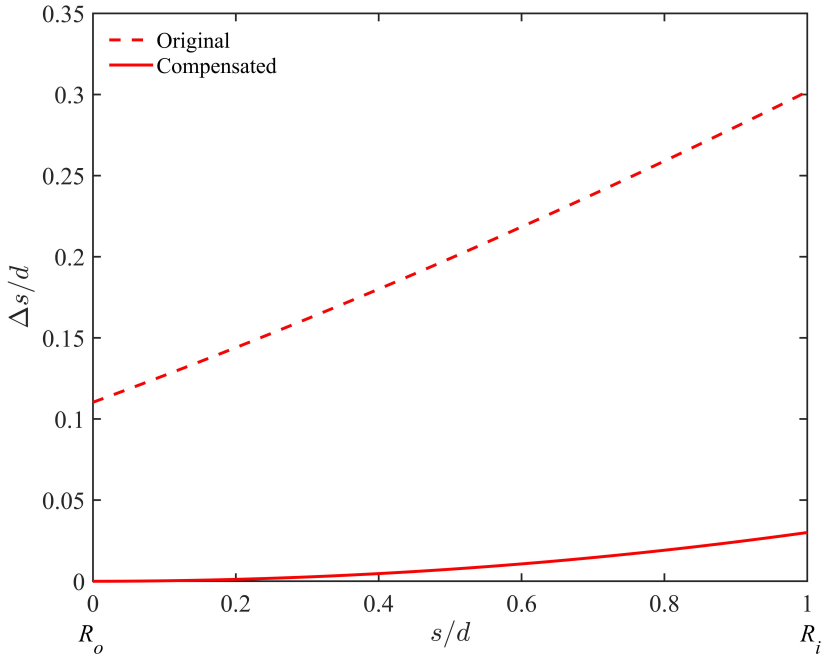

Figure 2.9: Separation between the measurement volumes versus the measurement volume position of the green beams (the green beams measure the axial velocity in the vertical cross section). Separation Δs is normalized by the annulus width d.

eliminate the measurement volume separation, and the two pairs of beams do not intersect at one unique point in the flow. Consequently, the results of the measurement of the two velocity components should still be treated individually.

2.3.3 Correction factor for azimuthal measurement result

According to the LDV principle, the flow velocity is obtained by measuring the Doppler frequency ν_d as follows:

$$|u| = \frac{\lambda_0}{2\sin\theta}\nu_d \tag{2.43}$$

If the laser beams are transmitted through flat surfaces (see Figure 2.6b), and invoking Snell's law, Eq.2.43 yields Eq.2.44

$$\frac{f_d}{2\,|u|} = \frac{\sin\theta}{\lambda_{air}} = \frac{\sin\beta_i}{\lambda_{solution}} \tag{2.44}$$

where λ with subscripts *air* and *solution* represent the laser wavelength in the corresponding medium and β_i equals the actual incident angle in this figure.

This means that when both interfaces are parallel flat surfaces, the effect of different refractive indices is canceled out by the change in wavelength. Therefore, the measurement results of u_z do not require correction.

However, for the case of curved surfaces, such as Figure 2.6a and Figure 2.7, Eq.2.44 is no longer applicable and a correction factor is needed for the measurement results of u_ϕ. As shown in Figure 2.7, this correction factor C_θ can be obtained as follows.

$$C_\theta = \frac{u_\theta}{u_{\theta,measured}} = \frac{n_{air}\sin\theta}{n_{solution}\sin\alpha} \tag{2.45}$$

In Eq.2.45, knowing the real incident angle α as a function of the position of the real measurement volume is a prerequisite to calculate the correction factor. This could be easily done in Section 2.3.2. The correction factor is depicted as a function of the normalized position of the measurement volume (s/d) in Figure 2.10.

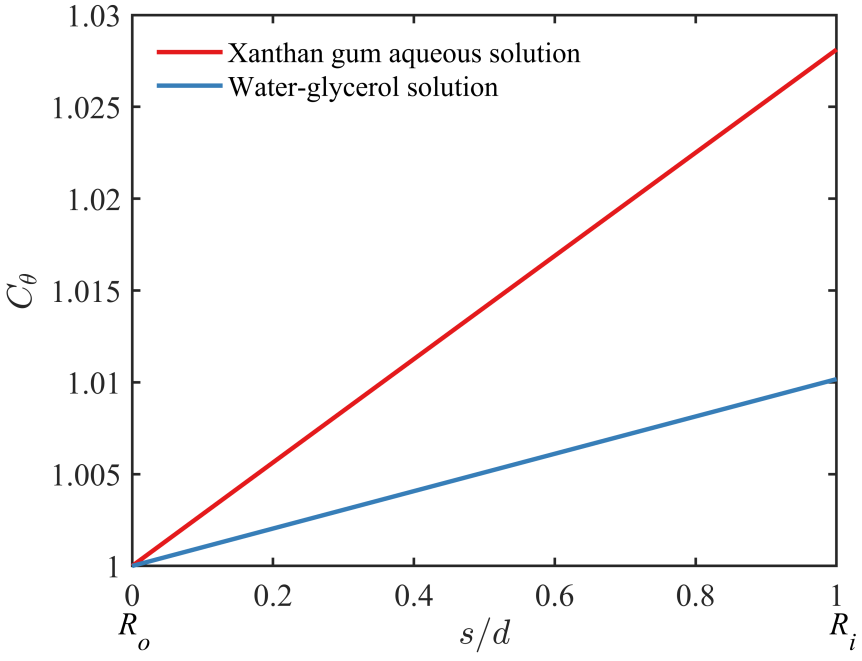

Figure 2.10: Correction factor C_θ as a function of the normalized measurement volume position s/d by Eq.2.45

In the figure, the velocity u_ϕ should be corrected for by up to 2.7% and 1.0% when the working solution is an aqueous solution of xanthan gum and a solution of water and glycerol, respectively. Furthermore, the correction factor is much lower than it in [38] (C_θ from 3% to 9%) where the horizontal beams were not compensated, which validates another advantage of our compensating method.

2.3.4 Viewing chamber

To provide a flat outer surface for the laser beam, a 3D printed clear resin-based viewing chamber was printed shown in Figure 2.11. One side of this unit has a curved surface that matches the outer radius of the cylinder. Therefore, the two parts can fit perfectly together when this unit was fixed to the cylinder with silicone glue. Additionally, a piece of 1/8 inch acrylic sheet was cut and attached to the chamber surface by bolts. To fill the hollow center space of this chamber, a 70.8 wt.% KSCN aqueous solution was prepared. The refractive index of this solution was measured to be 1.49 using an Abbe refractometer (ABBE-3L, *BAUSCH & LOMB*), similar to the refractive index of the acrylic sheet and the acrylic cylinder. The refractive indices of other materials were also measured and listed in Table 2.4

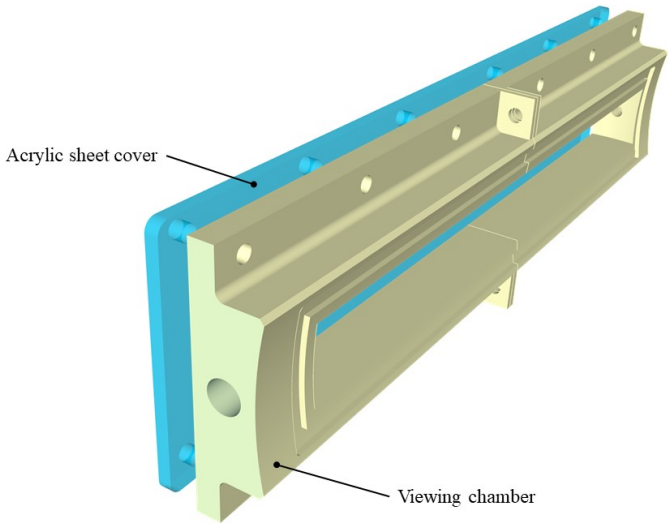

Figure 2.11: Viewing chamber and acrylic sheet cover modeling.

Material	Refractive Index (n)
0.1 wt.% xanthan gum aqueous solution	1.333
0.4 wt.% xanthan gum aqueous solution	1.333
70.0 wt.% glycerol aqueous solution	1.429
70.8 wt.% KSCN aqueous solution	1.491

Table 2.4: Refractive index list

As shown in Figure 2.12, a tube of the same material as the cylinder was partially immersed in water and the prepared KSCN solution. In Figure 2.12b, the lower part of the tube immersed in the KSCN solution was almost invisible, showing a good refractive index matching between the solution and the cast acrylic. From the aspect of the laser refraction on interface, the viewing chamber could be regarded as a whole with the cylinder. Therefore, a flat surface could replace the curved outer surface of the cylinder, effectively reducing the separation between two measurement volumes.

(a) Immersed in water

(b) Immersed in KSCN solution

Figure 2.12: Comparison for the refractive index matching between the cast acrylic and KSCN solution

2.4 Working fluids

2.4.1 Preparation of the working fluids

The working fluids were one 70.0 wt.% water-glycerol solution and two xanthan gum aqueous solutions of 0.4 wt.% and 0.1wt% respectively. A mixture of deionized water and glycerol (USP, *Kosher*) was used to study the Newtonian case. The shear thinning effect was studied using a food grade Xanthan gum powder (CASRS: [11138-66-2],*Chemical Store Inc.*) at two different concentrations. However, xanthan gum molecules are sensitive to bacteriological degradation. Therefore, benzoic acid with a concentration of 0.04 wt.% was added to the solution as a preservative. The addition of benzoic acid does not have an apparent effect on the rheological characteristics of the solution. Each solution was prepared in batches of 4 kg. The raw materials were well mixed using a laboratory mixer (AM120Z-H, *XZB Inst & Eqpt. Co., Ltd*) to ensure fully dissolved solutions. To avoid bubbles appearing inside the working solutions and affecting LDV measurements, we degassed them in a vacuum chamber before adding them to the setup chamber for experiments. To improve the quality of the LDV measurement signal, silver-coated 2.0 μm diameter spherical particles with a very small amount were added to the working solutions.

2.4.2 Rheological models and measurement of the fluid characteristic

Xanthan gum aqueous solutions exhibit shear thinning behavior and a Newtonian plateau, which are typical of polymer solutions. In this study, two mathematical models are used that describe the relationship between shear stress and shear rate of non-Newtonian fluids.

First, the simplest and most widely used model, the Power Law Model, with the form of:

$$\mu = k\dot{\gamma}^{n-1} \tag{2.46}$$

is fitted to the shear thinning region, where k $[m^2/s]$ is the flow consistency index, n is the shear thinning index, $\dot{\gamma}$ is the strain rate, and $\dot{\gamma} = d\gamma/dt$ $[s^{-1}]$. For $0 < n < 1$, the fluid shows a shear thinning behavior, and a lower value of n represents a stronger degree of shear thinning. For $n > 1$, the fluid shows a shear thickening behavior and $n = 1$ means a Newtonian behavior. Apparently, the degree of shear thinning increases with the concentration of xanthan gum, as qualified by n(Power) in Table 2.5. Furthermore, the Power Law model could fit only well in the shear rate range of $10^0 \sim 10^2$. Beyond this range, the fittings gradually deviate from the Newtonian plateau.

Furthermore, the Carreau model, a four-parameter model, is used to describe the whole rheology curve, especially the Newtonian plateau. The formulation is given as follows:

$$\mu = \mu_\infty + (\mu_0 - \mu_\infty)\left[1 + (\lambda\dot{\gamma})^2\right]^{\frac{n-1}{2}} \tag{2.47}$$

where μ_∞ and μ_0 are the viscosities at an infinitely high shear rate and a zero shear rate, respectively. λ $[s]$ is a time constant and n is the power index.

Ideally, the flow index n in two models should be the same for one flow.

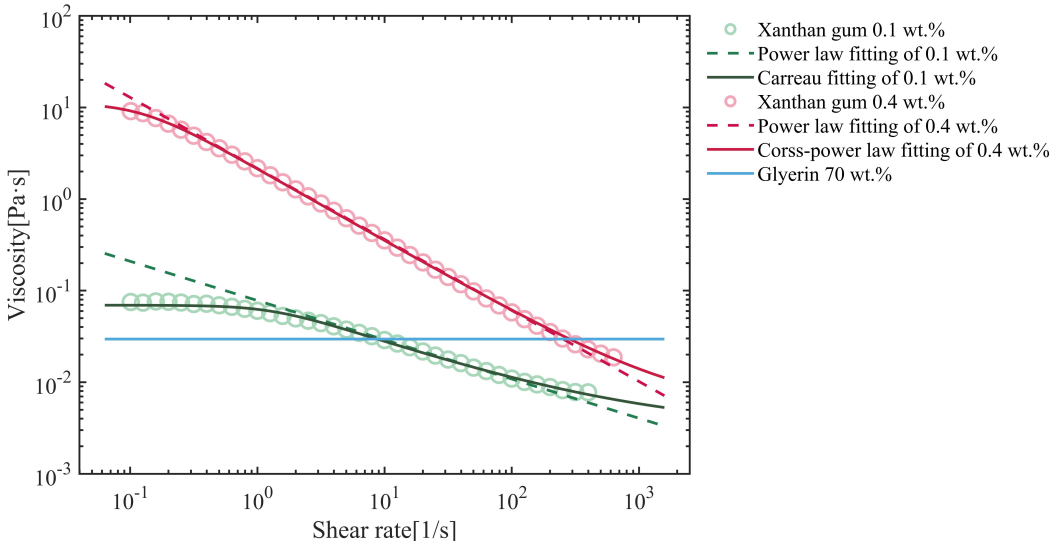

Figure 2.13: Measurement results and fitting curves of the working solution

In this study, the rheology curves were measured on a stress-controlled rheometer

(MCR-302 WESP,*Anton Paar USA Inc.*). The solutions were tested right before the experiment and three independent measurements were conducted for every sample to test the reproducibility of the results. The measurement results are marked as scatters in Figure 2.13, and the rheology curves are fitted by both the Power Law model in dashed lines and the Carreau model in solid lines. And the corresponding parameter values of the fitting models are listed in Table 2.5.

	μ [Pa·s]	$k[m^2/s]$	n(Power)	μ_0 [Pa·s]	μ_∞ [Pa·s]	λ [s]	n(Carreau)	ρ [kg/m^3]
Glycerol 70 wt.%	0.030	-	-	-	-	-	-	1169.9
XG 0.1 wt.%	-	0.078	0.57	0.069	0.0031	0.75	0.52	984.0
XG 0.4 wt.%	-	2.16	0.22	11.27	0.0048	8.20	0.21	985.2

Table 2.5: Rheological characteristics of the working fluids. XG: Xanthan gum.

2.5 Basic data processing of LDV measurements

The LDV measurements provide the velocity component time series at certain spacial point in the flow field. The velocity time series is composed of discrete velocity samples. Therefore, a velocity profile curve is usually composed of mean velocity value of a series of discrete spatial points. This section is going to describe the general methods of LDV data processing, with a focus on the mean velocity and fluctuations.

For a turbulent flow described by mean velocity and fluctuations of one spacial point, as shown by:

$$u(t) = \bar{u} + u'(t) \tag{2.48}$$

the mean velocity $\bar{u}$ is calculated by:

$$\bar{u} = \frac{1}{N}\sum_{\mathrm{i}=1}^{\mathrm{N}} u_{\mathrm{i}} \tag{2.49}$$

where N is the total sample number of the measurement.

The fluctuation component can be described as turbulent strength by the standard deviation of this group of samples statistically:

$$\sigma_{\mathrm{u}} = \sqrt{\frac{1}{N}\sum_{\mathrm{i}=1}^{\mathrm{N}}(u')^2} = \sqrt{\frac{1}{N}\sum_{\mathrm{i}=1}^{\mathrm{N}}(u_{\mathrm{i}} - \bar{u})^2} \tag{2.50}$$

and the variance ${\sigma_{\mathrm{u}}}^2$, equal to the square of the standard deviation, represents the normal turbulent stress of the corresponding velocity component.

The turbulent intensity of the considered velocity component is calculated by:

$$Tu = \sqrt{\frac{{\sigma_{\mathrm{u}}}^2}{\bar{u}^2}} = \frac{\sigma_{\mathrm{u}}}{\bar{u}} \tag{2.51}$$

2.6 Measurement field of the TC flow experiment

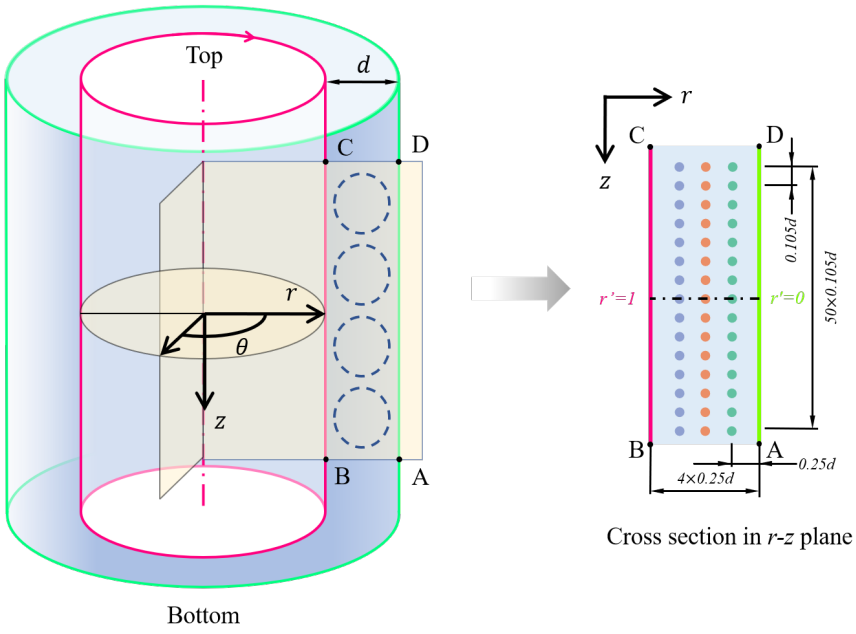

Figure 2.14: Sketch of Taylor vortex cell structure with the corresponding cylindrical coordinate. The right figure explains the measurement field in radial-axial plane.

Figure 2.14 shows the cylindrical coordinate applied in the geometry. The dashed rolls on the left represent the Taylor vortex remnants in the $r - z$ plane, which are considered to be the largest eddies of turbulent TC flow. It will be shown that both the axial velocity field u_z and the mean azimuthal velocity field u_θ, in addition to

depending on the radial position r, will also depend on the axial position z in later discussion. The rectangle $ABCD$ indicates the cross section of the measurement field in the $r - z$ plane.

In Chapter 3, measurements were always conducted at the mid height of the setup, from the stationary cylinder wall ($r' = 0$) to the rotating cylinder wall ($r' = 1$), to obtain the corresponding radial profiles of the flow at mid height.

In Chapter 4, mappings of the azimuthal and axial velocity components were performed as a succession of traverses in the axial direction from the top to the bottom of the geometry at three fixed radial locations to draw the axial profiles. The height of the measurement field ranges $-2.63d \sim 2.63d$ (0 represents the midheight of the cylinder). Each axial profile is made up of 51 measurement points with equidistance in the axial direction. The green, orange, and blue dot lines indicate the three different radial positions of the traverses, which are at the quadrisection points through the annulus, or $(r - R_o)/d = 0.25, 0.5, 0.75$, respectively, as shown in the figure on the right. The profile curves in the plots will be in the same color as the corresponding radial positions in Chapter 4.

Chapter 3

Radial profiles of basic laminar TC flow and TTV

3.1 Torque scaling for comparison with previous experiments and theories

To compare the measurement results with the previous literature, the dimensionless form of torque ($G = T/\rho\nu^2 L$, [25]) was utilized, where T is the torque, ρ is the fluid density, ν is the fluid kinematic viscosity and L is the length of the cylinder.

Marcus[39] made a prediction based on the marginal stability calculation. The annulus was divided into three regions in the radial direction: a thin boundary layer near the inner cylinder, a thin boundary layer near the outer cylinder, and an inviscid core in the middle. It assumes that the core region has a constant angular momentum density, and the boundary layer regions are laminar and marginally stable by maintaining a constant boundary layer thickness. The derived relation between G and Re yields

$$G = 0.202 \left(\eta^{-1} - 1\right)^{-5/3} \mathrm{Re}^{5/3} \tag{3.1}$$

Lathrop[25] mentioned another prediction derived from the Kolmogorov-type argument, which assumes a constant energy dissipation rate. Therefore, the torque is obtained by dividing the dissipated power by the rotation speed, given as:

$$G = \pi \left[\frac{\eta(1+\eta)}{(1-\eta)^2}\right] \mathrm{Re}^2 \tag{3.2}$$

The prediction holds with the infinitely high Reynolds number when the viscous force is negligible, and hence the exponent value equal to 2 might be regarded as an upper limit.

Wendt [40] conducted detailed torque measurements with three different radius ratios ($\eta = 0.68,\ 0385,\ 0.935$) and fit the dimensionless torque results to

$$G_{\text{Wendt}} = 1.45 \frac{\eta^{3/2}}{(1-\eta)^{7/4}} \,\text{Re}^{1.5}, \quad 4 \times 10^2 < \text{Re} < 10^4 \tag{3.3}$$

Lathrop [25] performed the experiment with $\eta = 0.724$ and the data fit the following relation:

$$\log_{10} G_{\text{Lathrop}} = 5.726 + 0.3235 \left(\log_{10} \text{Re}\right)^2 - 1.002 \left(\log_{10} \text{Re}\right), \quad \text{Re} < 1.0 \times 10^4 \tag{3.4}$$

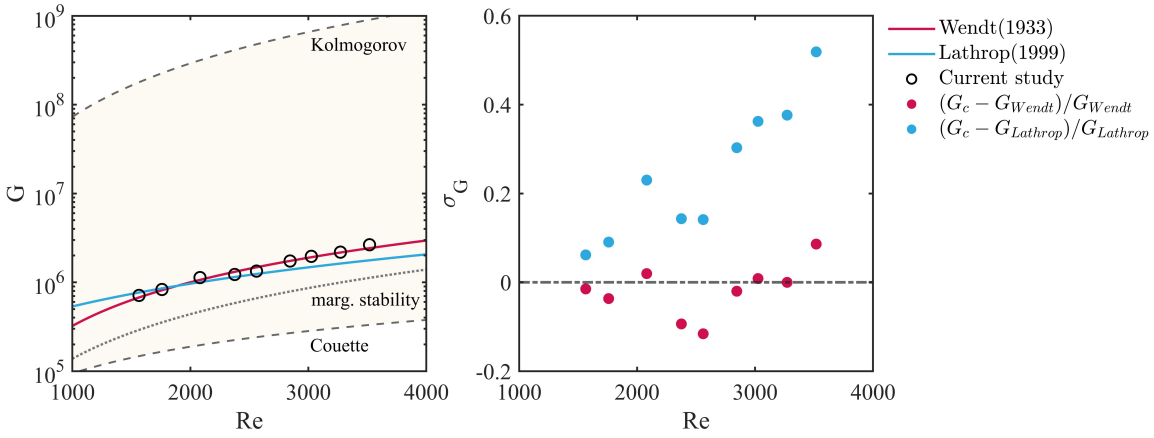

Figure 3.1: Left: Comparison between the measured dimensionless torque G_c with the results of the previous experiment (eq. (3.3) [40], eq. (3.4) [25]) and the marginal stability prediction (eq. (3.1)). The yellow area is highlighted between the Kolmogorov-type prediction (eq. (3.2)) and the laminar Couette flow torque ($G = 4\pi\eta \left[(1+\eta)(1-\eta)^2\right]^{-1} \text{Re}$), as upper and lower bounds, respectively. Right: Relative deviations from results of Wendt (eq. (3.3) [40]) and Lathrop (eq. (3.4) [25]).

As shown by fig. 3.1, the measurements of torque show just slight deviations from the past work, and especially agree well with the results of Wendt, which validates our results. Taking into account the different radius ratio $\eta = 0.724$ utilized by Lathrop and $\eta = 0.76$ in the current study, a relatively larger deviation between the

current study and Lathrop's results is acceptable. Besides, the marginal stability result eq. (3.1) apparently underrates the torque, but still shows a similar magnitude to the measurement results in the depicted range.

3.2 Basic laminar TC flow

In this section, theoretical and numerical analysis of basic laminar TC flow are performed. Two rheological models for non-Newtonian fluids are included: the power law model and the Carreau model. The effects of varying geometrical and rheological parameters are explored and presented by profiles.

3.2.1 Scaling of the rheology models

An incompressible shear flow between two infinitely long concentric cylinders is considered. The inner cylinder is rotational and the outer is stationary. The radius ratio η of the two cylinders is defined as $\eta = R_i/R_o$. The length scalars are normalized by the width of the annulus between the two cylinders $d = R_o - R_i$. Therefore, the dimensionless radii of the cylinders can be expressed, respectively, by

$$\begin{aligned} \tilde{R}_i &= \frac{R_i}{d} = \frac{\eta}{1-\eta} \\ \tilde{R}_o &= \frac{R_o}{d} = \frac{1}{1-\eta} \end{aligned} \tag{3.5}$$

where the tilde ($\tilde{\cdot}$) denotes dimensionless quantities. In addition, the velocity of the inner cylinder $u_{\theta,i} = \omega_{\theta,i} R_i$ is the reference velocity scale. $\dot{\gamma}_{ref} = u_{\theta,i}/d$ is the reference shear rate scale, sometimes also called the nominal shear rate. $\tau_{ref} = \mu_{ref}\dot{\gamma}_{ref}$ is the reference stress scale.

The adopted reference viscosity scale μ_{ref} is widely used in the previous literature and is defined differently depending on the specific rheology model. Hence, the reference viscosity scale will be indicated with each rheological model in the following section.

Scaling of power law model

$$\tilde{\mu} = \frac{k \cdot \dot{\gamma}_{ref}{}^{n-1}}{\mu_{ref}} \tilde{\dot{\gamma}}^{n-1} \tag{3.6}$$

where $\mu_{ref} = k \cdot \dot{\gamma}_{ref}{}^{n-1}$

Scaling of Carreau model

$$\tilde{\mu} = \frac{\mu_\infty}{\mu_{ref}} + \left(\frac{\mu_0}{\mu_{ref}} - \frac{\mu_\infty}{\mu_{ref}} \right) \left[1 + (\tilde{\lambda}\tilde{\dot{\gamma}})^2 \right]^{\frac{n-1}{2}} \tag{3.7}$$

where $\mu_{ref} = \mu_0$ and $\tilde{\lambda} = \lambda \dot{\gamma}_{ref}$. In the Carreau model, λ controls the beginning of the shear-thinning region of the rheogram, and λ^{-1} is the characteristic shear rate value of the onset of the shear-thinning.

3.2.2 Basic laminar TC flow

The basic laminar TC flow is defined as a stationary axisymmetric laminar flow with a purely azimuthal velocity field ($u_r = 0, u_\theta = u_\theta(r), u_z = 0$) [16]. Therefore, $\dot{\gamma}_{r\theta}(r) = \dot{\gamma}_{\theta r}(r)$ and $\tau_{r\theta}(r) = \tau_{\theta r}(r) = \mu \dot{\gamma}_{r\theta}$ are, respectively, the only nonzero elements of the strain rate tensor and the stress tensor, and the momentum equation reduces to

$$\frac{d(r^2 \tau_{r\theta})}{dr} = 0 \tag{3.8}$$

The integration of eq. (3.8) yields the following:

$$\frac{\tau_{r\theta}(r)}{\tau_{r\theta}(R_i)} = (\frac{R_i}{r})^2 \tag{3.9}$$

which indicates that the magnitude of the local stress monotonically decreases from the inner wall to the outer wall. The velocity profiles across the annulus and the corresponding strain rate profiles, viscosity profiles can be derived by solving the equation set made up by eq. (3.8) (or eq. (3.9)), the non-slip boundary condition $u_\theta(R_o) = 0$ and $u_\theta(R_i) = u_{\theta,i}$ and the fluid rheological curve.

3.2.3 Newtonian fluid

For a Newtonian fluid with constant viscosity, the analytical solution of the azimuthal angular velocity profile can be expressed as

$$\begin{aligned}\omega_\theta(r) &= \frac{\omega_i {R_i}^2}{{R_i}^2 - {R_o}^2}\left(1 - \frac{{R_o}^2}{r^2}\right) \\ &= \frac{\omega_i}{1-\eta^2}\left(1 - \frac{{R_o}^2}{r^2}\right)\end{aligned} \tag{3.10}$$

and the shear rate profile in the radial direction is:

$$\begin{aligned}\dot{\gamma}_{r\theta}(r) &= r\frac{\partial \omega_\theta(r)}{\partial r} \\ &= \frac{2\omega_i}{1-\eta^2}\frac{{R_o}^2}{r^2}\end{aligned} \tag{3.11}$$

Apparently, the profiles do not depend on the viscosity and only refer to the aspect ratio η, and $\omega_\theta(r) \sim 1 - (R_o/r)^2$, $\dot{\gamma}_{r\theta}(r) \sim (R_o/r)^2$. Figure 3.2 draws the scaled eqs. (3.10) and (3.11) with different η. In fig. 3.2b, the profiles deviate from the curve of the reference case (gray dashed line), a simple shear flow between two parallel plates, as the aspect ratio (η) decreases. As for the shear rate profiles, a smaller η results in a lower shear rate at the outer stationary cylinder but higher shear rate at the inner rotational wall, and the degree of difference at the inner wall is apparently larger than the outer wall.

3.2.4 Power law fluid

As the working fluid is a power law fluid described by eq. (3.6), the velocity and shear rate profiles are identified, respectively, by:

$$\begin{aligned}\omega_\theta(r) &= \omega_i\left(\frac{1}{{R_o}^{2/n}} - \frac{1}{{R_i}^{2/n}}\right)^{-1}\left(\frac{1}{{R_o}^{2/n}} - \frac{1}{r^{2/n}}\right) \\ &= \omega_i\left(1 - \frac{1}{\eta^{2/n}}\right)^{-1}\left[1 - (\frac{R_o}{r})^{2/n}\right]\end{aligned} \tag{3.12}$$

$$\begin{aligned}\dot{\gamma}_{r\theta}(r) &= \frac{2\omega_i}{n}\left(\frac{1}{R_o^{2/n}} - \frac{1}{R_i^{2/n}}\right)^{-1}\frac{1}{r^{2/n}} \\ &= \frac{2\omega_i}{n}\left(1 - \frac{1}{\eta^{2/n}}\right)^{-1}(\frac{R_o}{r})^{2/n}\end{aligned} \tag{3.13}$$

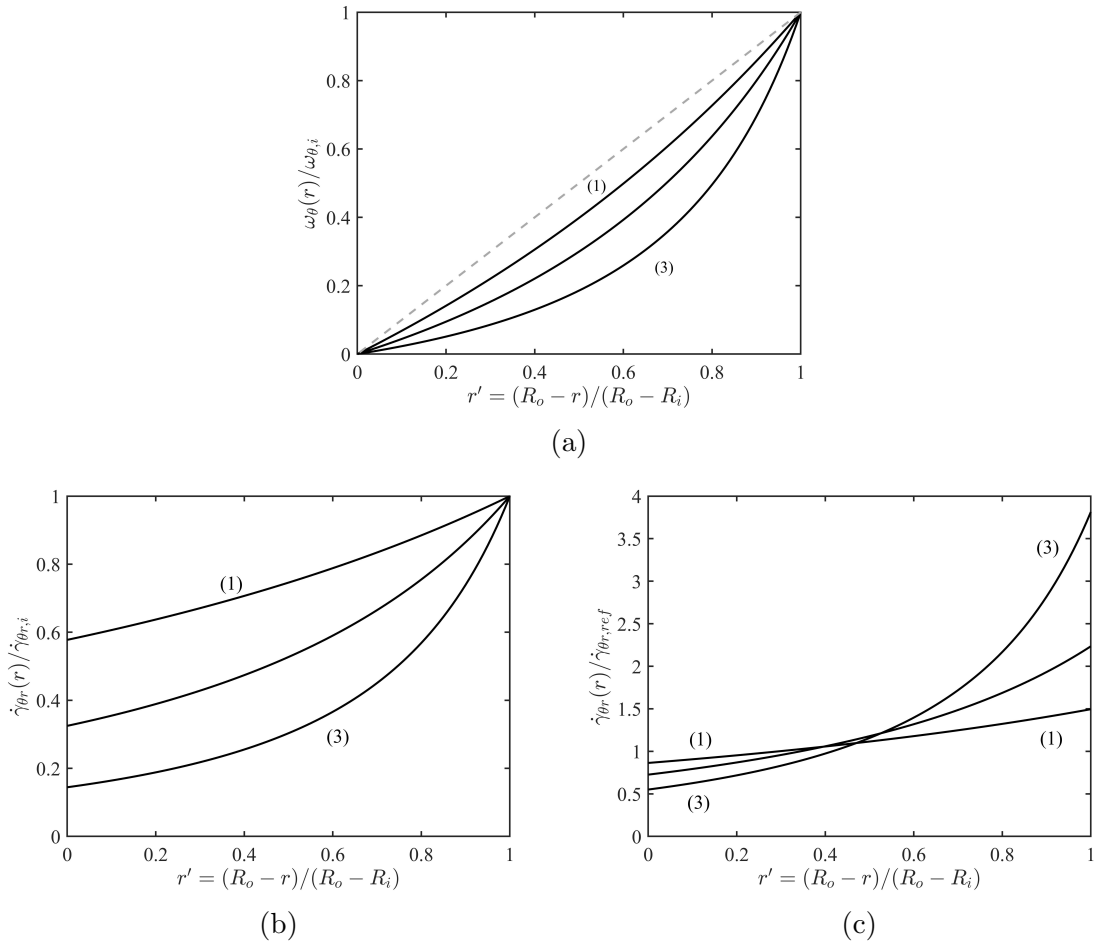

Figure 3.2: Basic laminar TC flow of Newtonian fluids. (a) Azimuthal angular velocity profiles. (b) Shear rate profiles scaled by the value at the inner wall. (c) Shear rate profiles scaled by the reference shear rate. (1) $\eta = 0.75$; (2) $\eta = 0.50$; (3) $\eta = 0.25$ and the gray dashed line: simple shear flow between parallel plates.

If $n = 1$, eqs. (3.12) and (3.13) reduces to eqs. (3.10) and (3.11).

The viscosity profiles can then be easily obtained by applying the corresponding rheological equation:

$$\mu_{r\theta}(r) = \mu[\dot{\gamma}_{r\theta}(r)] \tag{3.14}$$

The profiles of power law fluids with various shear-thinning indices n and fixed aspect ratio are depicted by fig. 3.3. From figs. 3.3b to 3.3d, an increasing shear thinning effect (decreasing n) leads to a deviation from the Newtonian case, which is the same as the behavior resulting from the decreasing aspect ratio with Newtonian fluid as

observed in fig. 3.2. Therefore, a stronger shear thinning effect and a smaller aspect ratio can mutually reinforce this deviation.

With respect to the viscosity profiles, the viscosity decreases monotonically from the outer wall to the inner wall. Also, a stronger shear thinning effect indicates a higher viscosity at the outer wall but lower viscosity at the inner wall, corresponding to a greater alternation amplitude.

3.2.5 Carreau fluid

For the Carreau model, the analytical expression of the profiles cannot be obtained. Instead, the equations are solved numerically. Figure 3.4 depicts the profiles with varying n and fixed λ, and fig. 3.5 for fixed n and varying λ.

In figs. 3.4a and 3.5a, the rheograms of the Carreau fluids (solid line) are exhibited with the power law fluids with the same n, to emphasize their rheological differences at the viscosity plateau.

In figs. 3.4b to 3.4e, generally, a stronger shear thinning effect of Carreau fluids leads to a similar deviation trend to power law fluids, but the magnitude of deviation is greatly inhibited compared to power law fluids as shown in figs. 3.3b to 3.3e. However, the velocity and shear rate profiles of both type of fluids still keep a convex shape.

In terms of viscosity profiles (figs. 3.4e to 3.4f), the local viscosity decreases monotonically from the outer wall to the inner wall, and a stronger shear thinning effect still enhances this deviation. But compared to power-law fluids with the same shear thinning index (figs. 3.3b to 3.3e), this deviation is still greatly inhibited. Additionally, the viscosity profiles are convex, different from those of power law fluids.

In fig. 3.4d, $\tilde{\dot{\gamma}}$ is around 10^0, where is exactly the transition region from the viscosity plateau to the shear-thinning region for the Carreau fluids in fig. 3.4a. In this shear rate range, unlike power law fluids, Carreau fluids exhibit a weaker shear thinning characteristic and the effect of the viscosity plateau should not be ignored. As the

ratio between the flow advection time and the characteristic time $\tilde{\dot{\gamma}}^{-1}/\lambda$ decreases, the effect of the viscosity plateau becomes less obvious, as shown by figs. 3.5b to 3.5e. In the current study, the ratio $\tilde{\dot{\gamma}}^{-1}/\lambda \approx 10^{-2}$. As curve (4) shown in fig. 3.5a, in this case, the Carreau model functions similarly to the power law model and the viscosity plateau effect can be ignored.

3.2.6 Basic laminar TC flow with experimental fluids of this study

The basic laminar TC flow with the working fluid used in this study is depicted in fig. 3.6. The related parameters of the rheology model are listed in table 2.5. As we have $\tilde{\dot{\gamma}}^{-1}/\lambda \approx 10^{-2}$, we find that the Carreau model exhibits little difference from the power-law model and the curves of both models almost overlap with each other.

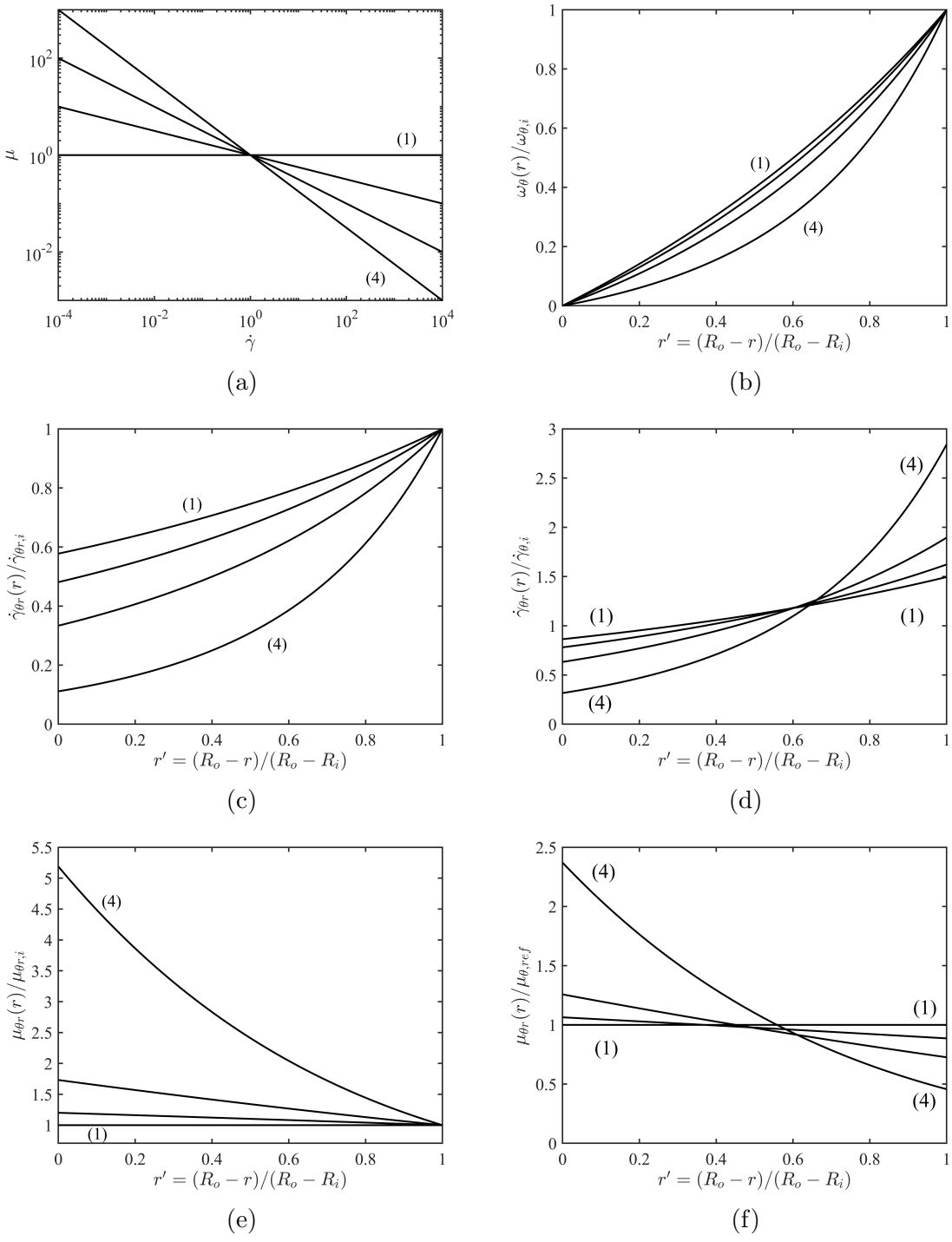

Figure 3.3: Basic laminar flow with power law fluids with $\eta = 0.76$. (a) Rheogram of power-law fluids. (b) Azimuthal angular velocity profiles. (c) Shear rate profiles scaled by value at the inner wall. (d) Shear rate profiles scaled by the reference shear rate scale. (e) Viscosity profiles scaled by value at the inner wall. (f) Viscosity profiles scaled by reference viscosity scale. (1) $n = 0$ Newtonian fluid; (2) $n = 0.75$; (3) $n = 0.50$; (4) $n = 0.25$.

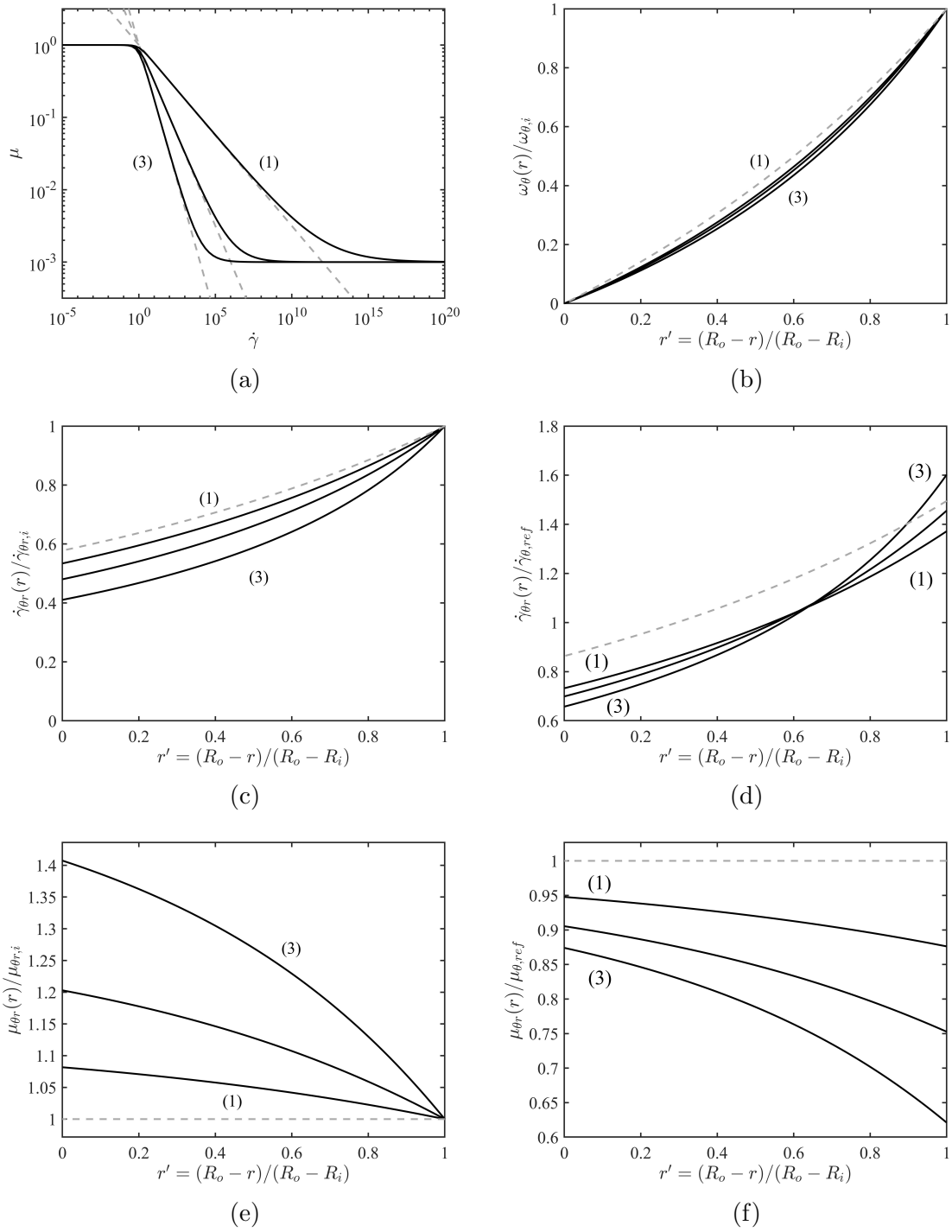

Figure 3.4: Pure laminar flow of Carreau fluids with $\eta = 0.76$ and $\lambda = 1$. (a) Rheogram of Carreau fluids (solid black line) and power law fluids (dashed gray line) with the same n value as the corresponding Carreau fluids (gray dashed line) (b) Azimuthal angular velocity profiles. (c) Shear rate profiles. (d) Viscosity profiles. The gray dashed line: Newtonian fluid. Quantities denoted by the prime ($'$) are normalized by the corresponding value at the inner wall, which are denoted by the subscript i. (1) $n = 0.25$; (2) $n = 0.50$; (3) $n = 0.75$.

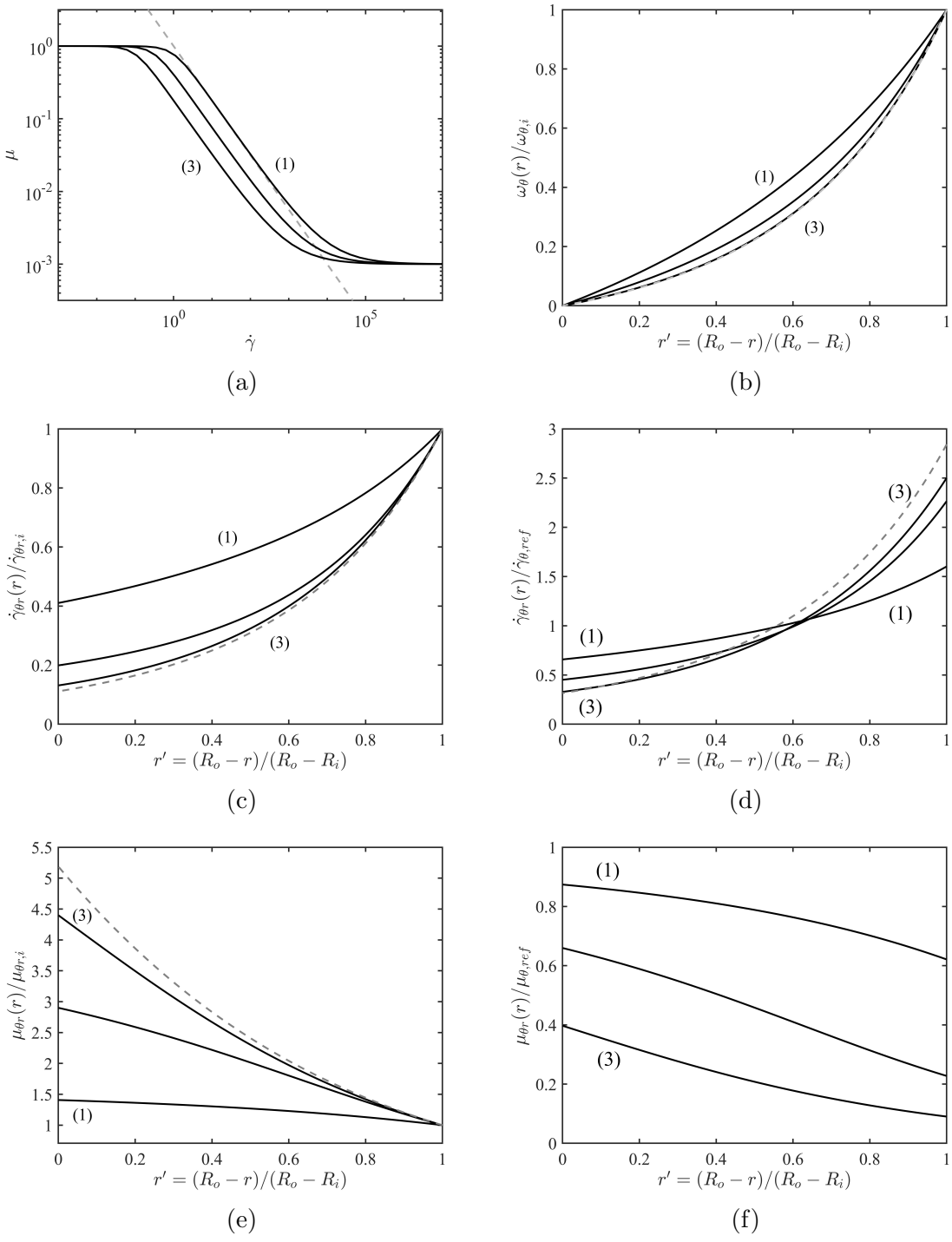

Figure 3.5: Pure laminar flow of Carreau fluids with $\eta = 0.76$, and $n = 0.25$. (a) Rheogram of Carreau law fluids. (b) Azimuthal angular velocity profiles. (c) Shear rate profiles. (d) Viscosity profiles. (1) $\lambda = 1$; (2) $\lambda = 10$; (3) $\lambda = 100$. The gray dashed line: power law fluid with the same n value as the corresponding Carreau fluid, $n = 0.25$. Quantities denoted by the prime ($'$) are normalized by the corresponding value at the inner wall, which are denoted by a subscript i.

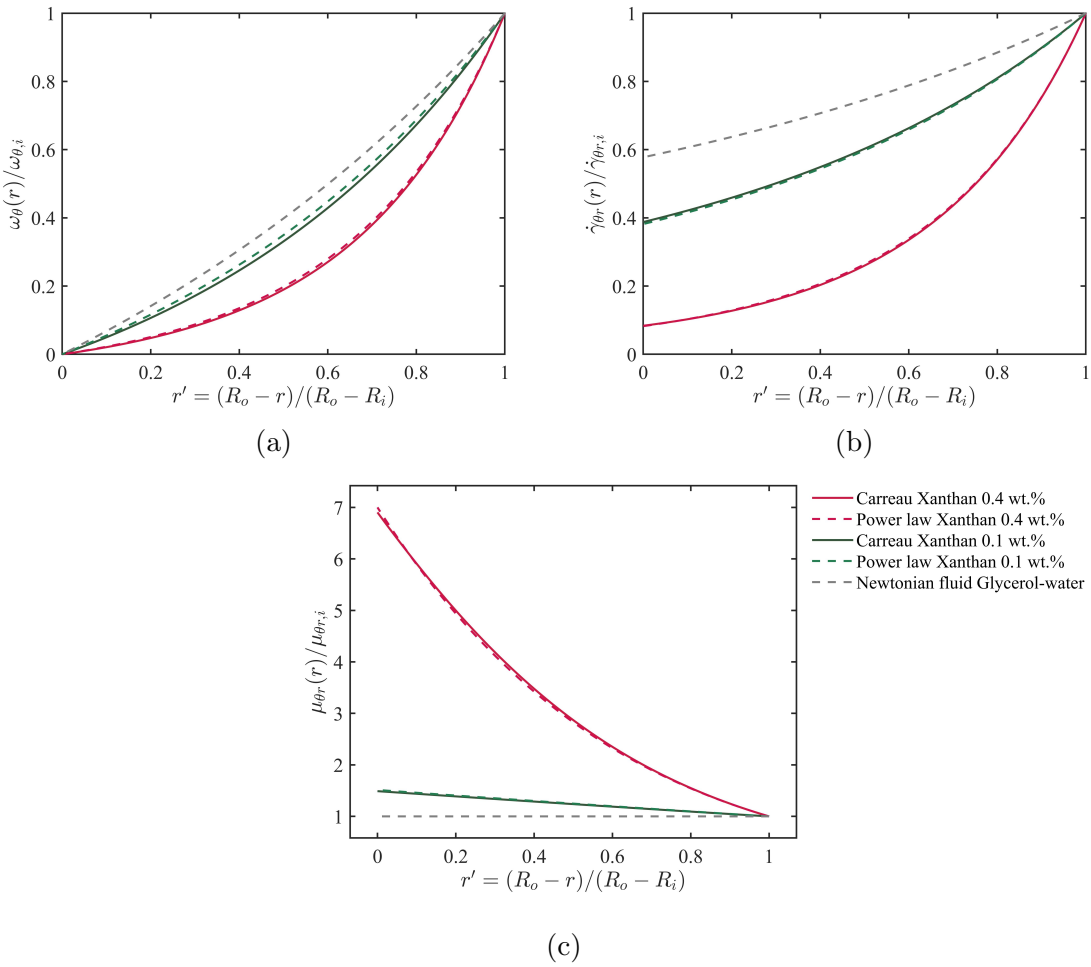

Figure 3.6: Pure laminar flow of the two xanthan gum aqueous fluids described in table 2.5 with $\eta = 0.76$. (a) Azimuthal angular velocity profiles. (b) Shear rate profiles. (c) Viscosity profiles. Curves are normalized by the corresponding value at the inner wall.

3.3 Radial profiles

3.3.1 Data collection and piecewise polynomial fitting of velocity profile

Figures 3.7 to 3.9 represent the radial measurement results with glycerin-water mixture, 0.4 wt.% and 0.1 wt.% Xanthan gum aqueous solutions, respectively. As the data obtained by LDV are the local velocity of discrete spatial points (as the circle markers), a piecewise polynomial fitting method was utilized to get an analytical expression of every profile. Every velocity profile was divided into 3 pieces: two near-wall region and one bulk region. The near-wall region usually exhibits a high velocity gradient, while the bulk region does not. Every region was fitted with a third-order polynomial, and necessary constraints were applied: (1)boundary condition: the velocity equals to the rotating cylinder at the inner wall and zero at the outer wall; (2) continuity: the velocity and its gradient at the connection point should be equivalent to ensure the profile is continuous and smooth. Once the velocity profile fitting is obtained, the shear rate and viscosity profile can be accessible from the velocity profile's derivative.

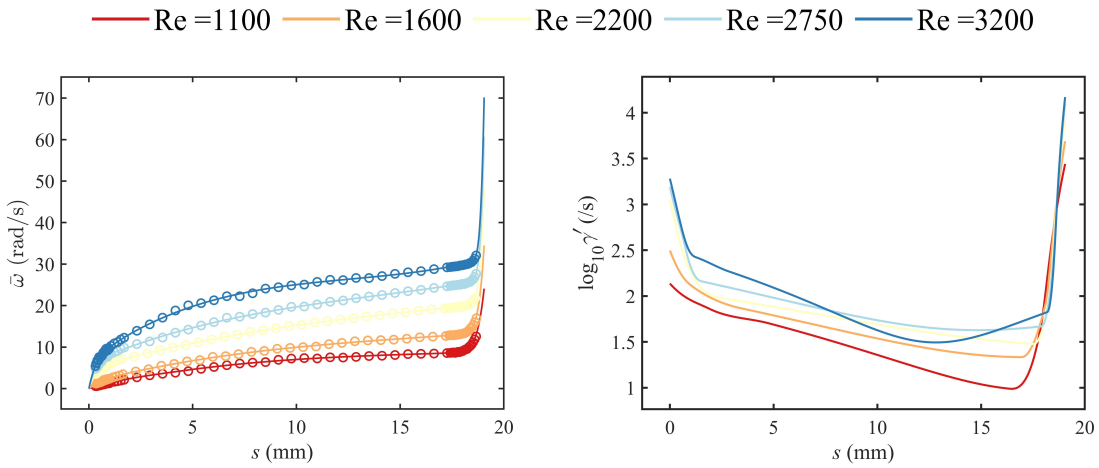

(a) (b)

Figure 3.7: Profiles of the TC flow experiment with Newtonian working fluids (glycerin). (a) Experiment results (circle marker) and curve fittings (solid line) of the azimuthal velocity profiles (ω_θ) in the radial direction. (b) Shear rate profiles in the radial direction.

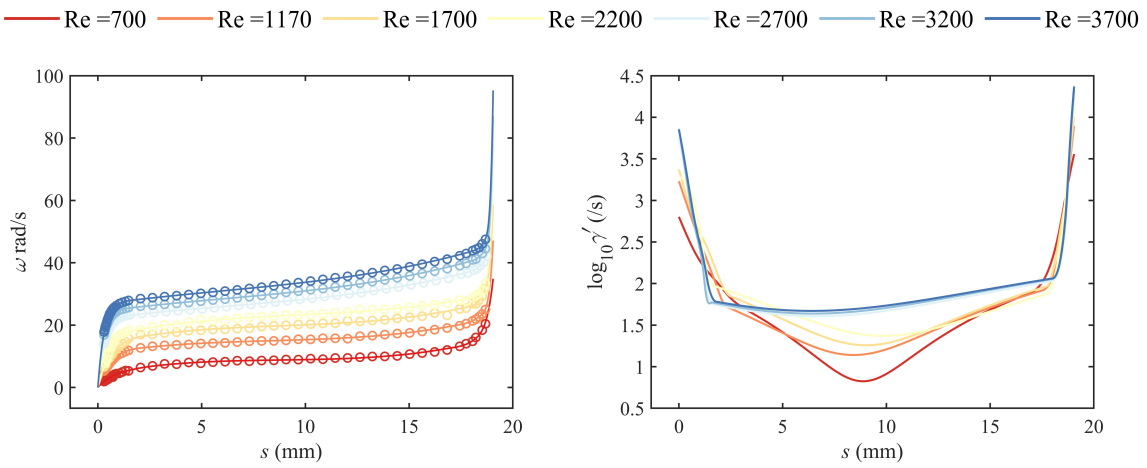

(a) (b)

Figure 3.8: Profiles of the TC flow experiment of non-Newtonian working fluids with strong shear-thinning effect (0.4 wt.% Xanthan gum aqueous solution). (a) Experiment results (circle marker) and curve fittings (solid line) of the azimuthal velocity profiles (ω_θ) in radius direction. (b) Shear rate profiles in radius direction.

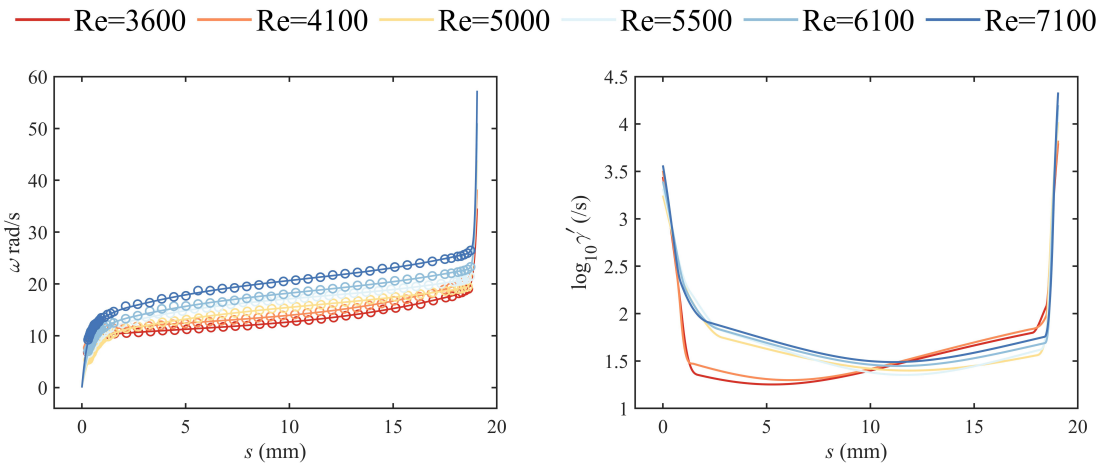

(a) (b)

Figure 3.9: Profiles of the TC flow experiment of non-Newtonian working fluids with relatively weaker shear-thinning effect (0.1 wt.% Xanthan gum aqueous solution). (a) Experiment results (circle marker) and curve fittings (solid line) of the azimuthal velocity profiles (ω_θ) in radius direction. (b) Shear rate profiles in radius direction.

3.3.2 Newtonian TTV

As the shear rate profiles depicted by figs. 3.10a and 3.10b, the boundary between the bulk region and the inner near-wall region is quite clear, while it is not quite

obvious between the bulk region and the outer near-wall region, especially in the low Re cases, i.e. Re=1100, 1600. Generally, the shear rate profiles keep decreasing from the inner wall, start to increase dramatically at the inner near-wall region and reach the maximum at the inner wall.

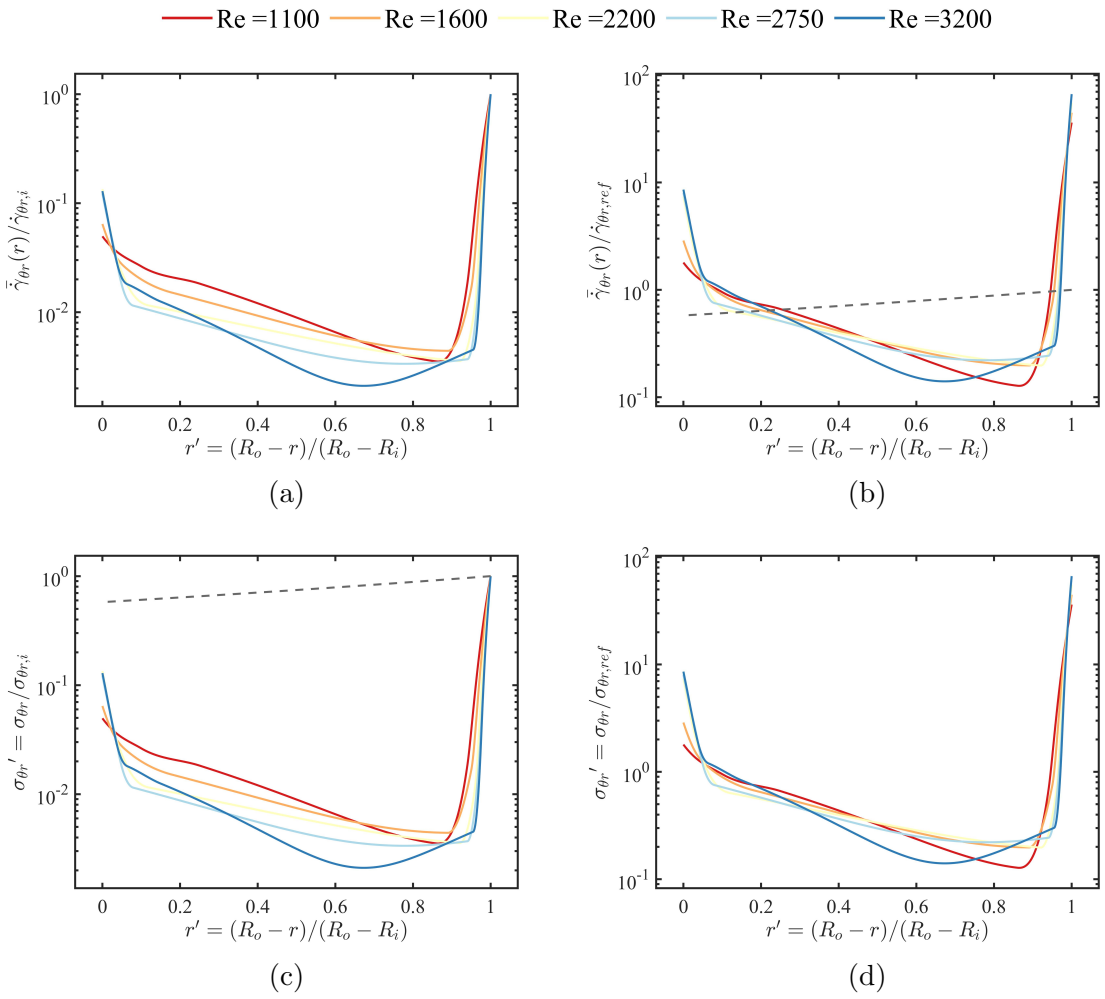

Figure 3.10: Derivative profiles of the TC flow experiment of Newtonian working fluids (glycerin-water mixture) by different scaling. (a)&(b) Shear rate profiles. (c)&(d) Viscous stress profiles. Figures on the left column are scaled by the value at the inner wall, which is denoted by the subscript i, and those on the right column are scaled by the corresponding reference scale as denoted by the subscript ref.

3.3.3 Non-Newtonian TTV

0.4 wt.% Xanthan gum aqueous solution

As shown by fig. 3.11a, for low Re (i.e. Re=700), the lowest shear rate is obtained at the middle of the gap ($r' \approx 0.45$) and no obvious boundary between the bulk region and near-wall region is observed. However, as Re increases, the boundary becomes more clear, and finally forms a "U" shape, with a quite flat bottom at the bulk region (i.e. Re = 2700 to 3700). The shear rate and its gradient are quite low at the bulk region, but high at the two near-wall regions. Owing to the shear-thinning characteristic of the fluid, it indicates a sandwich structure of the viscosity distribution: two low-viscosity layers at the near wall regions and one high-viscosity core at the bulk region, as depicted by figs. 3.11c and 3.11d. In fig. 3.11f, the viscous stress at the bulk region is always approximately equivalent to $0.7\mu_{ref}$, where $\mu_{ref} = \mu_{\mathrm{n}} = \mu|_{u_{\theta,i}/d}$. But the viscous stress at the wall increases with increasing Re.

0.1 wt.% Xanthan gum aqueous solution

Generally, the profiles of 0.1 wt.% Xanthan gum aqueous solution are similar to Re= 2700, 3200, 3700 of 0.4 wt.% Xanthan gum aqueous solution, which have been described in the previous subsection. It is worth stressing here is that the profiles can be apparently classified into 2 modes: Re = 3600, 4100 and Re = 5000 $\sim$ 7100. The main difference between these 2 modes is the profiles at the bulk region. The shear rate profiles of the two lower Re cases are increasing at the bulk region, while the profiles are decreasing of the three higher Re cases. The different trend can also be observed from the rest of the profiles in fig. 3.12 and the radial profiles of turbulence strength (fig. 3.13). This difference is found to be related to different Taylor vortex structures, and will be analyzed in the later chapter.

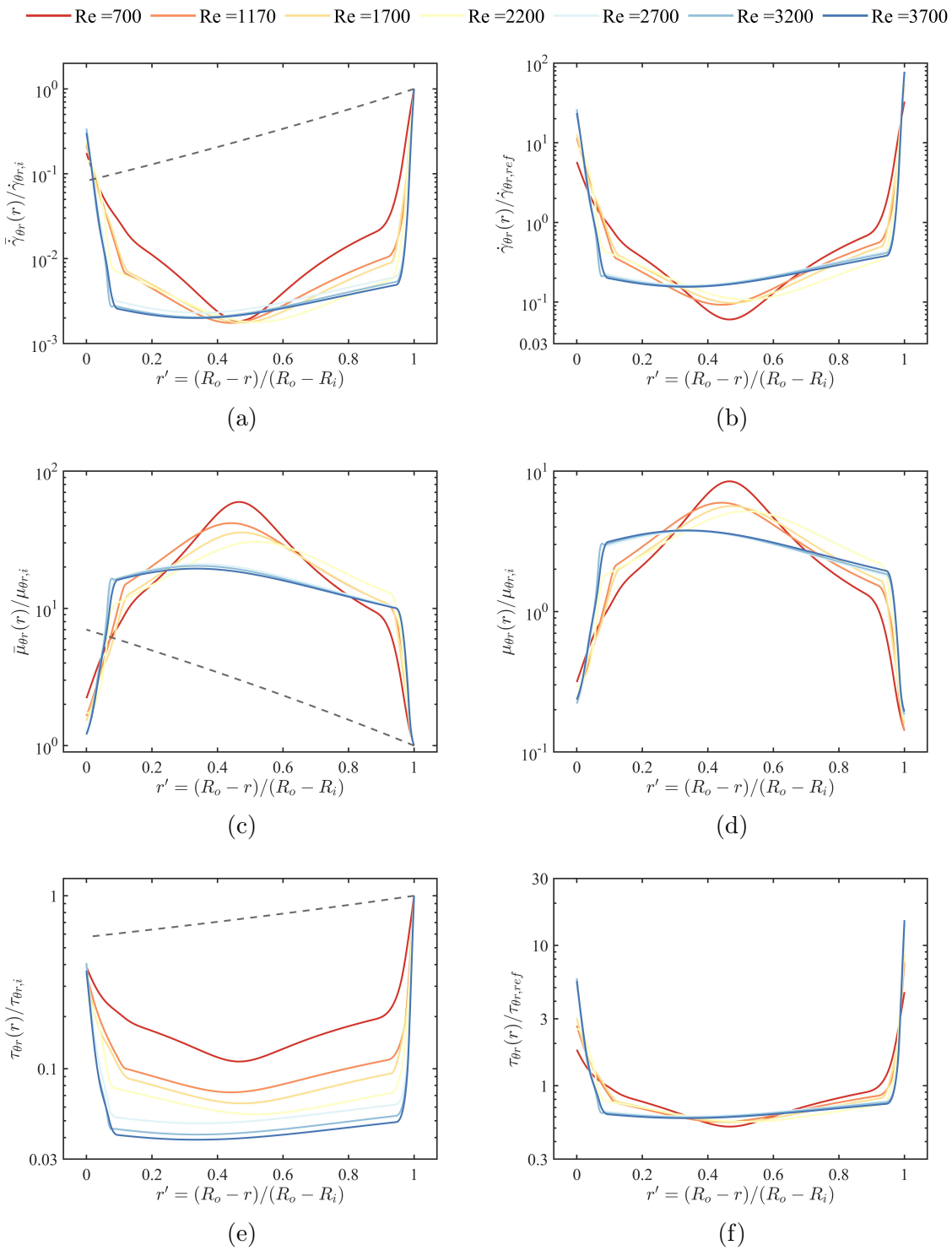

Figure 3.11: Derivative profiles of the TC flow experiment of non-Newtonian working fluid with strong shear-thinning effect (0.4 wt.% Xanthan gum aqueous solution) by different scaling. (a)&(b) Shear rate profiles. (c)&(d) Viscosity profiles. (e)&(f) Viscous stress profiles. Figures on the left column are scaled by the value at the inner wall, which is denoted by the subscript i, and those on the right column are scaled by the corresponding reference scale as denoted by the subscript ref.

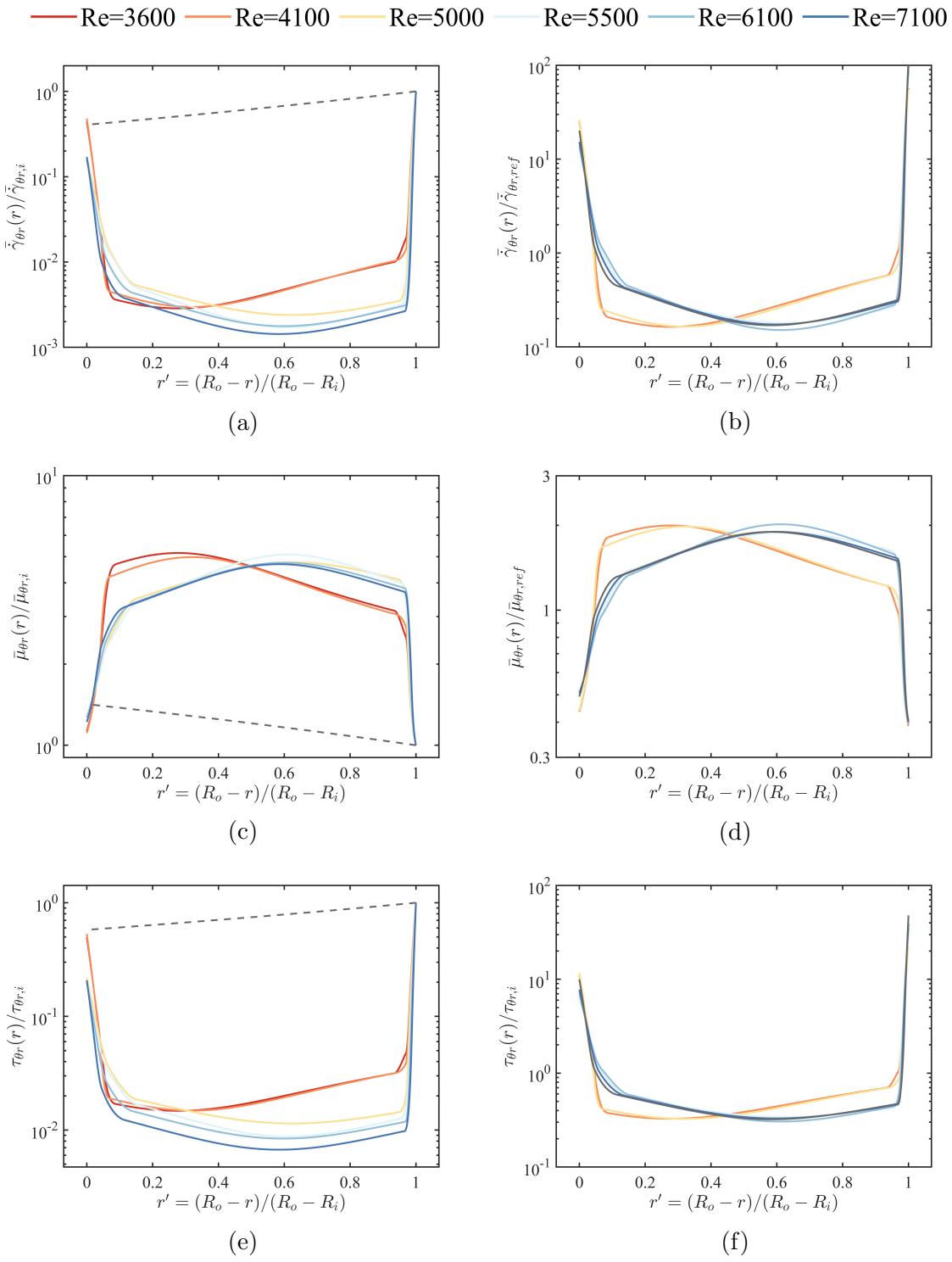

Figure 3.12: Derivative profiles of the TC flow experiment of non-Newtonian working fluid with relatively weaker shear-thinning effect (0.1 wt.% Xanthan gum aqueous solution) by different scaling. (a)&(b) Shear rate profiles. (c)&(d) Viscosity profiles. (e)&(f) Viscous stress profiles. Figures on the left column are scaled by the value at the inner wall, which is denoted by the subscript i, and those on the right column are scaled by the corresponding reference scale as denoted by the subscript ref.

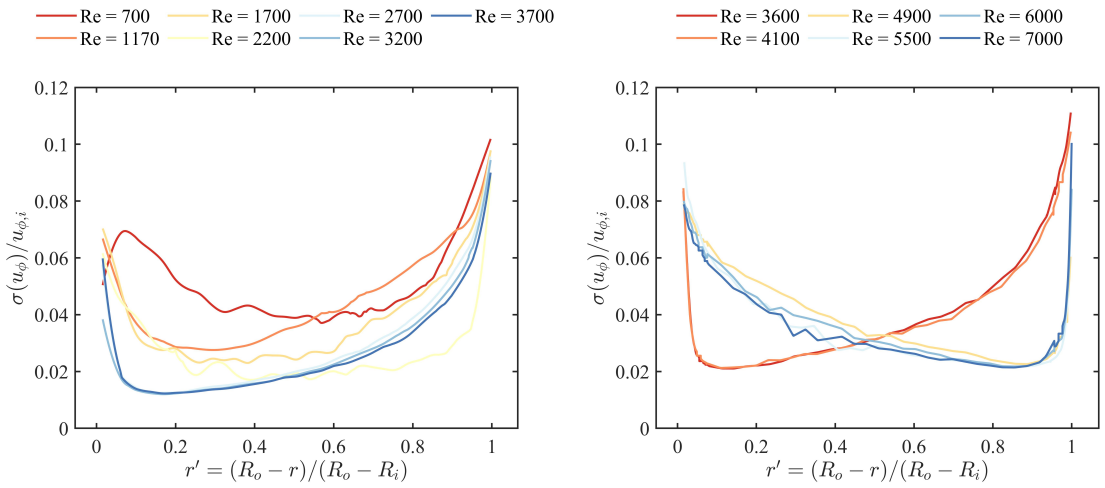

(a) (b)

Figure 3.13: Turbulent strength profiles through the annulus. (a) 0.4 wt.% Xanthan gum aqueous solution, $n = 0.22$. (b) 0.1 wt.% Xanthan gum aqueous solution, $n = 0.51$.

3.4 Different definitions of Reynolds number with non-Newtonian fluids

3.4.1 Various Reynolds number definitions

Due to the varying viscosity in the flow field, which caused by the rheological characteristic of the Non-Newtonian fluid, Reynolds number defined with consistent viscosity is no more applicable. Some Reynolds numbers calculated by different viscosity were proposed in the literature, aiming to take the varying viscosity into account.

The Reynolds number based on the nominal shear rate across the gap ($\mu_{\mathrm{n}} = \mu|_{u_{\theta,i}/d}$) is the most widely used:

$$\mathrm{Re} = \frac{\rho u_{\theta,i} d}{\mu_{\mathrm{n}}} \tag{3.15}$$

In this study, the experiments were also designed based on eq. (3.15) because of its simplicity.

Guzel[12] introduced another definition (Re_G) with consideration of the viscosity variation throughout the flow field for pipe flow. The Reynolds number is redefined on the basis of obtaining the real velocity profile and the viscosity profile. At first, a local Reynolds ($\mathrm{Re}_{G,l}$) number is defined:

$$\mathrm{Re}_{G,l}(r) = \frac{\rho u_\theta(r) d}{\mu(r)} \tag{3.16}$$

Therefore, a local Reynolds number profile $\mathrm{Re}_{G,l}(r)$ could be obtained (the subscript l represents "local"). Then Re_G is defined as the spacial average of $\mathrm{Re}_{G,l}(r)$ throughout the annulus:

$$\begin{aligned} \mathrm{Re}_G &= \frac{2}{(R_o^2 - R_i^2)} \int_{R_i}^{R_o} \mathrm{Re}_{G,l}(r) r dr \\ &= \frac{2\rho d}{(R_o^2 - R_i^2)} \int_{R_i}^{R_o} \frac{u_\theta(r)}{\mu(r)} r dr = \frac{2\rho}{(R_o + R_i)} \int_{R_i}^{R_o} \frac{u_\theta(r)}{\mu(r)} r dr \end{aligned} \tag{3.17}$$

By considering the specific viscosity change in the flow field, this adopted definition is applicable to both Newtonian fluids and non-Newtonian fluids and therefore enable a more proper direct comparison between them.

However, calculating Re on the premise of knowing the velocity profile is not always possible. Therefore, Elçiçek[13] suggested $\mathrm{Re_G}'$ as an alternative. The formulas are similar to eqs. (3.16) and (3.17), but instead of using the profiles of real flow, $u_\theta(r)$ and $\mu_\theta(r)$ profiles were from the basic laminar TC flow, which are numerically accessible:

$$\mathrm{Re_{G,l}}'(r) = \frac{\rho u_\theta'(r) d}{\mu'(r)} \tag{3.18}$$

$$\mathrm{Re_G}' = \frac{2}{(R_o^2 - R_i^2)} \int_{R_i}^{R_o} \mathrm{Re_{G,l}}'(r) r dr \tag{3.19}$$

where the superscript $'$ of $u_\theta(r)$ and $\mu_\theta(r)$ represents the profiles of laminar TC flow. Profiles of $\mathrm{Re_{G,l}}'(r)$ are shown in fig. 3.14.

3.4.2 Evaluation of the applicability of Re_G and $\mathrm{Re_G}'$

In this section, the difference between the radial profiles of basic laminar flow and real flow will be exhibited. The discrepancy between Re_G and $\mathrm{Re_G}'$ will also be displayed and the applicability of $\mathrm{Re_G}'$ will be evaluated.

Figures 3.15 to 3.17 depicted the local Reynolds number profiles of the glycerin-water mixture, 0.4 wt.% Xanthan gum aqueous solution and 0.1 wt.% Xanthan gum aqueous solution, respectively. It is obvious that the profiles of the basic laminar flow (gray dashed line) cannot capture the distribution of local Re. Especially in two non-Newtonian fluids, Re_G is quite low due to the high viscosity in the bulk region, which occupies the majority of the annulus. Therefore, $\mathrm{Re_G}'$ still overrates compared to Re_G. In the appendix, the detailed comparison of Re, Re_G, and $\mathrm{Re_G}'$ is listed in tables.

Overall speaking, $\mathrm{Re_G}'$ is more like just multiplying Re by a factor than really considering the real distribution of the local Reynolds number, which is thought to be unnecessary from the author's personal point of view.

3.5 Summary

This section starts by validating the setup by comparing it with the previous literature.

After that, the effect of the radius ratio, rheological models, and shear thinning index on the radial profiles in the basic laminar TC flow was investigated, which is analytically or numerically accessible. The radial measurement results were then presented in profiles, and piecewise polynomial fittings of the velocity profiles were obtained to calculate the shear rate, viscosity, and viscous stress profiles. The sandwich structure of the profiles in non-Newtonian TTV was analyzed, and two different modes in 0.1 wt.% Xanthan gum aqueous solution were discovered which are related to the Taylor vortex structure.

In the last part, an assumption proposed by previous literature about the use of local Re of laminar TC flow to modify the Re of non-Newtonian Tc flow was evaluated, on the basis of the measurement results. However, it is indicated that this substitution is not necessary and cannot reflect the real local Re distribution in the TC flow.

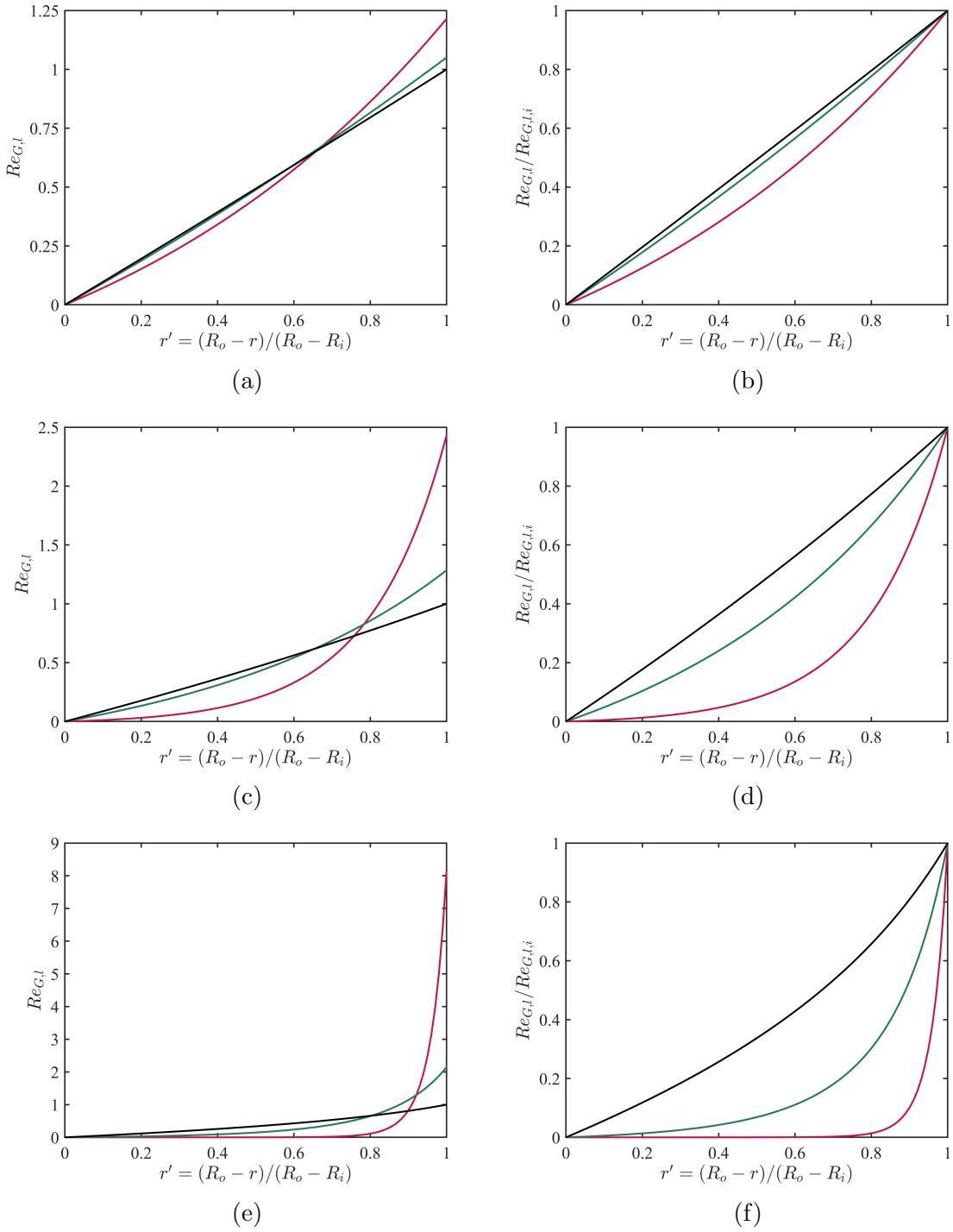

Figure 3.14: $\mathrm{Re}_{G,l}$ profiles of the basic laminar TC flow through the annulus. (a)&(b) $\eta = 0.95$. (c)&(d) $\eta = 0.76$, the same as the apparatus used in this study. (e)&(f) $\eta = 0.38$. The figures in the right column are scaled by the value at the inner wall. Black: $n = 1$, Newtonian solution; Green line: $n = 0.51$, corresponds to 0.1 wt.% Xanthan gum aqueous solution; Red line: $n = 0.22$, corresponds to 0.4 wt.% Xanthan gum aqueous solution. $\mathrm{Re_G}'$ then can be calculated based on these numerically accessible profiles.

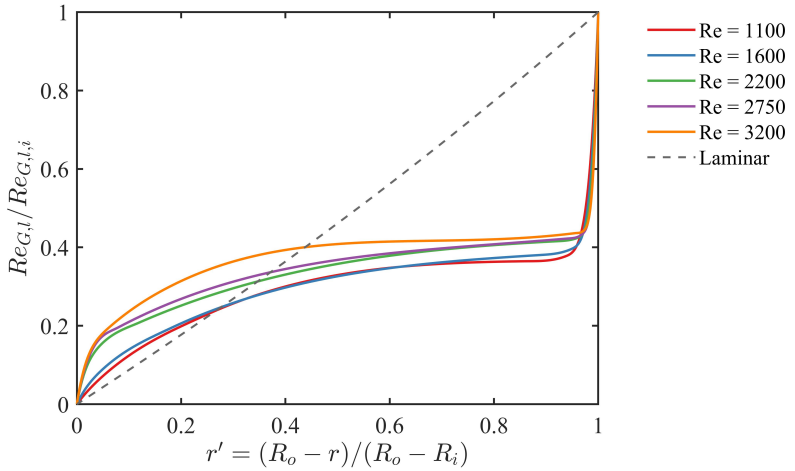

Figure 3.15: $\mathrm{Re}_{G,l}$ profiles of the water-glycerin solution. The figure is scaled by the value at the inner wall. The gray dashed line represents the profile of the basic pure laminar TC flow case as reference, which has been shown as the black line in fig. 3.14d.

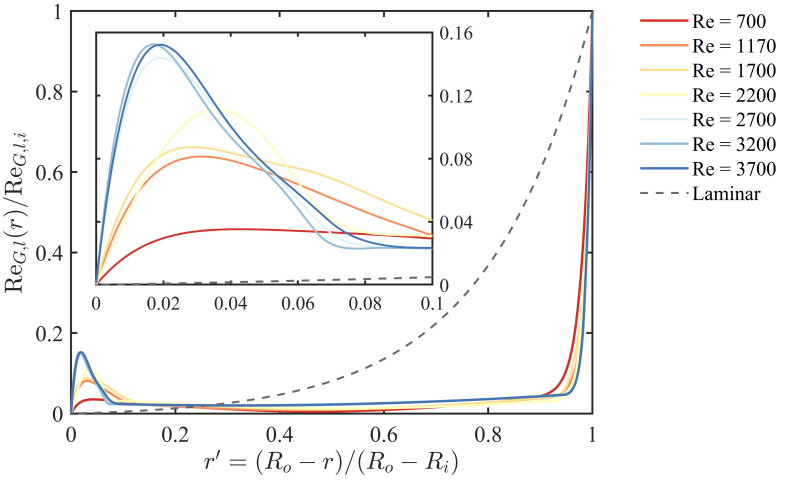

Figure 3.16: $\mathrm{Re}_{G,l}$ profiles of the 0.4 wt.% Xanthan gum aqueous solution. The figure is scaled by the value at the inner wall. The gray dashed line represents the profile of the basic pure laminar TC flow case as a reference, which is shown as the red line in fig. 3.14d.

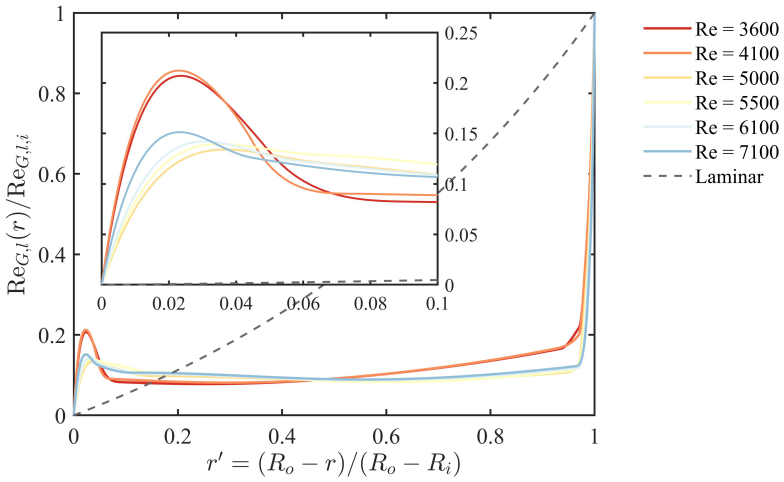

Figure 3.17: $\mathrm{Re}_{G,l}$ profiles of the 0.1 wt.% Xanthan gum aqueous solution. The figure is scaled by the value at the inner wall. The gray dashed line represents the profile of the basic pure laminar TC flow case as a reference, which has been shown as the green line in fig. 3.14d.

Chapter 4

Axial profiles and mapping of the structures in the radial-axial plane

This chapter will mainly discuss the Taylor vortex structure by analyzing the axial profiles of the flow field, which are based on a series of mappings mentioned in section 2.6. In part of Newtonian TTV, the vortex structure is compared to the TVF from the previous work.

Due to the turbulence in the TC flow investigated in this study, the instantaneous flow field always teems with vortices in small scales, and Taylor vortex cells are not clear in the instantaneous flow field, as shown by fig. 4.1a. However, this underlying organized structure could be revealed in the time-averaged mean velocity field (fig. 4.1b). Instantaneously, turbulent fluctuations are superimposed on Taylor vortices, distorting and interrupting these organized structures [32]. As the Reynolds number increases, the turbulent fluctuations dominate and overwhelm the Taylor roll cells in instantaneous flow.

Therefore, the parameters measured in, such as fig. 4.3, are presented as time-averaged axial variations at three different radial positions. A schematic diagram to indicate the sense of radial-axial circulation of the Taylor vortices is shown at the top of every group of figures.

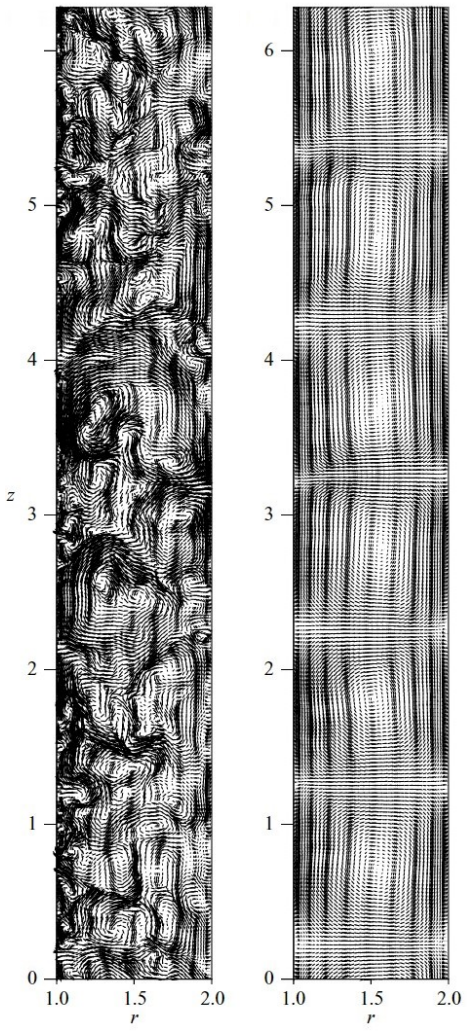

Figure 4.1: Comparison of (a) instantaneous and (b) time-averaged mean flow patterns in a radial-axial plane at $Re = 8000$ for Newtonian fluid. Figures taken from [32].

4.1 Newtonian Turbulent Taylor vortex flow

Taylor vortices could be observed in the time-averaged velocity field, and the structure was found to be stable in the annulus space, which means that the structure exhibits no drift in the radial or axial direction over the measurement timescale. Similar profiles were discovered for all Newtonian cases conducted in this study, with Re from 1100 to 3200. Therefore, only the profiles of $Re = 3200$ are presented in detail to avoid redundancy.

To better illustrate the features of the flow, a more straightforward three-dimensional schematic diagram is shown as fig. 4.2. The blue and red rings circulating the inner cylinder represent the structure of the Taylor vortices that rotate in the opposite direction. The azimuthal velocity at 3 different radial positions is depicted in the real azimuthal direction, and the data are identical to those in fig. 4.3b and figs. 4.4a to 4.4c. The green arrows emphasize the azimuthal velocity overshoot to the minimum at the inward jet flow between two adjacent Taylor vortices, whereas the yellow arrows indicate the velocity overshoot to the maximum. Therefore, the relationship between the radial jet flow and the azimuthal momentum transport is quite clear.

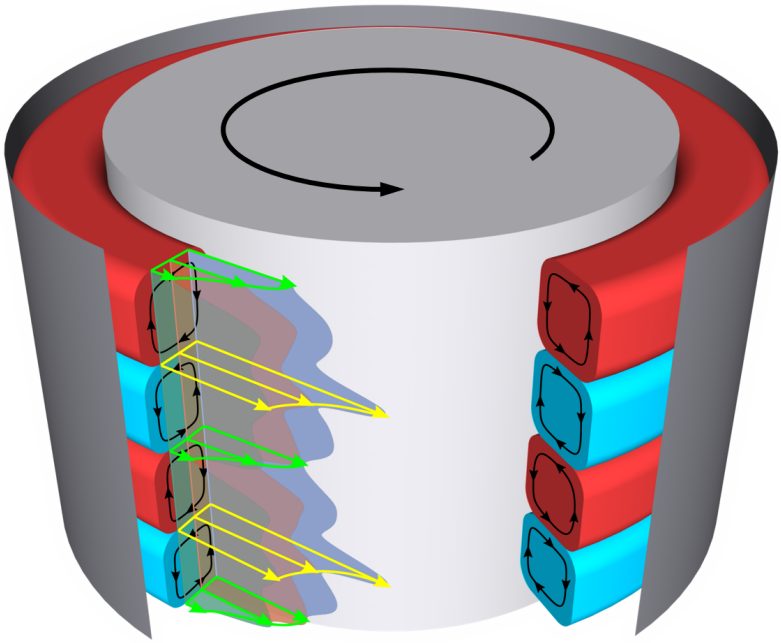

Figure 4.2: 3D schematic diagram of the Newtonian TTV flow

In fig. 4.3c, the profiles of the radial position at 0.25 and 0.75 (blue and green) are sinusoidal with a phase difference of π. However, the amplitude of the sinusoidal waveform cannot be kept on the two sides of the measurement field, indicating the likely presence of the end effects.

In fig. 4.3b, an expected axial periodicity is observed in the azimuthal component with the same frequency as the axial velocity but with a delay of $\pi/2$ (for example,

the maximum and minimum azimuthal velocity correspond to the zero axial velocity). Specifically, the azimuthal velocity is highest at the boundary between adjacent Taylor vortex cells where an outflow jet exists, and decreases to lowest at the outflow jet. This observation is consistent with consideration of the transport of angular momentum in the radial direction. The outflow jet carries the fluid with an excess of angular momentum leading to a velocity overshoot, whilst the inflow jet also leads to an overshoot, but in the reverse direction. Additionally, the magnitude of the overshoots obviously decreases in the direction of the jets (e.g. as h equals 0, where an inflow jet locates, the azimuthal velocity overshoots to a lower value, and the magnitude of the overshoot decreases in the jet's direction, namely, radially inward, from green to blue curve in fig. 4.3a).

In fig. 4.3d and fig. 4.3e, the turbulence strength profiles of both components bulge at the cell boundaries, where the radial jet flows are located. Radially, the turbulence strength always peaks in the flow impingement region, which implies this region with a high shear rate. Then, the turbulence strength decreases in the direction of the jet flow to the minimum at the flow separation region. The maximum turbulence strength is observed in the impingement region of the outward jet flow (that is, near the inner cylinder), approximately 15% higher than the inward jet flow. The decrease in magnitude of the turbulence strength is obviously greater for the azimuthal velocity. It is concluded that this organized distribution of the turbulence strength is also attributed to the pairing of the Taylor vortex structure and the radial jet flows.

In a single Taylor roll cell, a minor asymmetry of the Taylor vortex structure is discovered, compared to TVF: first, the axial profiles of u_z are neither sinusoidal nor zero in the neutral plane of the annulus, as shown by fig. 4.4e; second, there is something somewhat oblique at the peaks of the sinusoidal curves of u_z at $(r-R_o)/d =$ 0.25, 0.75, as shown by figs. 4.4d and 4.4f.

More simply, these characteristics of the u_z profiles indicate a kind of distortion of the Taylor vortex structure, as shown by the velocity contours and streamline plots

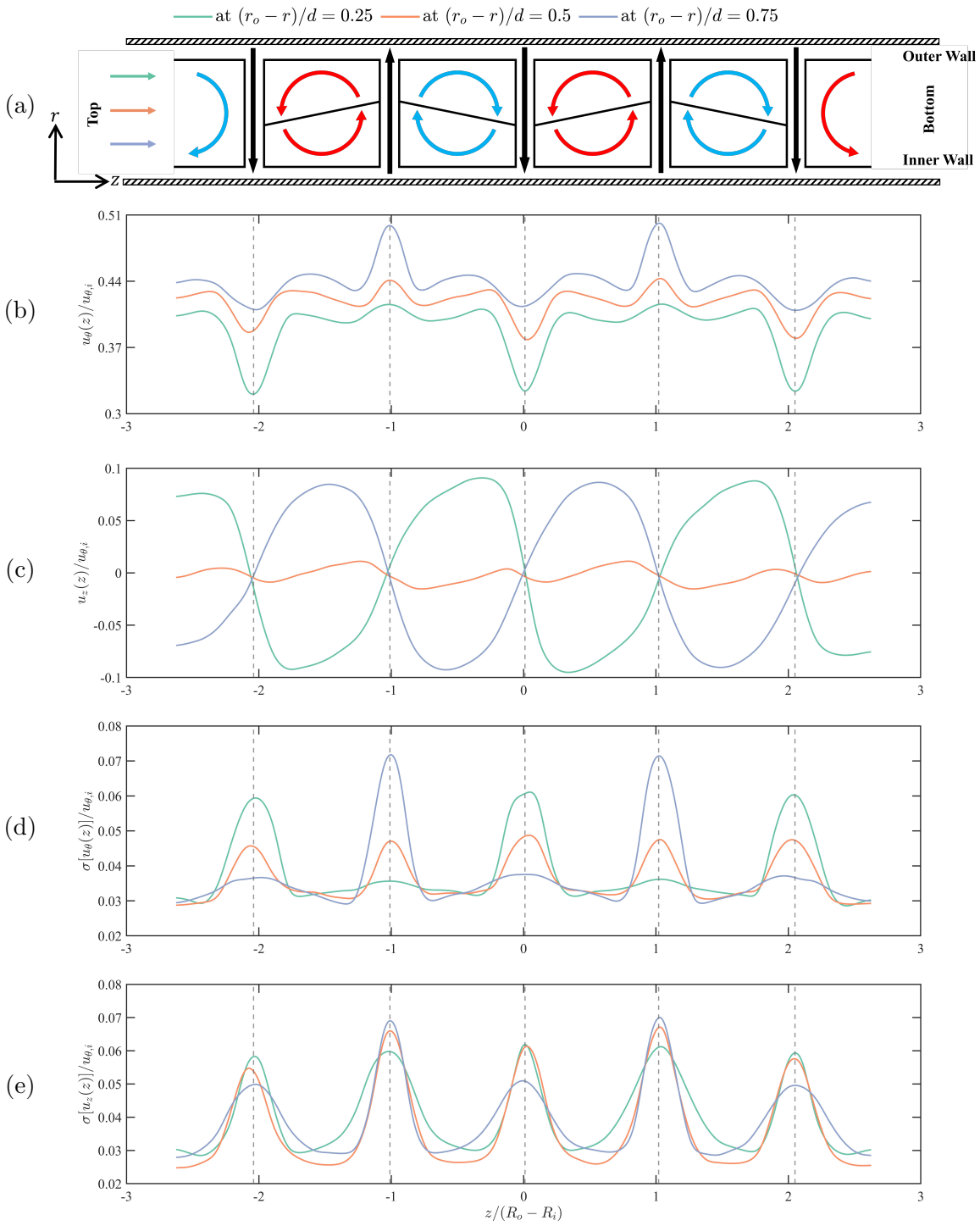

Figure 4.3: Newtonian TTV. (a)Schematic diagram of the Taylor vortex in $r - z$ plane. (b) Axial profiles of azimuthal velocity component. (c) Axial profiles of axial velocity component. (d) Axial profiles of turbulence strength of azimuthal velocity component. (e) Axial profiles of turbulence strength of axial velocity component.

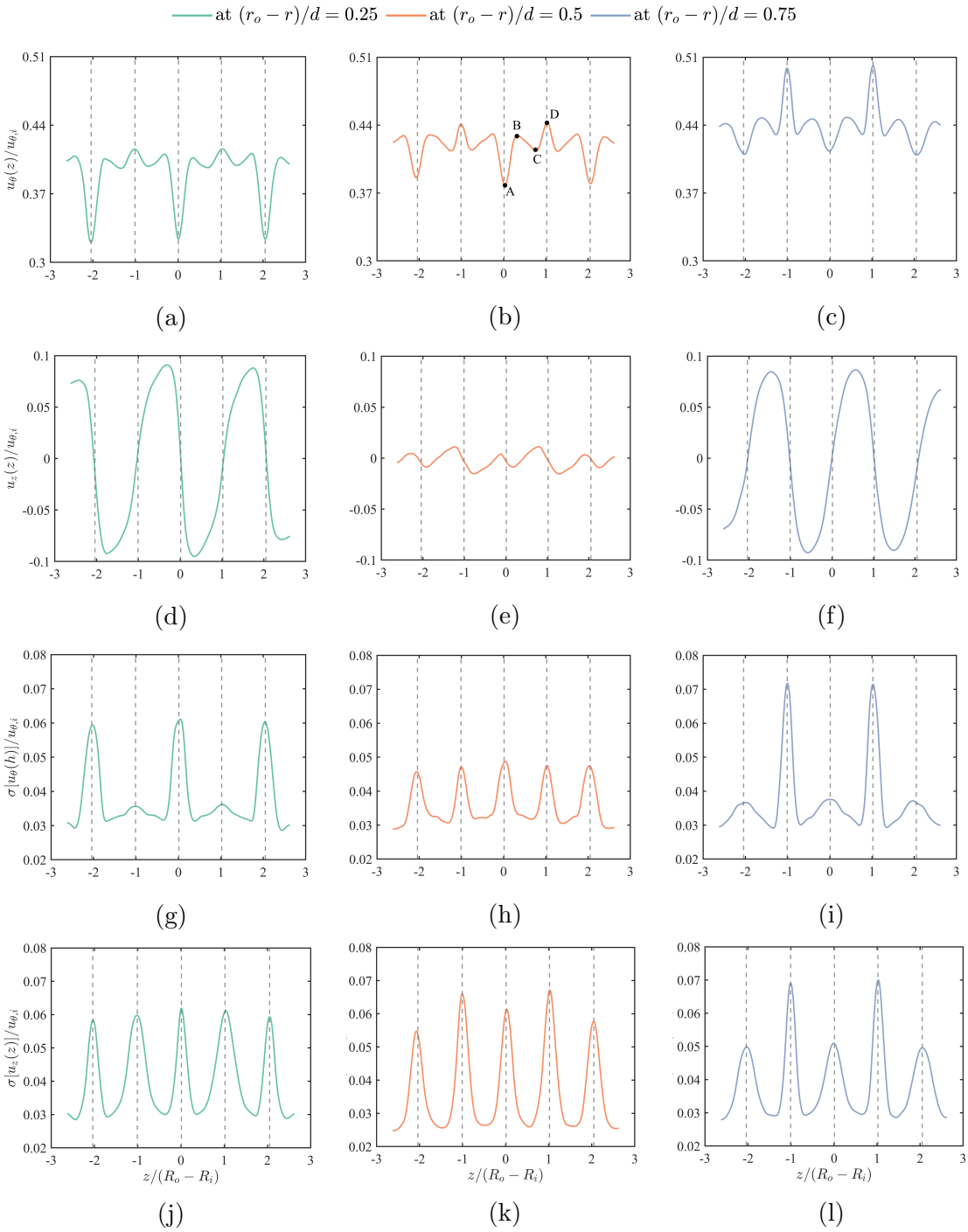

Figure 4.4: Separated profiles of the Newtonian TTV. The data are identical to fig. 4.3. (a-c)Schematic diagram of the Taylor vortex in $r-z$ plane. (d-f) Axial profiles of azimuthal velocity component. (g-i) Axial profiles of axial velocity component. (d) Axial profiles of turbulence strength of azimuthal velocity component. (j-l) Axial profiles of turbulence strength of axial velocity component.

in fig. 4.5. In the contours, the blue isolines represent the positive axial velocity (towards right) corresponding to the blue blocks in the streamline plots, and red represents negative. Radial jet flows are marked by black arrows in all subfigures. It would be appreciated that the contours require considerable interpolation, and it might be unwise to pay much attention to the relatively minor features. However, the distortion of the Taylor vortex structure is undoubtedly real, especially through the radial drift of the "neck" of the jet flows (as marked by the green dashed rectangle). This distortion results in a radial asymmetry compared to the TVF. However, the axial asymmetry in the TVF, with the eye of the vortex closer to the outward jet flow, is not observed in the TTV in this study.

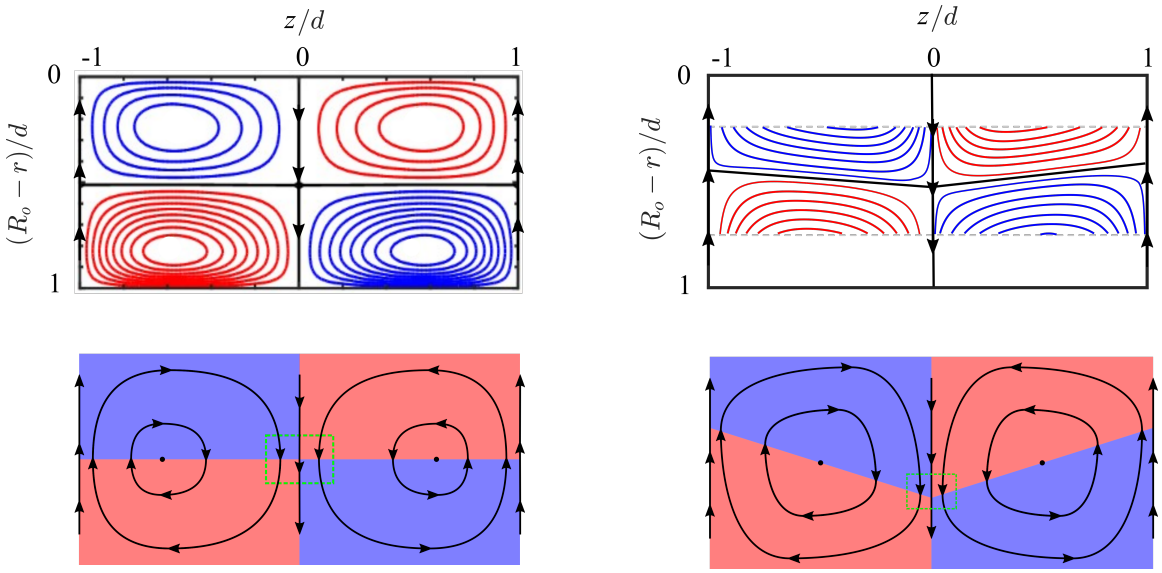

(a) TVF, [20] (b) TTV

Figure 4.5: Comparison between Newtonian TVF and TTV. Top: contours of u_z; bottom: schematics of the corresponding streamline, but the distortion magnitude is exaggerated.

With respect to the profiles of u_θ, for example, in fig. 4.4b, the velocity is extremed in jet flows: minimum at the inward jet flow (point A) and maximum at the outward jet flow (point D). However, there are a local maximum (point B) and a local minimum (point C) in between. In contrast, the behavior is pretty simple for TVF, which increases monotonically from the minimum at the inward jet flow to the maximum

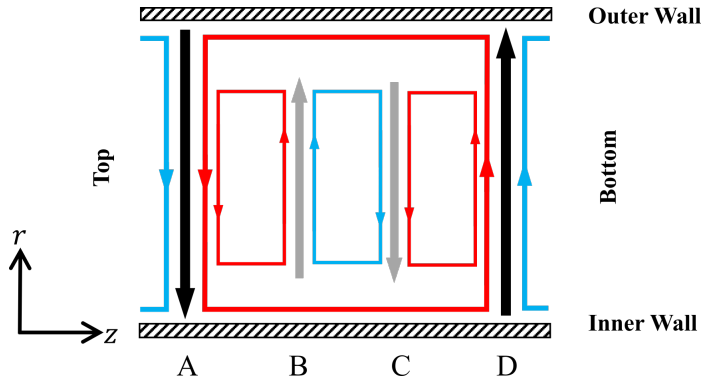

Figure 4.6: Sketch of the vortex structure in smaller scale inside a Taylor vortex

at the outward jet flow. Normally, the Taylor vortex is considered to be the largest vortex in TTV. Therefore, it is supposed that there might be vortices in a smaller scale existing inside the Taylor vortex. As depicted by fig. 4.6, three sub-vortices are included in one Taylor vortex, and sub-jets (gray arrows) formed between every two adjacent sub-vortices. These sub-jet flows also carry angular momentum radially but with a lower strength, which results in the local maximum and minimum inside one Taylor vortex as mentioned above.

4.2 Non-Newtonian Turbulent Taylor vortex flow

Same measurement procedures with section 4.1 were conducted to obtain the axial profiles of non-Newtonian fluids, and the results will be shown in a similar way in the next section.

4.2.1 0.4 wt.% Xanthan gum aqueous solution

In contrast to the Newtonian case, several distinctly different modes were discovered with the 0.4 wt.% xanthan gum aqueous solution.

As shown by fig. 4.7, when $Ew = 1170$, only one pair of complete Taylor vortices was observed within the measurement field. The effect of transport of angular momentum by radial jet flow causes the overshoot of u_θ, which is similar to the Newtonian case. The basic distribution of the turbulence strength also corresponds to the

Taylor vortex structure: higher turbulence in the flow impingement region and lower in the flow separation region.

However, there are still some differences between Non-Newtonian and Newtonian TTV: (1) the wavelength of the middle pair of vortices is approximately 4.2, obviously greater than Newtonian TTV. And two other vortices can be found at the margin of the measurement field, but they cannot be fully displayed due to the limited measurement field; (2) the vorticity of the Taylor vortex is apparently lower than in the Newtonian case, indicated by a much lower axial velocity at the same position; (3) the value of the turbulence strength is typically lower than in the Newtonian case, especially the turbulence strength of u_z, as compared by figs. 4.3e and 4.7e.

In fig. 4.8, as in $Re = 2200$, the main difference is that the observed Taylor vortices are not closely adjacent to each other. Normally, the region where $u_z \approx 0$ is regarded as the jet flow. So in fig. 4.8a, a wide gap between the two vortices can be observed for $-1 < z/(R_o - R_i) < 1$. At the same time, the high plateau of u_θ also agrees that a wide radial jet flow occupies this region. Lastly, the overall turbulence strength is lower than the Newtonian TTV, as shown by appendix B. Especially $\sigma(u_z)$ at the mid-gap is always kept at a very low level, even the jet flow has no obvious effect on it.

As Re increases to $2700 \sim 3700$, only one pair of vortices with a large wavelength can still be observed. Unlike $Re = 2200$, the Taylor vortices approach each other at $z/(R_o - R_i) = 0$ now. The effect of jet flow on the u_θ overshoot and the bulge of the turbulence strength is also validated in this case, except for the turbulence strength in the flow separation region: a decrease in $\sigma(u_\theta)$ is observed in the flow separation region, as shown by fig. 4.9e.

4.2.2 0.1 wt.% Xanthan gum aqueous solution

In this section, two different modes were discovered with the 0.1 wt.% Xanthan gum aqueous solution.

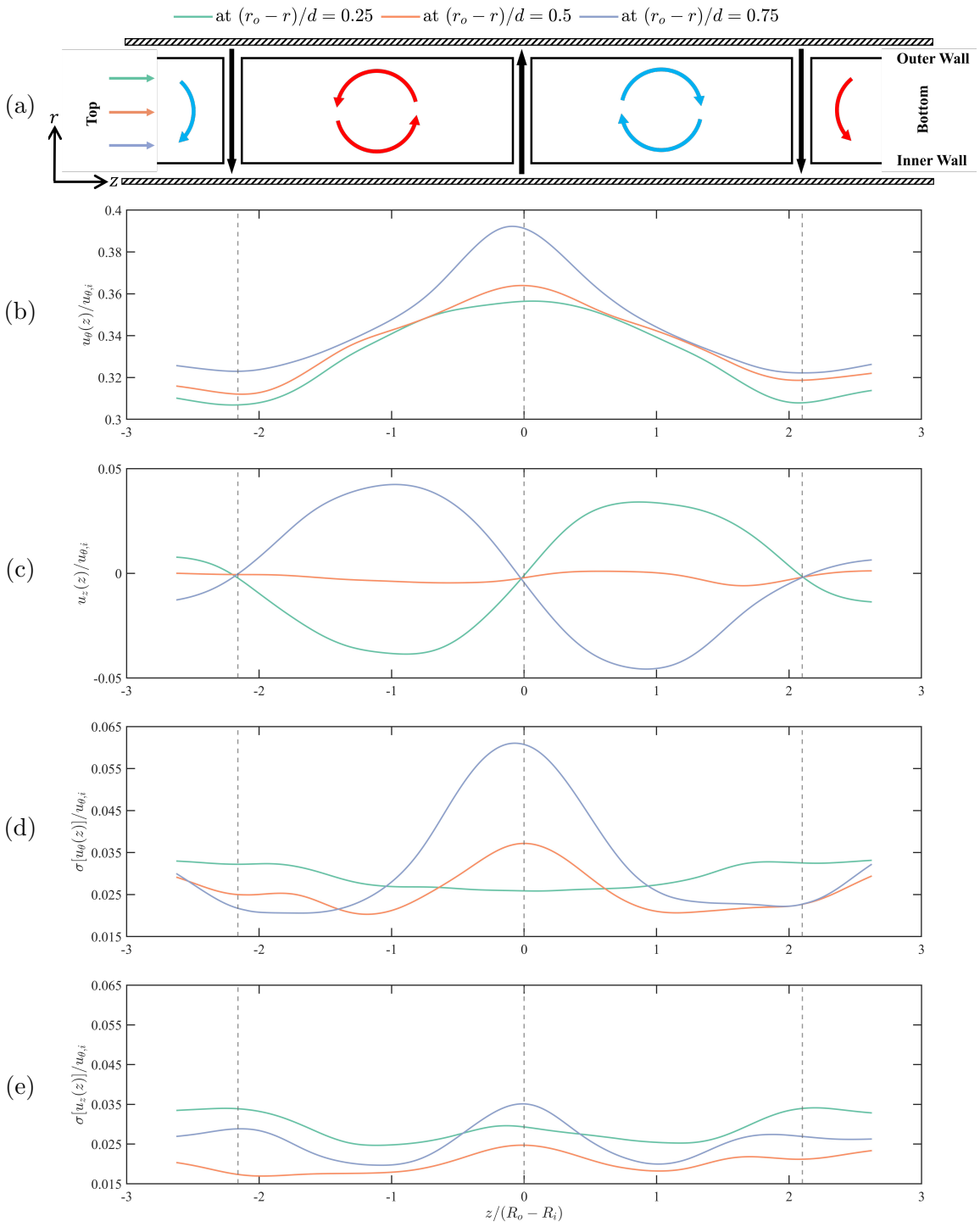

Figure 4.7: Non-Newtonian TTV with 0.4 wt.% Xanthan gum aqueous solution. $Re = 1170$. (a)Schematic diagram of the Taylor vortex in $r - z$ plane. Axial profiles of (b) the azimuthal velocity component, (c) axial velocity component, (d) the turbulence strength of the azimuthal velocity component, (e) the turbulence strength of the axial velocity component.

For $Re = 3600$, 4100, Taylor vortices with unequal wavelength exist in the flow at the same time. As shown by fig. 4.10a, the wavelength of the middle pair of vortices is about 2.8, and about 1.8 for those at the margin of the measurement field. According to fig. 4.10b, the overshoot resulted by jet flow is still distinguishable mainly at the flow impingement region, while at the flow separation region, the overshoot is too weak to be observed. Similar behavior also can be found in fig. 4.10d: bulges of the profiles of $\sigma(u_\theta)$ can be distinguished at the flow impingement region and the middle of the gap, while the bulges are no more obvious at the flow separation region. These may suggest that the jet flows attenuate more quickly due to the high viscosity at the bulk region in Non-Newtonian TTV.

In fig. 4.11, the Taylor vortex structure becomes different again. The wavelength of approximately 2.7 of the middle pair of vortices is observed, and the wavelength of the marginal pair is apparently larger, but the value is not obtained due to the limited measurement field. The mechanisms of azimuthal velocity overshoot and bulges of the turbulence strength profiles are similar to $Re = 3600$, 4100 in fig. 4.10

However, in this case ($Re = 4900$, 6000 and 7000), the most notably difference is that the jet flow direction at the mid-height ($z = 0$) is inward. While for all other Newtonian cases, the direction is inward, including the 0.4 wt.% Xanthan gum aqueous solution. This reminds the two different modes in the radial profiles discussed in Chapter 3: the radial profiles of azimuthal velocity, shear rate, viscosity and turbulence strength can be classified into two corresponding groups, $Re = 3600$, 4100 and $Re = 4900$, 6000 *and* 7000. Now it is quite clear that the discrepancy between the radial profiles is resulted by different Taylor vortex structure, or more specifically, the different direction of the jet flow at the mid-height.

4.3 Summary

In this chapter, the time-averaged axial profiles and mapping of the Taylor vortex structure of one Newtonian fluid and two Non-Newtonian fluids were presented. The

relationship between Taylor vortex structure and periodicity of axial profiles of velocity and turbulence strength was analyzed. A hypothesis of vortices with smaller scale existing inside Taylor vortex was proposed. Comparisons of the axial profiles and Taylor vortex structure, between Newtonian TVF and TTV, Newtonian and Non-Newtonian TTV were conducted. At last, a connection between the Taylor vortex structure and radial profiles was discovered.

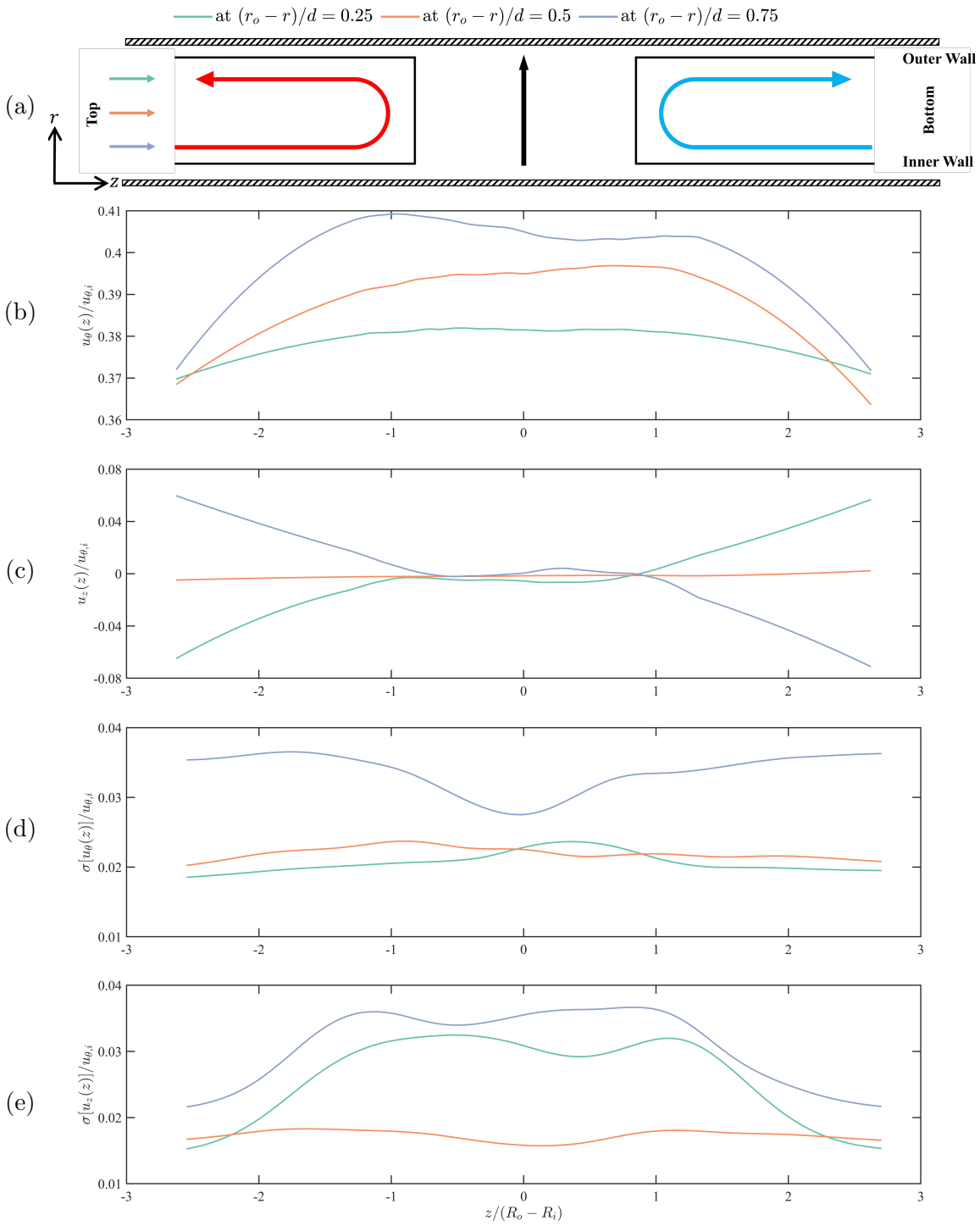

Figure 4.8: Non-Newtonian TTV with 0.4 wt.% Xanthan gum aqueous solution. $Re = 2200$. (a)Schematic diagram of the Taylor vortex in $r - z$ plane. Axial profiles of (b) the azimuthal velocity component, (c) axial velocity component, (d) the turbulence strength of the azimuthal velocity component, (e) the turbulence strength of the axial velocity component. $Re = 1700$ is in the same mode and has similar profiles with $Re = 2200$, which is attached in the appendix.

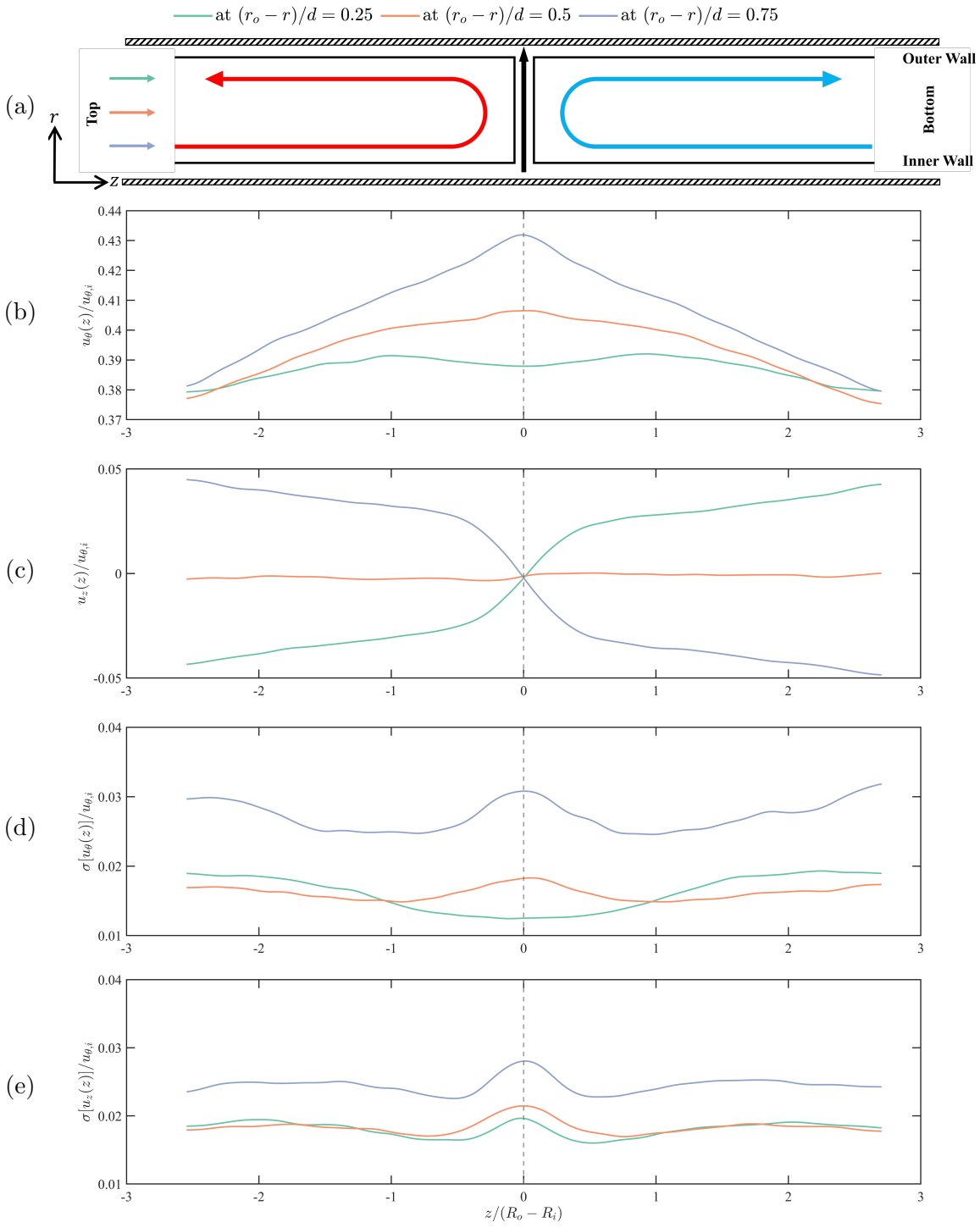

Figure 4.9: Non-Newtonian TTV with 0.4 wt.% Xanthan gum aqueous solution. $Re = 3700$. (a)Schematic diagram of the Taylor vortex in $r - z$ plane. Axial profiles of (b) the azimuthal velocity component, (c) axial velocity component, (d) the turbulence strength of the azimuthal velocity component, (e) the turbulence strength of the axial velocity component. $Re = 2700$, 3200 are in the same mode and has similar profiles to $Re = 3700$, which are attached in the appendix.

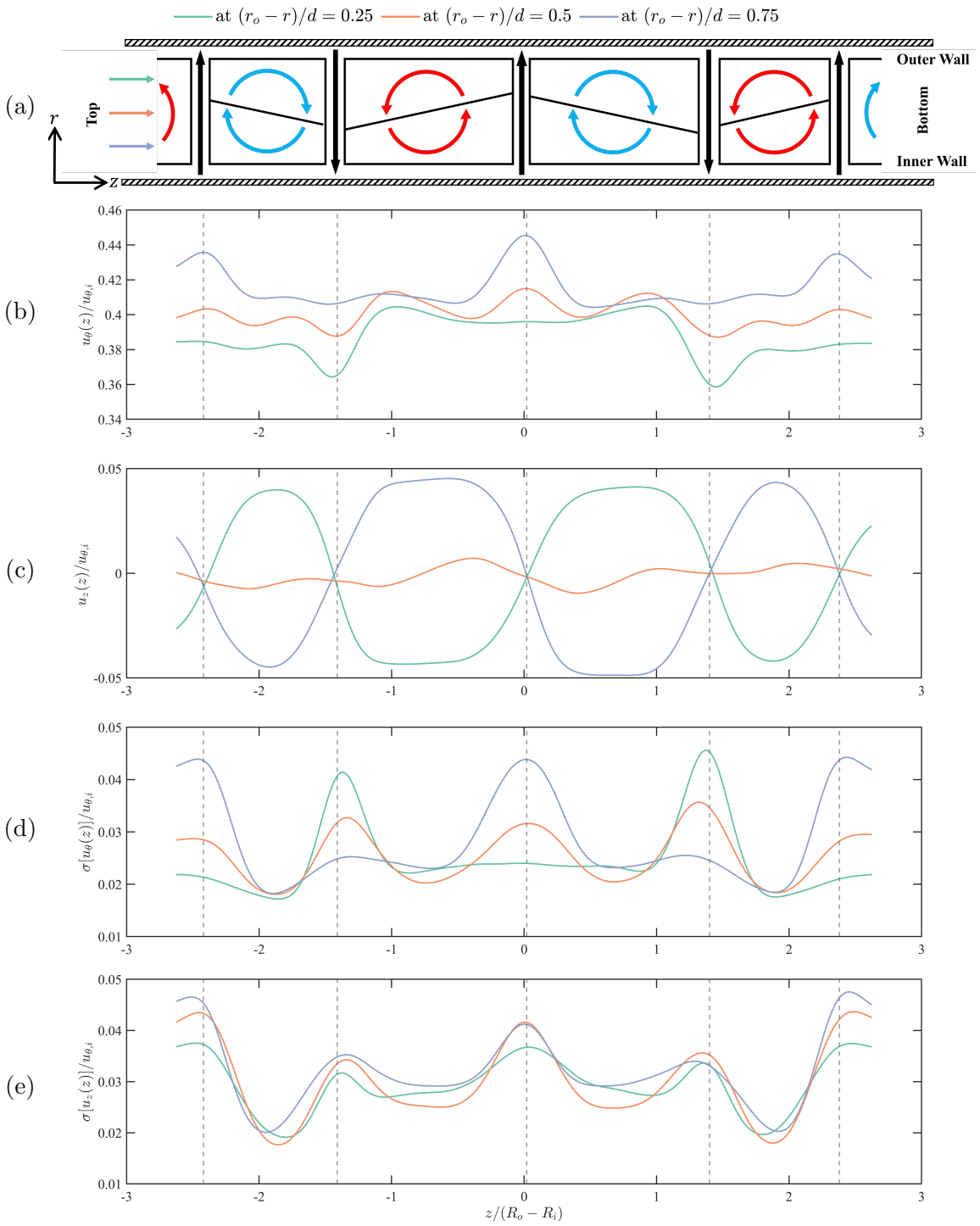

Figure 4.10: Non-Newtonian TTV with 0.1 wt.% Xanthan gum aqueous solution. $Re = 4100$. (a)Schematic diagram of the Taylor vortex in $r - z$ plane. Axial profiles of (b) the azimuthal velocity component, (c) axial velocity component, (d) the turbulence strength of the azimuthal velocity component, (e) the turbulence strength of the axial velocity component. $Re = 3600$ is in the same mode and has similar profiles with $Re = 4100$, which is attached in the appendix.

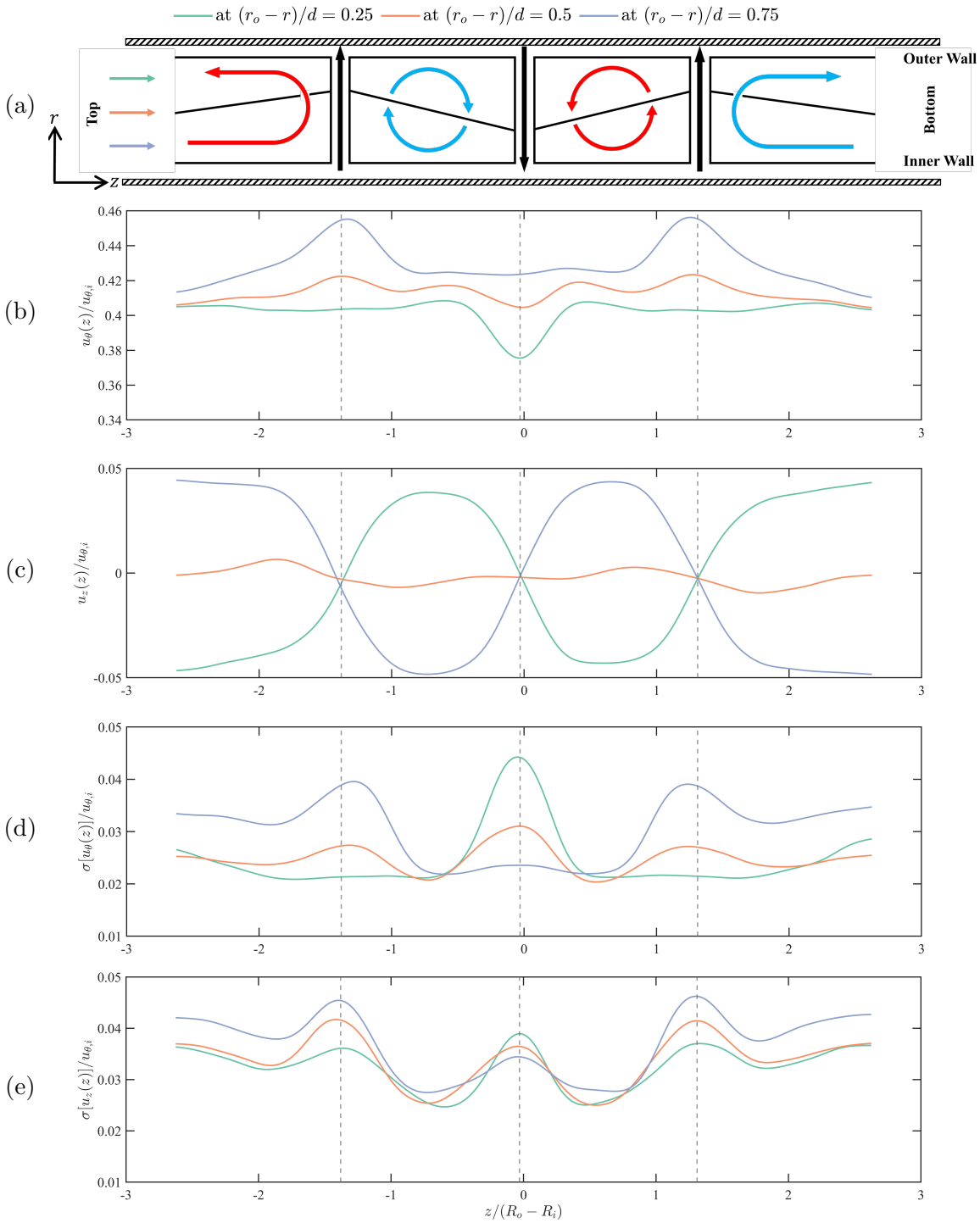

Figure 4.11: Non-Newtonian TTV with 0.1 wt.% Xanthan gum aqueous solution. $Re = 4900$. (a)Schematic diagram of the Taylor vortex in the $r - z$ plane. Axial profiles of (b) the azimuthal velocity component, (c) the axial velocity component, (d) the turbulence strength of the azimuthal velocity component, and (e) the turbulence strength of the axial velocity component. $Re = 6000$, 7000 are in the same mode and have profiles similar to $Re = 3700$, which are attached in the Appendix.

Chapter 5

Conclusions

5.1 Conclusions

The main objective of this study was to investigate the flow field of Newtonian and non-Newtonian TTV based on LDV measurement.

First, a compensation method to provide a flat refraction interface for the laser was developed by adding a viewing chamber to the outer surface of the setup. The separation distance between the measurement volumes could be reduced to less than 2.5% of the annulus width. Additionally, the conversion relationship from the displacement of the laser probe to the measurement volumes was also derived, which is essential to draw the correct flow profiles later. The rheological test results of the non-Newtonian working fluids were fitted to the Power-law model and the Carreau model to evaluate the shear thinning behavior of the working fluids. Later, the effect of the viscosity plateau in basic laminar TC flow was analyzed, and it was found that the viscosity plateau did not have an obvious effect on our flow.

In Chapter 3, at first, the shear-thinning effect on radial profiles was discussed analytically and numerically in the basic laminar TC flow. The results show that a stronger shear thinning behavior has a similar effect as a smaller radius ratio that makes the curves concave downward, and this effect can be superimposed by both factors. Then the radial profiles at the midheight of the setup were exhibited. The measurement results were fitted to piecewise polynomials with essential constraints.

Therefore, the radial profiles of shear rate as well as viscosity could be derived after obtaining the expression of the velocity profiles. These profiles show that a "sandwich" structure, composed of one bulk region with high viscosity in the middle of the flow and two near-wall regions with low viscosity, is more distinguished with increasing Reynolds number in non-Newtonian flows. Finally, the radial profiles of the local Reynolds number were displayed, and obvious discrapency was revealed compared to the basic laminar TC flow. This suggests that using the basic laminar TC flow profiles to modify the Reynolds number of the non-Newtonian TC flow [13] may not be valuable because it cannot capture the real local Reynolds number distribution of the turbulent TC flow.

In Chapter 4, the Taylor vortex structure inside the flow was revealed on the basis of the axial profiles and found to be widespread. The periodicity of the profiles caused by the Taylor vortex structure was discussed and a 90 deg lag between the azimuthal velocity and the axial velocity profiles was found. In Newtonian TTV, only one mode with consistent spatial wavelength of the Taylor vortex was found. However, several different modes with varying wavelength were discovered in the non-Newtonian case. It is worth mentioning that the two modes found in non-Newtonian TTV with the 0.1 wt% XG solution have the opposite direction of the radial jet flow at midheight. This recalls the corresponding behavior of the radial profiles mentioned in Chapter 3 and demontrates the radial transport of the angular momentum by jet flow.

5.2 Future Considerations

Although the experimental work was finished and abundant data was obtained to display the varying structure in TTF, some problems and defects still arose and made the work imperfect. Therefore, some ideals and suggestions for future work are given as follows:

- Change the placement of the LDV probe. The cylindrical wall with finite thick-

ness makes it impossible to measure the two velocity components simultaneously using LDV. Therefore, it is suggested to set the LDV probe above the top plate of the setup in the axial direction. In this way, the laser will only refract at the top flat plate, which can prevent the separation of the measurement volumes and enable simultaneous measurement of two velocity components. In this way, a Reynolds stress component $\overline{u'_\theta u'_r}$ can be obtained.

- Obtain the profiles by using PIV. Considering that LDV measures the local velocity of discrete spacious points, obtaining flow profiles is quite inefficient. In contrast, PIV would be a more productive method to obtain the profiles.

- Investigate the energy spectrum of the flow using LDV. The strength of LDV is its high temporal resolution. Therefore, spectral dynamics of turbulence should be a valuable topic if the temporal resolution of the LDV measurement can be guaranteed.

Bibliography

[1] "VIII. stability of a viscous liquid contained between two rotating cylinders," *Philosophical Transactions of the Royal Society of London. Series A, Containing Papers of a Mathematical or Physical Character*, vol. 223, pp. 289–343, 605-615 Jan. 1923.

[2] J. E. Burkhalter and E. L. Koschmieder, "Steady supercritical taylor vortex flow," 1973, Measure the Taylor vortex ring length with increasing Taylor, pp. 547–560.

[3] D. Coles, "Transition in circular couette flow," *Journal of Fluid Mechanics*, vol. 21, pp. 385–425, 3 1965.

[4] J. A. Cole, "Taylor-vortex instability and annulus-length effects," *Journal of Fluid Mechanics*, vol. 75, pp. 1–15, 1 1976.

[5] S. J. Muller, "Elastically-influenced instabilities in taylor-couette and other flows with curved streamlines: A review," *Korea Australia Rheology Journal*, vol. 20, pp. 117–125, 3 2008, Review¡br/¿elasticity on TC flow.

[6] C. A. Jones, "The transition to wavy taylor vortices," *Journal of Fluid Mechanics*, vol. 157, pp. 135–162, 1985, Numerical calculation.

[7] S. T. Wereley and R. M. Lueptow, "Velocity field for taylor-couette flow with an axial flow," *Physics of Fluids*, vol. 11, pp. 3637–3649, 12 Dec. 1999, PIV with RIM r-z plan velocity profile contour.

[8] H. L. Swinney, "Flow regimes in a circular couette system with independently rotating cylinders," *Journal of Fluid Mechanics*, vol. 164, pp. 155–183, 1986.

[9] A. Brandstater and H. L. Swinney, "Strange attractors in weakly turbulent couette-taylor flow," *Physical Review A*, vol. 35, pp. 2207–2220, 5 1987, early PIV on tc flow¡br/¿need read.

[10] A. Lindner, D. Bonn, and J. Meunier, "Viscous fingering in a shear-thinning fluid," *Physics of Fluids*, vol. 12, p. 256, 2 Jan. 2000.

[11] H. Masuda, T. Horie, R. Hubacz, M. Ohta, and N. Ohmura, "Prediction of onset of taylor-couette instability for shear-thinning fluids," *Rheologica Acta 2016 56:2*, vol. 56, pp. 73–84, 2 Dec. 2016.

[12] B Güzel, I Frigaard, and D. Martinez, "Predicting laminar–turbulent transition in poiseuille pipe flow for non-newtonian fluids," *Chemical Engineering Science*, vol. 64, no. 2, pp. 254–264, 2009.

[13] H. Elçiçek and B. Güzel, "Effect of shear-thinning behavior on flow regimes in taylor–couette flows," *Journal of Non-Newtonian Fluid Mechanics*, vol. 279, May 2020.

[14] O. Coronado-Matutti, P. R. Mendes, and M. S. Carvalho, "Instability of inelastic shear-thinning liquids in a couette flow between concentric cylinders," *Journal of Fluids Engineering, Transactions of the ASME*, vol. 126, pp. 385–390, 3 May 2004.

[15] N. Ashrafi, "Stability analysis of shear-thinning flow between rotating cylinders," *Applied Mathematical Modelling*, vol. 35, pp. 4407–4423, 9 Sep. 2011.

[16] B. Alibenyahia, C. Lemaitre, C. Nouar, and N. Ait-Messaoudene, "Revisiting the stability of circular couette flow of shear-thinning fluids," *Journal of Non-Newtonian Fluid Mechanics*, vol. 183-184, pp. 37–51, Sep. 2012.

[17] N. Cagney and S. Balabani, "Taylor-couette flow of shear-thinning fluids," *Physics of Fluids*, vol. 31, p. 53 102, 5 May 2019.

[18] T. J. Lockett, S. M. Richardson, and W. J. Worraker, "The stability of inelastic non-newtonian fluids in couette flow between concentric cylinders: A finite-element study," *Journal of Non-Newtonian Fluid Mechanics*, vol. 43, pp. 165–177, 2-3 Jul. 1992.

[19] Y. Agbessi, B. Alibenyahia, C. Nouar, C. Lemaitre, and L. Choplin, "Linear stability of taylor–couette flow of shear-thinning fluids: Modal and non-modal approaches," *Journal of Fluid Mechanics*, vol. 776, pp. 354–389, Aug. 2015.

[20] S Topayev, C Nouar, D Bernardin, A Neveu, and S. A. Bahrani, "Taylor-vortex flow in shear-thinning fluids," *Physical Review E*, vol. 100, 2019.

[21] M. P. Escudier, I. W. Gouldson, and D. M. Jones, "Taylor vortices in newtonian and shear-thinning liquids," *Proceedings - Royal Society of London, A*, vol. 449, pp. 155–176, 1935 1995, Xantham gum ¡br/¿LDV.

[22] N. Cagney and S. Balabani, "Influence of shear-thinning rheology on the mixing dynamics in taylor-couette flow," *Chemical Engineering and Technology*, vol. 42, pp. 1680–1690, 8 Aug. 2019.

[23] M. P. Escudier, I. W. Gouldson, and D. M. Jones, "Taylor vortices in newtonian and shear-thinning liquids," *Proceedings - Royal Society of London, A*, vol. 449, pp. 155–176, 1935 1995.

[24] G. S. Lewis and H. L. Swinney, "Velocity structure functions, scaling, and transitions in high-reynolds-number couette-taylor flow," *Physical Review E - Statistical Physics, Plasmas, Fluids, and Related Interdisciplinary Topics*, vol. 59, pp. 5457–5467, 5 1999, Torque measurements included¡br/¿Comparision bt model and exp data.

[25] D. P. Lathrop, J. Fineberg, and H. L. Swinney, "Transition to shear-driven turbulence in couette-taylor flow," *Physical Review A*, vol. 46, pp. 6390–6405, 10 Nov. 1992.

[26] E. Koschmieder, "Turbulent taylor vortex flow," *Journal of Fluid Mechanics*, vol. 93, no. 3, pp. 515–527, 1979.

[27] G. P. Smith and A. A. Townsend, "Turbulent couette flow between concentric cylinders at large taylor numbers," *Journal of Fluid Mechanics*, vol. 123, pp. 187–217, 1982, detailed experiment.

[28] A. Barcilon, J. Brindley, M. Lessen, and F. R. Mobbs, "Marginal instability in taylor–couette flows at a very high taylor number," *Journal of Fluid Mechanics*, vol. 94, pp. 453–463, 3 1979.

[29] K. Coughlin and P. S. Marcus, "Turbulent bursts in couette-taylor flow," *Physical Review Letters*, vol. 77, p. 2214, 11 Sep. 1996.

[30] J. A. Vastano and R. D. Moser, "Short-time lyapunov exponent analysis and the transition to chaos in taylor–couette flow," *Journal of Fluid Mechanics*, vol. 233, pp. 83–118, 83 1991.

[31] M. Bilson and K. Bremhorst, "Direct numerical simulation of turbulent taylor–couette flow," *Journal of Fluid Mechanics*, vol. 579, pp. 227–270, May 2007.

[32] S. Dong, "Direct numerical simulation of turbulent taylor–couette flow," *Journal of Fluid Mechanics*, vol. 587, pp. 373–393, Sep. 2007, DNS simulation of turbulent tc flow.¡br/¿Comparison between instentaneous and time averaged r-z structure.

[33] R. Ostilla-Mónico, E. P. van der Poel, R. Verzicco, S. Grossmann, and D. Lohse, "Boundary layer dynamics at the transition between the classical and the ultimate regime of taylor-couette flow," *Physics of Fluids*, vol. 26, p. 015 114, 1 Jan. 2014.

[34] S. Huisman, R. Van der Veen, C Sun, and D Lohse, "Multiple states in ultimate taylor-couette turbulence," *Nature Comm*, vol. 5, p. 3820, 2014.

[35] M. J. Burin *et al.*, "Reduction of ekman circulation within taylor-couette flow," *Experiments in Fluids*, vol. 40, pp. 962–966, 6 2006.

[36] Z. Zhang, *LDA Application Methods*. Springer Berlin Heidelberg, Aug. 2010, pp. 331–341, Citation should be from university libarary¡br/¿Guidebook for LDA.

[37] Z. Z. E. Parkinson, "Lda application and the dual-measurement-method in experimental investigations of the free surface jet at a model nozzle of a pelton turbine," *11th International Symposium on Applications of Laser Anemometry to Fluid Mechanics*, pp. 1–7, 2002.

[38] S. G. Huisman, D. P. V. Gils, and C. Sun, "Applying laser doppler anemometry inside a taylor-couette geometry using a ray-tracer to correct for curvature effects," *European Journal of Mechanics, B/Fluids*, vol. 36, pp. 115–119, 2012, Laser correction.

[39] P. S. Marcus, "Simulation of taylor-couette flow. part 1. numerical methods and comparison with experiment," *Journal of Fluid Mechanics*, vol. 146, pp. 45–64, 1984.

[40] F. Wendt, "Turbulente strömungen zwischen zwei rotierenden konaxialen zylindern," *Ingenieur-Archiv 1933 4:6*, vol. 4, pp. 577–595, 6 Dec. 1933.

Appendix A: Comparison between Re, Re_G and $Re_G{}'$

As discussed in section 3.4, different Reynolds number can be accessed due to different selections of the visocosity reference scale. This appendix shows the detailed comparison between them and the corresponding relationship with dimentionless torque in figure.

Re	1100	1550	2200	2750	3200
Re_G	313	454	714	926	1163
Re_{GB}	494	706	988	1245	1439
Re_G / Re	0.29	0.29	0.33	0.34	0.37
G($\times 10^6$)	0.45	0.74	1.21	1.71	2.11

Table A.1: Table of water-glycerin mixture (Newtonian).

Re	700	1170	1700	2200	2700	3200	3700
Re_G	171	280	409	473	634	719	815
Re_{GB}	302	505	733	967	1199	1420	1654
Re_G / Re	0.25	0.24	0.24	0.21	0.23	0.22	0.22
μ_{ref}	0.0572	0.0461	0.0396	0.0354	0.0324	0.0303	0.0285
μ_G	0.1867	0.1447	0.1209	0.1113	0.0887	0.0848	0.0808
μ_{GB}	0.0786	0.0634	0.0544	0.0486	0.0446	0.0416	0.0392
μ_G/μ_{ref}	3.26	3.14	3.05	3.15	2.74	2.80	2.83
$\mathrm{G}(\times 10^5)$	2.07	2.00	3.60	6.03	7.97	9.80	11.89
$\mathrm{G}_G(\times 10^5)$	0.19	0.20	0.39	0.61	1.06	1.25	1.48
$\mathrm{G}_{GB}(\times 10^5)$	1.10	1.06	1.91	3.20	4.21	5.20	6.28
G_G / G	0.09	0.10	0.11	0.10	0.13	0.13	0.12

Table A.2: Table of 0.4 wt.% XG aqueous solution (shear-thnning).

Re	3600	4100	4900	6000	7000
Re_G	1073	1215	1287	1581	1853
Re_{GB}	1645	1883	2265	2766	3226
Re_G / Re	0.30	0.30	0.26	0.26	0.26
μ_{ref}	0.0110	0.0106	0.0101	0.0096	0.0093
μ_G	0.0175	0.0169	0.0159	0.0151	0.0146
μ_{GB}	0.0108	0.0104	0.0099	0.0095	0.0091
μ_G/μ_{ref}	1.60	1.60	1.57	1.57	1.57
$\mathrm{G}(\times 10^6)$	3.56	3.13	4.90	6.73	8.17
$\mathrm{G}_G(\times 10^6)$	1.41	1.23	1.98	2.72	3.32
$\mathrm{G}_{GB}(\times 10^6)$	3.69	3.25	5.10	6.87	8.54
G_G / G	0.39	0.39	0.40	0.40	0.40

Table A.3: Table of 0.1 wt.% XG aqueous solution (shear-thnning).

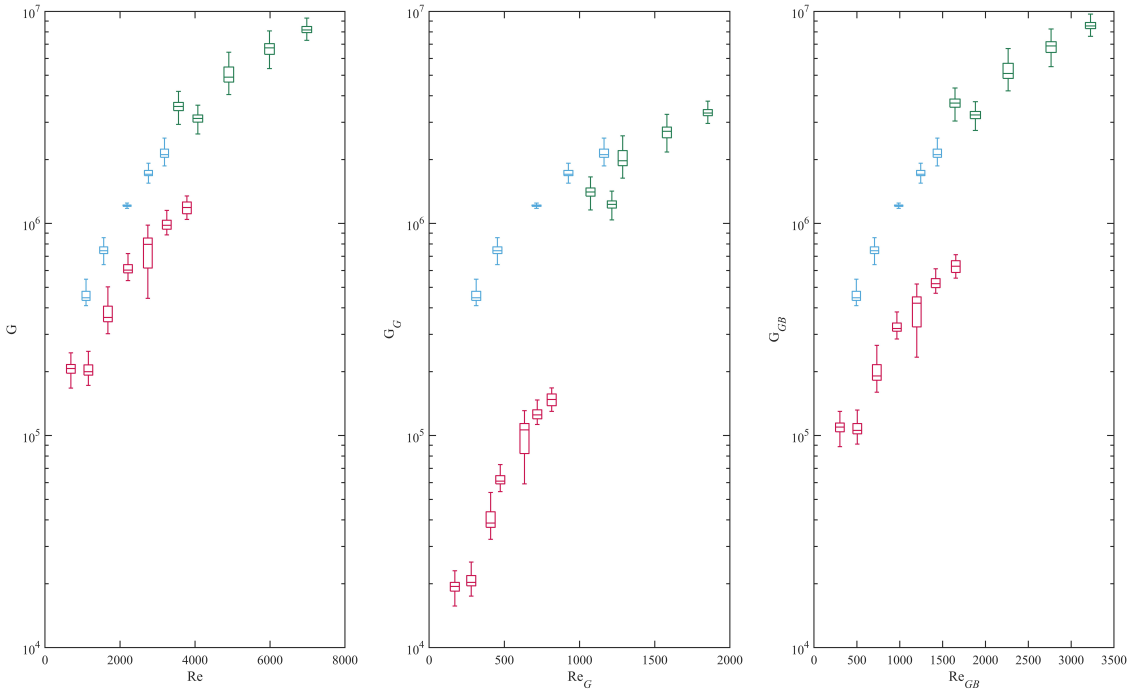

(a) (b) (c)

Figure A.1: Experimental measurements for the dimensionless torque versus Reynolds number. Measurements with different working fluids are distinguished by color. Blue: $n = 1$, Newtonian solution; Green: $n = 0.51$, corresponds to 0.1 wt.% Xanthan gum aqueous solution; Red: $n = 0.22$, corresponds to 0.4 wt.% Xanthan gum aqueous solution.(a) G vs Re; (b) G_{GB} vs Re_{GB}; (c) G_{GB} vs Re_{GB}.

Appendix B: Supplymentray figures for Chapter 4

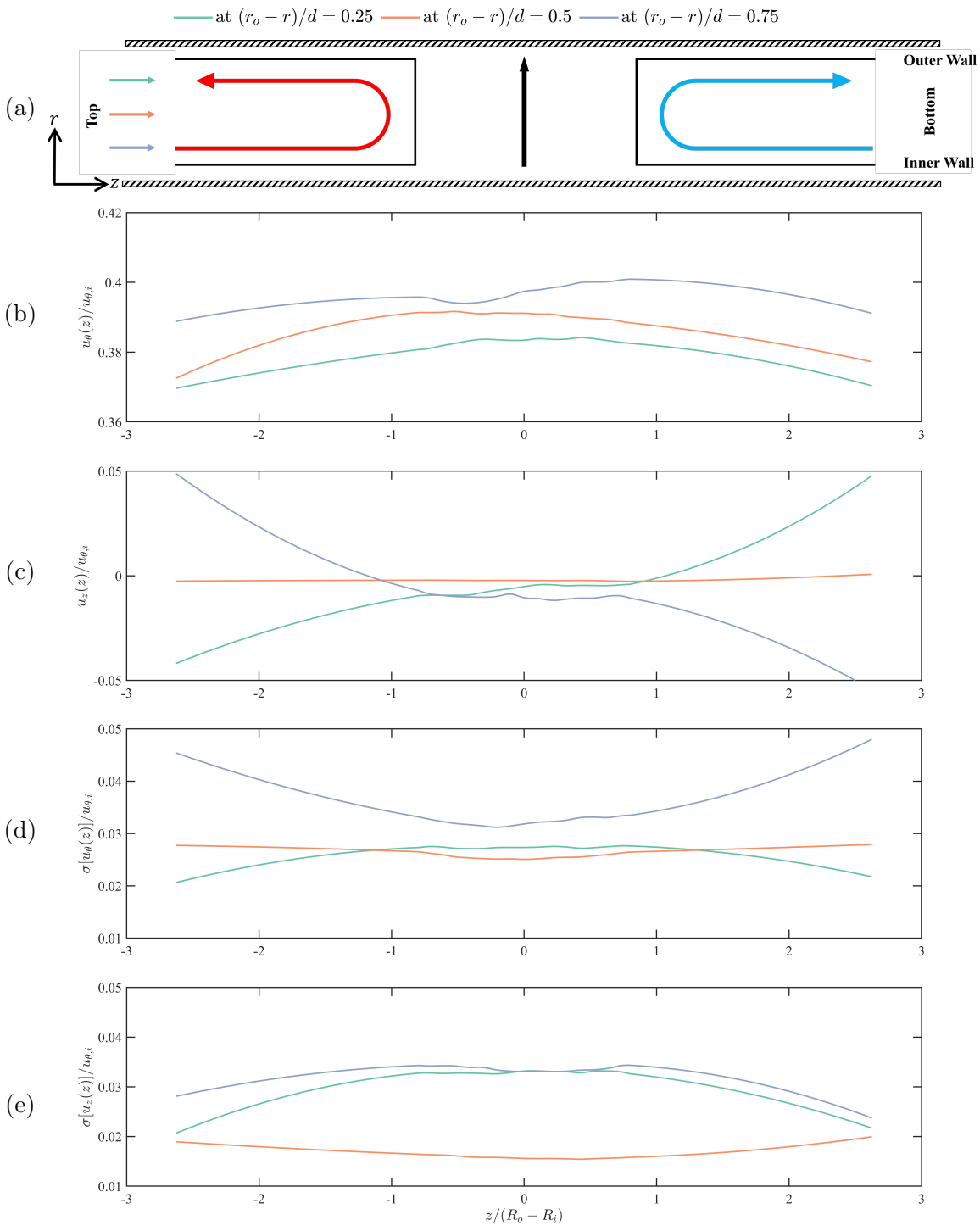

Figure B.1: Non-Newtonian TTV with 0.4 wt.% Xanthan gum aqueous solution. $Re = 1700$. (a)Schematic diagram of the Taylor vortex in $r - z$ plane. Axial profiles of (b) the azimuthal velocity component, (c) axial velocity component, (d) the turbulence strength of the azimuthal velocity component, (e) the turbulence strength of the axial velocity component.

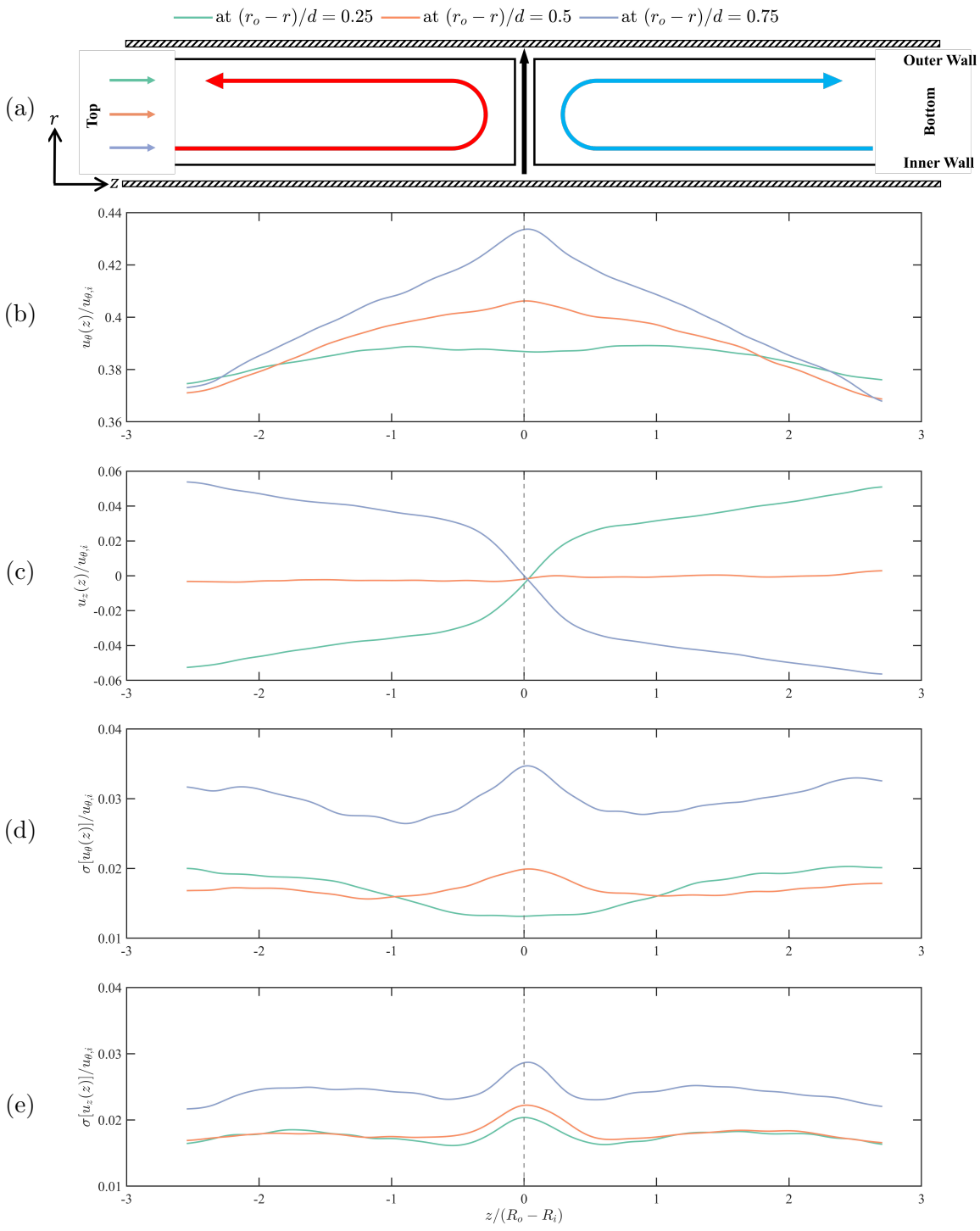

Figure B.2: Non-Newtonian TTV with 0.4 wt.% Xanthan gum aqueous solution. $Re = 2700$. (a)Schematic diagram of the Taylor vortex in $r - z$ plane. Axial profiles of (b) the azimuthal velocity component, (c) axial velocity component, (d) the turbulence strength of the azimuthal velocity component, (e) the turbulence strength of the axial velocity component.

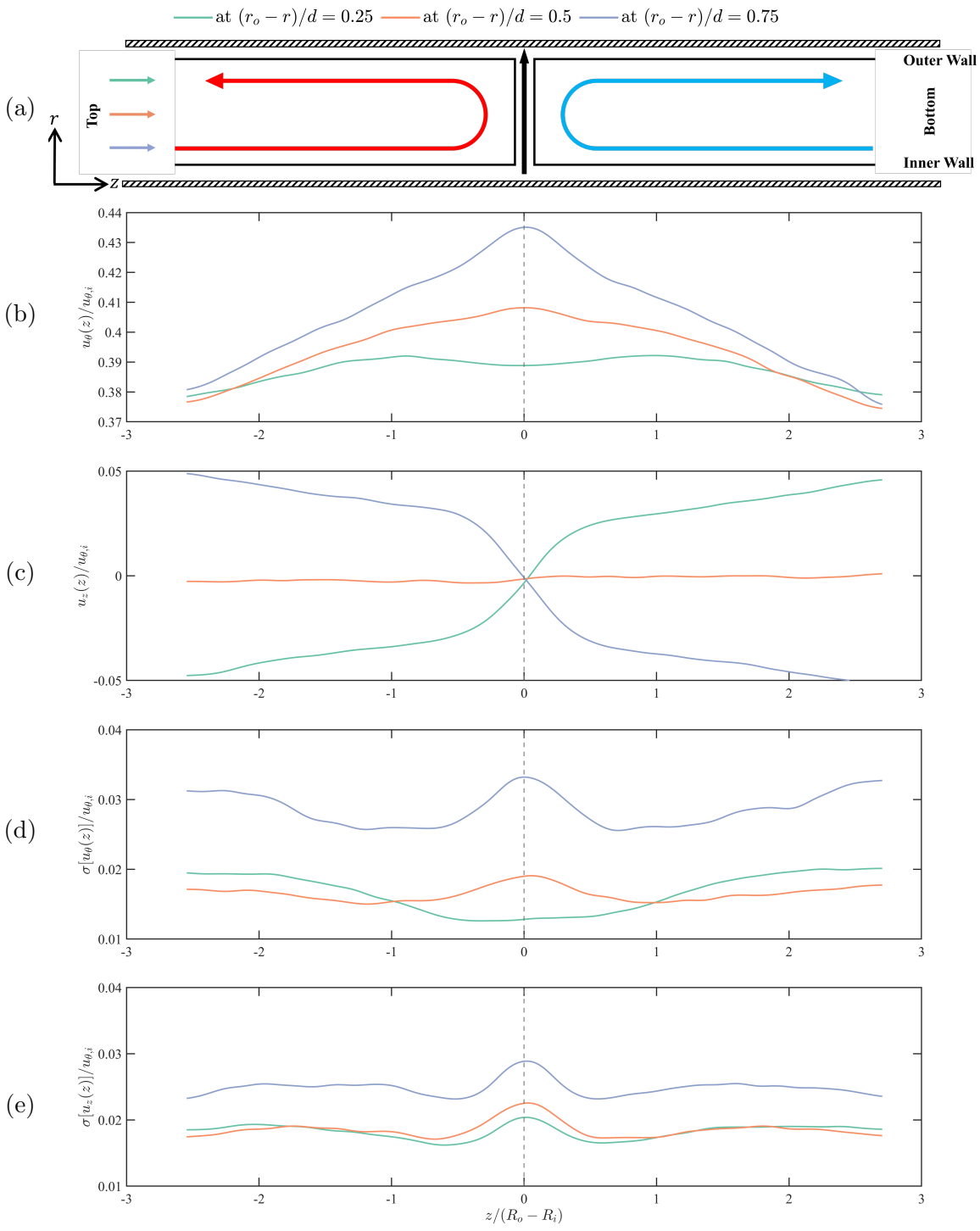

Figure B.3: Non-Newtonian TTV with 0.4 wt.% Xanthan gum aqueous solution. $Re = 3200$. (a)Schematic diagram of the Taylor vortex in $r - z$ plane. Axial profiles of (b) the azimuthal velocity component, (c) axial velocity component, (d) the turbulence strength of the azimuthal velocity component, (e) the turbulence strength of the axial velocity component.

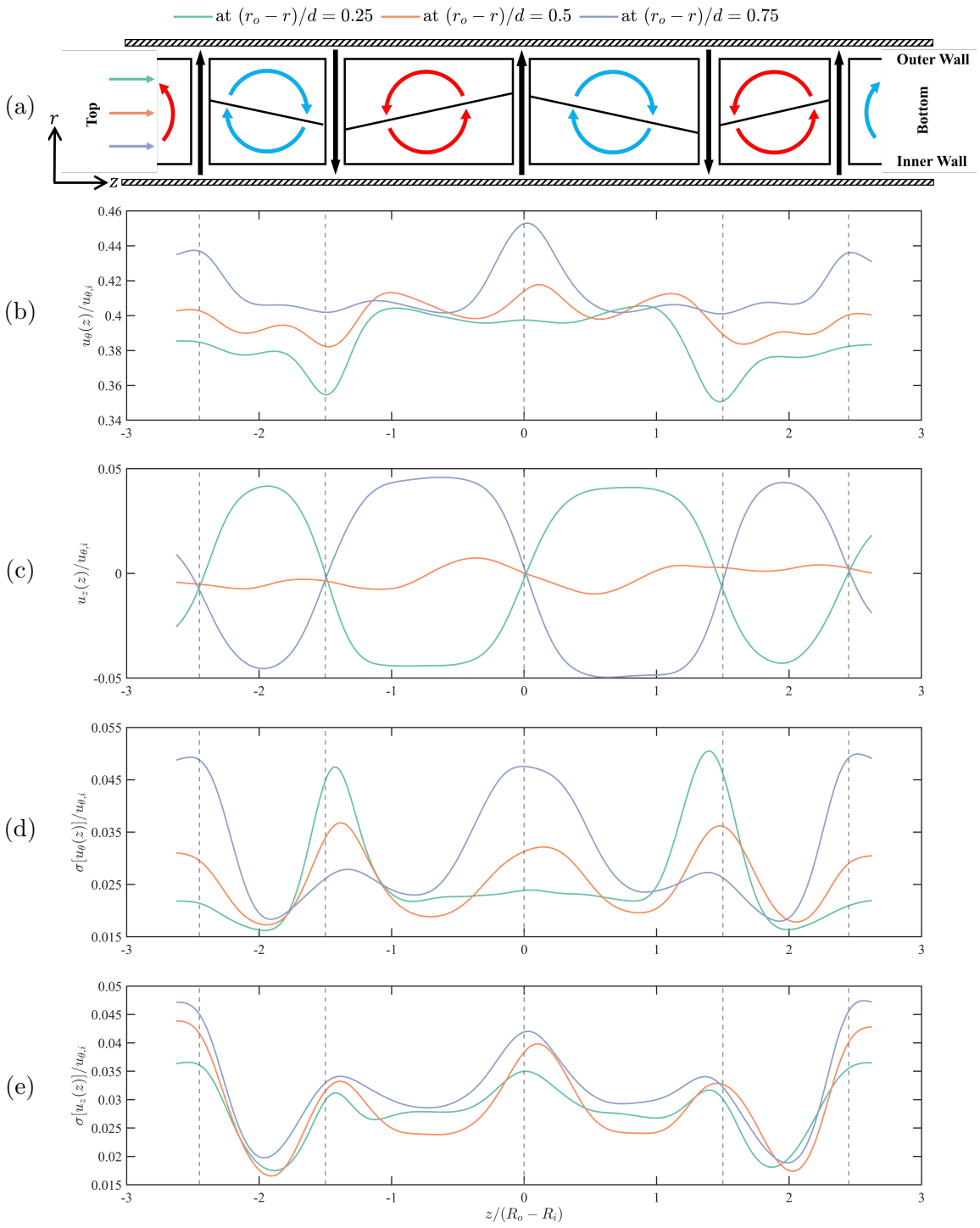

Figure B.4: Non-Newtonian TTV with 0.1 wt.% Xanthan gum aqueous solution. $Re = 3600$. (a)Schematic diagram of the Taylor vortex in the $r - z$ plane. Axial profiles of (b) the azimuthal velocity component, (c) the axial velocity component, (d) the turbulence strength of the azimuthal velocity component, and (e) the turbulence strength of the axial velocity component.

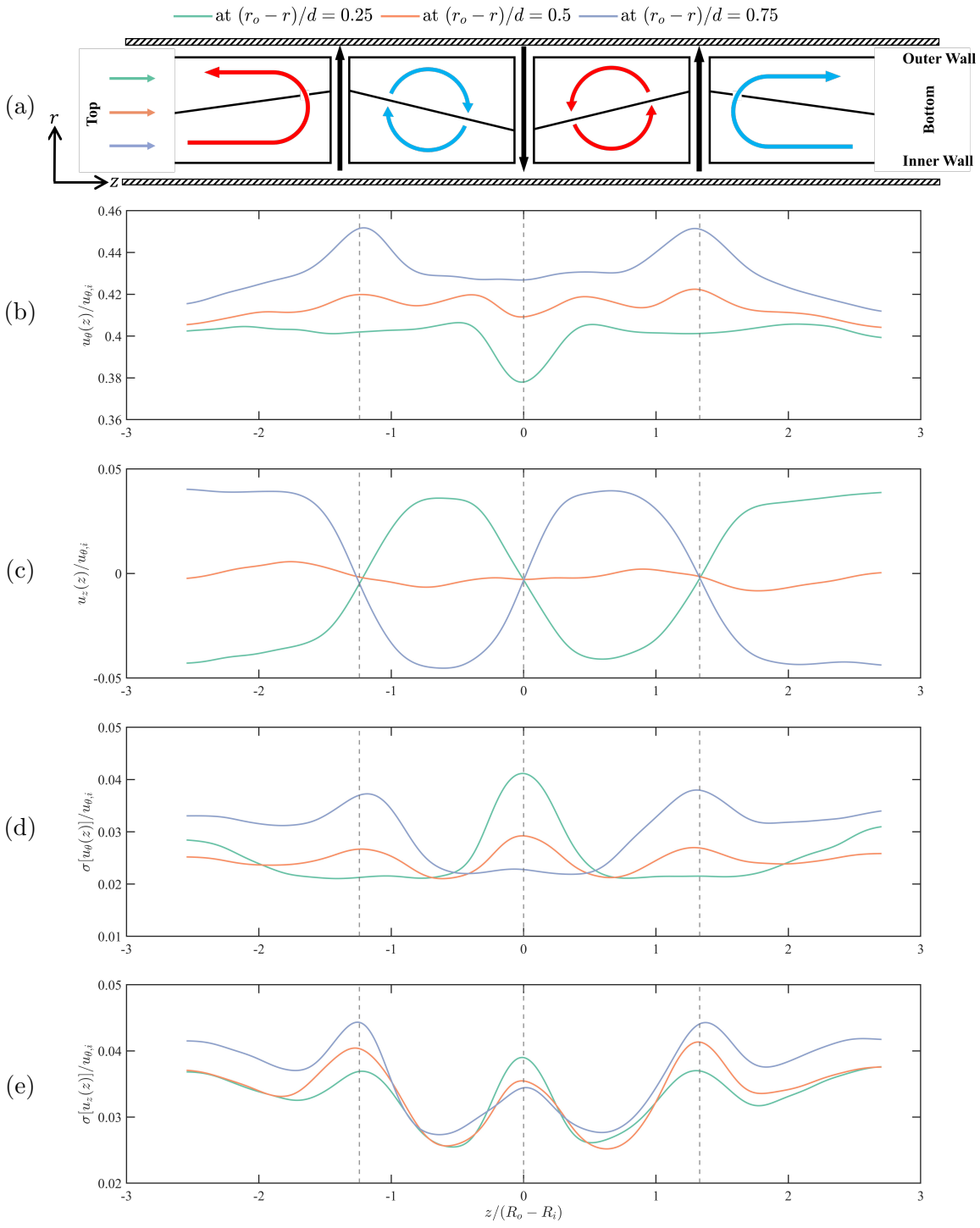

Figure B.5: Non-Newtonian TTV with 0.1 wt.% Xanthan gum aqueous solution. $Re = 6000$. (a)Schematic diagram of the Taylor vortex in the $r - z$ plane. Axial profiles of (b) the azimuthal velocity component, (c) the axial velocity component, (d) the turbulence strength of the azimuthal velocity component, and (e) the turbulence strength of the axial velocity component.

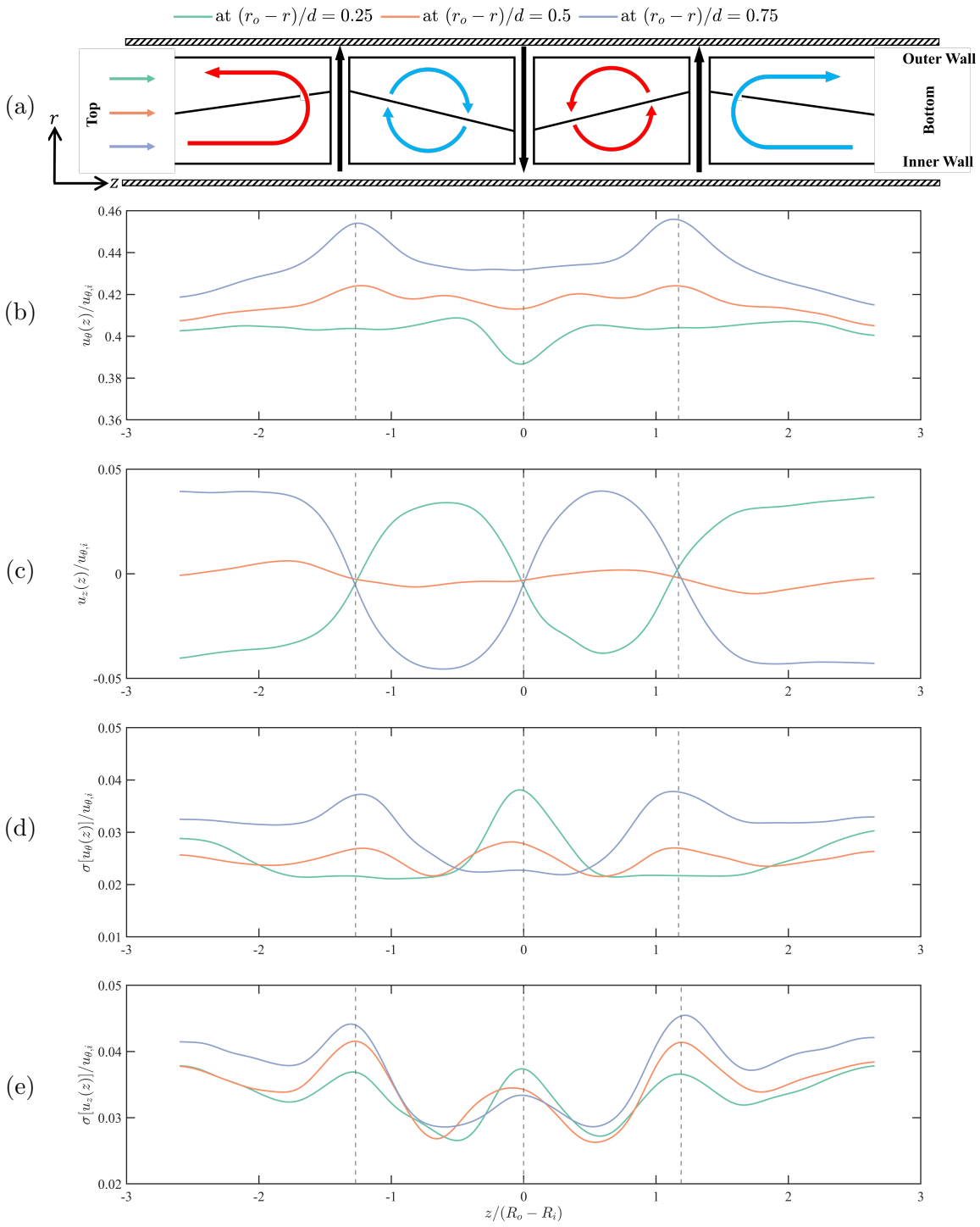

Figure B.6: Non-Newtonian TTV with 0.1 wt.% Xanthan gum aqueous solution. $Re = 7000$. (a)Schematic diagram of the Taylor vortex in the $r - z$ plane. Axial profiles of (b) the azimuthal velocity component, (c) the axial velocity component, (d) the turbulence strength of the azimuthal velocity component, and (e) the turbulence strength of the axial velocity component.

Appendix C: Matlab codes for data processing and plots

Some of the data processing scripts are attached in this appendix to briefly explain the main steps of data processing of this study.

Generally, the data processing includes five main steps:

1) Convert the measurement data form Excel sheet to .mat file, which is more accessible for Matlab to read data. Information of the traverse position should also be contained to produce profile plots later; 2) Process the data from LDV measurement. In this study, multiple times of measurements were conducted at every position. Therefore, data should be properly categorized to be processed together;

3) Piecewise polynomial fitting of the radial profiles. In this step, detailed adjustment of the piecewise polynomials had to be conducted manually to get satisfying fitting results. Once the expression of the velocity profile is obtained, the profiles of shear rate and viscosity would be accessible.

4) This script is mainly for plotting the radial profiles. With data provided by previous work, the templates of the plots should be carefully handled to present a consistent visual effect which includes fonts, size, color, figure aspect ratio and etc;

5) This script is mainly for plotting the axial profiles. Similarly, the template should be consistent for figures of the same type.

C.1 Read data and convert

Listing C.1: Read the measurement data from Excel sheet and convert into .mat with corresponding traverse position labeled

```
clear

listing = dir('*.xlsx')

for i = 1:length(listing)


% Read data and traverse step info

filename = listing(i).name
%% Input and record position info


opts = spreadsheetImportOptions("NumVariables", 1);
% Specify sheet and range
opts.Sheet = "BSA Header";
opts.DataRange = "E4:E4";  % For varied radial position, data range should be at D4:
    D4.

% Specify column names and types
```

```
opts.VariableNames = "VarName3";
opts.VariableTypes = "string";

% Import the data
Untitled = readtable(filename,opts)

Position = str2double(extractBefore(Untitled.(1)," mm"))

%Clear temporary opts
clear opts
%% Input measurement data
% u_z
% Set up the Import Options and import the data

opts = spreadsheetImportOptions("NumVariables", 3);

% Specify sheet and range
opts.Sheet = "Group 1";
opts.DataRange = "A2";

% Specify column names and types
opts.VariableNames = ["ArrivalTimems", "TransitTimes", "VelocityUms"];
opts.VariableTypes = ["double", "double", "double"];

% Specify file level properties
opts.MissingRule = "omitrow";

% Specify variable properties
opts = setvaropts(opts, ["ArrivalTimems", "TransitTimes", "VelocityUms"], "
    TreatAsMissing", '');

% Import the data
u_z = readtable(filename, opts, "UseExcel", false);
% Convert to output type

u_z = table2array(u_z)

%Clear temporary opts
clear opts

% u_phi
% Set up the Import Options and import the data

opts = spreadsheetImportOptions("NumVariables", 3);

% Specify sheet and range
opts.Sheet = "Group 2";
opts.DataRange = "A2";

% Specify column names and types
opts.VariableNames = ["ArrivalTime2ms", "TransitTime2s", "VelocityVPDA2ms"];
opts.VariableTypes = ["double", "double", "double"];

% Specify file level properties
opts.MissingRule = "omitrow";

% Specify variable properties
opts = setvaropts(opts, ["ArrivalTime2ms", "TransitTime2s", "VelocityVPDA2ms"], "
    TreatAsMissing", '');

% Import the data
u_phi = readtable(filename, opts, "UseExcel", false);
% Convert to output type

u_phi = table2array(u_phi)

%Clear temporary opts
clear opts
```

```
%% Remove outliers

% Remove outlier by mean of u_z
    TF = isoutlier(u_z(:,3),"mean")
    u_z([TF],:) = []

% Remove outlier by mean of u_r
    TF = isoutlier(u_phi(:,3),"mean")
    u_phi([TF],:) = []

%% Save with position info in file name
Name = sprintf('Radial_%.2fmm.mat',Position)

save (Name,"Position","u_phi","u_z")

end
```

C.2 Data averaging from multiple runs of measurement

Listing C.2: Get the average value and standard deviation of the measurement data and label them with corresponding traverse position

```
clear

%% Read data
FilesName = dir('*mm*.mat')

MeanVel = zeros(numel(FilesName),4)
u_i = 1 % m/s % Inner cylinder velocity

for i= 1:numel(FilesName)
    load(FilesName(i).name)

    MeanVel(i,1) = Position; % First row index by stepinfo
    MeanVel(i,2) = mean(u_phi(:,3)) % Calculate mean value
    MeanVel(i,3) = mean(u_z(:,3))
    MeanVel(i,4) = std(u_phi(:,3))
    MeanVel(i,5) = std(u_z(:,3)) %standartd deviation

    MeanVel_Reci(i,1) = Position; % First row index by stepinfo
    MeanVel_Reci(i,2) = 1/sum(1./u_phi(:,3)) % Calculate mean value
    MeanVel_Reci(i,3) = 1/sum(1./u_z(:,3))
    MeanVel_Reci(i,4) = sum((u_phi(:,3)-MeanVel_Reci(i,2))^2./u_phi(:,3))/sum(1./
        u_phi(:,3))
    MeanVel_Reci(i,5) = std(u_z(:,3)) %standartd deviation

    MeanVel(i,1) = Position; % First row index by stepinfo
    TT = sum(u_phi())
    MeanVel(i,2) =
    MeanVel(i,3) = mean(u_z(:,3))
    MeanVel(i,4) = std(u_phi(:,3))
    MeanVel(i,5) = std(u_z(:,3)) %standartd deviation
end

MeanVel(:,2) = -MeanVel(:,2) % Correct negetive value from LDV
MeanVel = sortrows(MeanVel)

%% Save averaged mean value with corresponding position of every run
save("Radial_Run7","MeanVel")
```

C.3 Piecewise polynomial fitting of the radial profiles

Listing C.3: Get the piecewise polynomial fitting of the radial profiles and save the results into .mat file

```
clear

colorOrder = get(gca,'ColorOrder')

listing = dir('*.mat') % Read data from files
%% Define fig obj
Omega_RadialPosition = figure;
StrainRate_RadialPosition = figure;
StrainRateFitting_RadialPosition = figure;
StrainRate_Smo_RadialPosition = figure;
%%
LegendName = strings([1,7]);
%%
% Setting of piecewise connection point
% Detailed adjustment of the connection point between adjacent piecewise
% plynomial acooerding to the shape of curve is necessary to get proper fitting
ConnectionPoint = [];
%%
for ii = 1:length(listing)
    FileName = listing(ii).name;
    load(FileName)

    RPM = str2double(extractBetween(FileName,"RPM","_Radial"));
    u_phi_i = (RPM)*pi*0.060325/30; % Calculate the inner cylinder speed m/s
    Omega_i = (RPM)*pi/30;
    LegendName(ii) = sprintf('%d',RPM2Re('Gly',RPM))

%%
% Judgement of Figure start point & interpolate with equal spaced interval

    RefraCorMatrix = Correct(Position);

    Cut_uphi_position = Position;
    Cut_x = find(0.21<Position&Position<12.91); % Discard points where measurement
        volume partialy in wall

    Interp_x = min(RefraCorMatrix(Cut_x,1)):0.01:max(RefraCorMatrix(Cut_x,1));
    Omega = u_phi_Mean(Cut_x,1)./((79.375-RefraCorMatrix(Cut_x,1))*1e-3);

    Interp_Omega = spline(RefraCorMatrix(Cut_x,1),Omega,Interp_x);
%%
% Cut the interpolated curve

    Start_1st = 0.21; % In traverse position fixed
    End_1st = ConnectionPoint(ii,1);

    Start_2nd = ConnectionPoint(ii,2);
    End_2nd = ConnectionPoint(ii,3);

    Start_3rd = ConnectionPoint(ii,4);
    End_3rd = 19.05;

    Cut_x_1st = find(Start_1st<Interp_x&Interp_x<End_1st) %First part of curve
    Cut_x_2nd = find(Start_2nd<Interp_x&Interp_x<End_2nd) %Outer Middle part of curve
    Cut_x_3rd = find(Start_3rd<Interp_x&Interp_x<End_3rd) %Inner middle part
%% Polynomial fitting

    C1_x = round(0.5*(End_1st+Start_2nd),2);
```

```
    C2_x = round(0.5*(End_2nd+Start_3rd),2); % Choice of 3 connection points for
        constraints

% outer middle part fitting

    Fit_Omega_2nd = polyfix(Interp_x(Cut_x_2nd),Interp_Omega(Cut_x_2nd),3, ...
                            [],[], ...
                            [],[])
% near outer wall part

    Value_c1 = polyval(Fit_Omega_2nd,C1_x) % Same value @ 1st connetion point
    Fit_Omega_1st = polyfix(Interp_x(Cut_x_1st),Interp_Omega(Cut_x_1st),5, ...
                            [0 C1_x], [0 Value_c1])
%
% near inner wall part

     Value_c2 = polyval(Fit_Omega_2nd,C2_x) % Same value @ 1st connetion point
     Fit_Omega_3rd = polyfix(Interp_x(Cut_x_3rd),Interp_Omega(Cut_x_3rd),5, ...
                            [C2_x 19.05],[Value_c2 Omega_i], ...
                            [],[])
    % u_phi(r) (m/s) = f(r) [r is mm]

%%
% Spline connection

Spline_Constraint = []
Spline_Constraint(1,:) = [polyval(Fit_Omega_2nd,ConnectionPoint(ii,1))
                          polyval(Fit_Omega_1st,ConnectionPoint(ii,2))
                          polyval(Fit_Omega_3rd,ConnectionPoint(ii,3))
                          polyval(Fit_Omega_2nd,ConnectionPoint(ii,4))]

Spline_Constraint(2,:) = [polyval(polyder(Fit_Omega_2nd),ConnectionPoint(ii,1))
                          polyval(polyder(Fit_Omega_1st),ConnectionPoint(ii,2))
                          polyval(polyder(Fit_Omega_3rd),ConnectionPoint(ii,3))
                          polyval(polyder(Fit_Omega_2nd),ConnectionPoint(ii,4))]

Spline_Constraint(3,:) = [polyval(polyder(polyder(Fit_Omega_2nd)),ConnectionPoint(ii
    ,1))
                          polyval(polyder(polyder(Fit_Omega_1st)),ConnectionPoint(ii
                              ,2))
                          polyval(polyder(polyder(Fit_Omega_3rd)),ConnectionPoint(ii
                              ,3))
                          polyval(polyder(polyder(Fit_Omega_2nd)),ConnectionPoint(ii
                              ,4))]

Spline_Constraint(4,:) =log10(Spline_Constraint(2,:))
Spline_Constraint(5,:) = Spline_Constraint(3,:)./(Spline_Constraint(2,:)*log(10))

Spline_Seg_1st = spline([ConnectionPoint(ii,2) ConnectionPoint(ii,1)], ...
                        [Spline_Constraint(2,2) ...
                         Spline_Constraint(1,[2 1]) ...
                         Spline_Constraint(2,1)])
Spline_Seg_2nd = spline([ConnectionPoint(ii,4) ConnectionPoint(ii,3)], ...
                        [Spline_Constraint(2,4) ...
                         Spline_Constraint(1,[4 3]) ...
                         Spline_Constraint(2,3)])

Spline_Seg_3rd = spline([ConnectionPoint(ii,2) ConnectionPoint(ii,1)], ...
                        [Spline_Constraint(5,2) ...
                         Spline_Constraint(4,[2 1]) ...
                         Spline_Constraint(5,1)])
Spline_Seg_4th = spline([ConnectionPoint(ii,4) ConnectionPoint(ii,3)], ...
                        [Spline_Constraint(5,4) ...
                         Spline_Constraint(4,[4 3]) ...
                         Spline_Constraint(5,3)])

% Combine piecewise polynomial function
```

```
 pp = 0.001;
    Fit_x_1st = 0:pp:(ConnectionPoint(ii,2)-pp);
    Fit_y_1st = polyval(Fit_Omega_1st,Fit_x_1st);

    Fit_x_2nd = ConnectionPoint(ii,2):pp:(ConnectionPoint(ii,1)-pp);
    Fit_y_2nd = ppval(Spline_Seg_1st,Fit_x_2nd);

    Fit_x_3rd = ConnectionPoint(ii,1):pp:(ConnectionPoint(ii,4)-pp);
    Fit_y_3rd = polyval(Fit_Omega_2nd,Fit_x_3rd);

    Fit_x_4th = ConnectionPoint(ii,4):pp:(ConnectionPoint(ii,3)-pp);
    Fit_y_4th = ppval(Spline_Seg_2nd,Fit_x_4th);

    Fit_x_5th = ConnectionPoint(ii,3):pp:19.05;
    Fit_y_5th = polyval(Fit_Omega_3rd,Fit_x_5th);

    Fit_x = [Fit_x_1st Fit_x_2nd Fit_x_3rd Fit_x_4th Fit_x_5th]
    Fit_omega = [Fit_y_1st Fit_y_2nd Fit_y_3rd Fit_y_4th Fit_y_5th]

    Fit_yy_1st = log10(polyval(polyder(Fit_Omega_1st),Fit_x_1st))
    Fit_yy_2nd = ppval(Spline_Seg_3rd,Fit_x_2nd);
    Fit_yy_3rd = log10(polyval(polyder(Fit_Omega_2nd),Fit_x_3rd));
    Fit_yy_4th = ppval(Spline_Seg_4th,Fit_x_4th);
    Fit_yy_5th = log10(polyval(polyder(Fit_Omega_3rd),Fit_x_5th));

    Fit_Strain = [Fit_yy_1st Fit_yy_2nd Fit_yy_3rd Fit_yy_4th Fit_yy_5th]
    Fit_Strain = Fit_Strain +log10(79.375-Fit_x)

figure(Omega_RadialPosition)
    Exp=plot(RefraCorMatrix(Cut_x,1),Omega, 'o',...
           'DisplayName',strcat('\itExp of Re\rm ', LegendName(ii)), ...
           'LineWidth',1, ...
           "Color",colorOrder(ii,:))
    hold on
    Fitting = plot(Fit_x/Fit_x(end),Fit_omega/Omega_i, ...
                  'DisplayName',strcat('\itFitting of Re\rm ', LegendName(ii)), ...
                  'LineWidth',1.25, ...
                  "Color",colorOrder(ii,:))
    hold on

figure(StrainRate_RadialPosition)
fig = plot(Fit_x,Fit_Strain,"Color",colorOrder(ii,:), ...
                            'LineWidth',1.5, ...
                            'DisplayName',strcat('\itRe \rm ', LegendName(ii)))
    hold on
%%

    Deri_strain_Smo = polyfit(Fit_x,Fit_Strain,9) % Polynomial fitting with log10 of
        strain
    figure(StrainRateFitting_RadialPosition)
    Fitting_StrainRate = plot(Fit_x,polyval(Deri_strain_Smo,Fit_x).*NaN, ...
                           'o','LineWidth',1.5, ...
                           'DisplayName',strcat('Re = ', LegendName(ii)), ...
                           "Color",colorOrder(ii,:))
    hold on

%%
% Store the strain rate data

    Deri_strain_Smo = polyval(Deri_strain_Smo,Fit_x)
    Name = sprintf('Re_%d_RPM_%d_Sandwich',str2num(LegendName(ii)),RPM)
    save(Name,'Fit_x','Fit_omega','Deri_strain_Smo','Fit_Strain','RPM')
end

load LaminarTheoratical.mat % This file contains data of the profiles of basic
    maminar TC flow

figure(Omega_RadialPosition);
```

```
plot(r_prime,NonNewt_Nor_Omega(:,3),'--','LineWidth',1.25,'Color','#686868', ...
    "DisplayName","Laminar")
lgd1 = legend('Location',"northeastoutside",'Box',"off")
pbaspect([4 3 1])
% axis padded
%lgd1.NumColumns = 2;
%lgd1.Title.String = '\itRe\rm'
ylim([0 1])
xlabel('$r^\prime=(R_o-r)/(R_o-R_i)$','Interpreter','latex')
ylabel('$\bar{\omega}_\theta/\omega_{\theta,i}$','Interpreter','latex')
% xlabel('\its\rm (mm)')
% ylabel('\it\omega\rm rad/s')
set(gca, 'FontName', 'Times New Roman')
set(gca,'FontSize',12)

figure(StrainRate_RadialPosition);
% lgd2 = legend('Location',"northeastoutside",'Box',"off")
pbaspect([4 3 1])
axis padded
%lgd1.NumColumns = 2;
%lgd1.Title.String = '\itRe\rm'
xlabel('\its\rm (mm)')
ylabel('log_{10}\it\gamma^\prime\rm (/s)')
set(gca, 'FontName', 'Times New Roman')
set(gca,'FontSize',12)

figure(StrainRate_Smo_RadialPosition);
lgd3 = legend('Location',"northeastoutside",'Box',"off")
pbaspect([4 3 1])
%lgd1.NumColumns = 2;
%lgd1.Title.String = '\itRe\rm'
axis padded
xlabel('\its\rm (mm)')
ylabel('shear strain rate log_{10}\it\gamma^\prime\rm (/s)')
set(gca, 'FontName', 'Times New Roman')
set(gca,'FontSize',12)
```

C.4 Plotting radial profiles

Listing C.4: Plot the radial profiles on the basis of the previous .mat file

```
clear

colorOrder = get(gca,'ColorOrder')

Miu_RadialPosition = figure
Miu_RadialPosition_Log = figure
Stress_RadialPosotion_Ref = figure
Stress_RadialPosotion_Log = figure
ShearRate_RadialPosition = figure
ShearRate_RadialPosition_Ref = figure
Re_Gl_RadialPosotion = figure
Re_GltoRe_G_RadialPosotion = figure

LegendName = strings([1,7]);
Re_G = zeros(7,2)
%%
listing = dir('*Re_*_Sandwich*.mat') % Read

% miu_zero = 0.08635;
% miu_inf = 0.004981;
% m = 0.3508;
% n = 0.7032;
```

```
Densisty = 1169.9
R_o = 79.375*1e-3
R_i = 60.325*1e-3
d = R_o - R_i

for ii = 1:length(listing)
    FileName = listing(ii).name;
    load(FileName)
    LegendName(ii) = sprintf('%d',RPM2Re('Gly',RPM))

    ShearRate_ref = (RPM)*pi*0.060325/30/d
    Miu = 0.0296;
    Stress_ref = ShearRate_ref*Miu;
    Re(ii) = Densisty*(RPM)*pi*0.060325/30*d/Miu

%
%     Miu = (miu_zero-miu_inf)./...
%       (1+(m.*(10.^Fit_Strain)).^n)+miu_inf; % Fit_Strain is log10 of strain
%
    Stress_thetar = Miu.*(10.^Fit_Strain);

    figure(ShearRate_RadialPosition)
    Exp=semilogy(Fit_x/Fit_x(end),(10.^Fit_Strain/(10.^(Fit_Strain(end)))),...
           'DisplayName',strcat('\itRe\rm ', LegendName(ii)), ...
           'LineWidth',1.5, ...
           "Color",colorOrder(ii,:))
    hold on

    figure(ShearRate_RadialPosition_Ref)
    Exp=semilogy(Fit_x/Fit_x(end),(10.^Fit_Strain/ShearRate_ref),...
           'DisplayName',strcat('\itRe\rm ', LegendName(ii)), ...
           'LineWidth',1.5, ...
           "Color",colorOrder(ii,:))
    hold on

%     figure(Miu_RadialPosition)
%     Exp=plot(Fit_x/Fit_x(end),Miu/Miu(end),...
%            'DisplayName',strcat('\itRe\rm ', LegendName(ii)), ...
%            'LineWidth',1, ...
%            "Color",colorOrder(ii,:))
%     hold on
%
%     figure(Miu_RadialPosition_Log)
%     Exp=semilogy(Fit_x/Fit_x(end),Miu/Miu(end),...
%            'DisplayName',strcat('\itRe\rm ', LegendName(ii)), ...
%            'LineWidth',1, ...
%            "Color",colorOrder(ii,:))
%     hold on



    figure(Stress_RadialPosotion_Log)
    Exp=semilogy(Fit_x/Fit_x(end),Stress_thetar/Stress_thetar(end),...
           'DisplayName',strcat('\itRe\rm ', LegendName(ii)), ...
           'LineWidth',1.5, ...
           "Color",colorOrder(ii,:))
    hold on

    figure(Stress_RadialPosotion_Ref)
    Exp=semilogy(Fit_x/Fit_x(end),Stress_thetar/Stress_ref,...
           'DisplayName',strcat('\itRe\rm ', LegendName(ii)), ...
           'LineWidth',1.5, ...
           "Color",colorOrder(ii,:))
    hold on
%%
% Re_Gl & Re_G

    Re_Gl = Fit_omega.*(79.375-Fit_x)*1e-3./Miu*Densisty*(R_o-R_i)
```

```
    % no Lack the coefficient density&length

    Re_G(ii,1) = trapz(Fit_x*1e-3,Re_Gl.*(79.375-Fit_x)*1e-3)...
                 *2/(R_o^2-R_i^2)
    %1st row for integrated value of lack Re_Gl*r

    Re_G(ii,2) = trapz(Fit_x*1e-3,Miu.*(79.375-Fit_x)*1e-3)...
                 *2/(R_o^2-R_i^2)
    %2nd row for integrated value of density miu*r

    figure(Re_Gl_RadialPosotion)
    Exp=plot(Fit_x/Fit_x(end),Re_Gl/Re_Gl(end),...
           'DisplayName',strcat('\itRe\rm ', LegendName(ii)), ...
           'LineWidth',1.5, ...
           "Color",colorOrder(ii,:))
    hold on

    figure(Re_GltoRe_G_RadialPosotion)
    Exp=plot(Fit_x/Fit_x(end),Re_Gl/Re_G(ii,1),...
           'DisplayName',strcat('\itRe\rm ', LegendName(ii)), ...
           'LineWidth',1.5, ...
           "Color",colorOrder(ii,:))
    hold on

end

load LaminarTheoratical.mat

figure(ShearRate_RadialPosition);
% plot(r_prime,NonNewt_Nor_ShearRate(:,3),'--','LineWidth',1.25,'Color','#686868',
    ...
%     "DisplayName","Laminar")
% lgd1 = legend('Location',"northeastoutside",'Box',"off")
pbaspect([4 3 1])
axis padded
%lgd1.NumColumns = 2;
%lgd1.Title.String = '\itRe\rm'
xlabel('$r^\prime=(R_o-r)/(R_o-R_i)$','Interpreter','latex')
ylabel('$\bar{\dot{\gamma}}_{\theta r}(r)/\dot{\gamma}_{\theta r,i}$','Interpreter','
    latex')
set(gca, 'FontName', 'Times New Roman')
set(gca,'FontSize',12)

figure(ShearRate_RadialPosition_Ref);
plot(r_prime,NonNewt_Nor_ShearRate(:,3),'--','LineWidth',1.25,'Color','#686868', ...
    "DisplayName","Laminar")
% lgd1 = legend('Location',"northeastoutside",'Box',"off")
pbaspect([4 3 1])
axis padded
%lgd1.NumColumns = 2;
%lgd1.Title.String = '\itRe\rm'
xlabel('$r^\prime=(R_o-r)/(R_o-R_i)$','Interpreter','latex')
ylabel('$\bar{\dot{\gamma}}_{\theta r}(r)/\dot{\gamma}_{\theta r,ref}$','Interpreter'
    ,'latex')
set(gca, 'FontName', 'Times New Roman')
set(gca,'FontSize',12)

% figure(Miu_RadialPosition);
% plot(r_prime,Nor_Miu(:,2),'--','LineWidth',1.25,'Color','#686868', ...
%     "DisplayName","Laminar")
%
% lgd1 = legend('Location',"northeastoutside",'Box',"off")
% pbaspect([4 3 1])
% % axis padded
% %lgd1.NumColumns = 2;
% %lgd1.Title.String = '\itRe\rm'
% xlabel('$r^\prime=(R_o-r)/(R_o-R_i)$','Interpreter','latex')
% ylabel('${\mu_\theta}^\prime=\mu_\theta(r)/\mu_{\theta,i}$','Interpreter','latex')
```

```
% set(gca, 'FontName', 'Times New Roman')
% set(gca,'FontSize',12)

figure(Stress_RadialPosotion_Ref);
% plot(r_prime,Nor_Stress(:,3),'--','LineWidth',1.25,'Color','#686868', ...
%     "DisplayName","Laminar")
%
% lgd1 = legend('Location',"northeastoutside",'Box',"off")
pbaspect([4 3 1])
axis padded
%lgd1.NumColumns = 2;
%lgd1.Title.String = '\itRe\rm'
xlabel('$r^\prime=(R_o-r)/(R_o-R_i)$','Interpreter','latex')
ylabel('${\sigma_{\theta r}}^\prime=\sigma_{\theta r}/\sigma_{\theta r,ref}$','
    Interpreter','latex')
%ylabel('\it\sigma\rm (pa)')
set(gca, 'FontName', 'Times New Roman')
set(gca,'FontSize',12)

% figure(Miu_RadialPosition_Log);
% plot(r_prime,Nor_Miu(:,2),'--','LineWidth',1.25,'Color','#686868', ...
%     "DisplayName","Laminar")
%
% lgd1 = legend('Location',"northeastoutside",'Box',"off")
% pbaspect([4 3 1])
% % axis padded
% %lgd1.NumColumns = 2;
% %lgd1.Title.String = '\itRe\rm'
% xlabel('$r^\prime=(R_o-r)/(R_o-R_i)$','Interpreter','latex')
% ylabel('${\mu_\theta}^\prime=\mu_\theta(r)/\mu_{\theta,i}$','Interpreter','latex')
% set(gca, 'FontName', 'Times New Roman')
% set(gca,'FontSize',12)

figure(Stress_RadialPosotion_Log);
plot(r_prime,Nor_Stress(:,3),'--','LineWidth',1.25,'Color','#686868', ...
    "DisplayName","Laminar")

% lgd1 = legend('Location',"northeastoutside",'Box',"off")
pbaspect([4 3 1])
axis padded
%lgd1.NumColumns = 2;
%lgd1.Title.String = '\itRe\rm'
xlabel('$r^\prime=(R_o-r)/(R_o-R_i)$','Interpreter','latex')
ylabel('${\sigma_{\theta r}}^\prime=\sigma_{\theta r}/\sigma_{\theta r,i}$','
    Interpreter','latex')
set(gca, 'FontName', 'Times New Roman')
set(gca,'FontSize',12)

figure(Re_Gl_RadialPosotion);
plot(r_prime,Nor_Re_l(:,3),'--','LineWidth',1.25,'Color','#686868', ...
    "DisplayName","Laminar")

% lgd1 = legend('Location',"northeastoutside",'Box',"off")
pbaspect([4 3 1])
% axis padded
%lgd1.NumColumns = 2;
%lgd1.Title.String = '\itRe\rm'
xlabel('$r^\prime=(R_o-r)/(R_o-R_i)$','Interpreter','latex')
ylabel('$Re_{G,l}/Re_{G,l,i}$','Interpreter','latex')
set(gca, 'FontName', 'Times New Roman')
set(gca,'FontSize',12)

figure(Re_GltoRe_G_RadialPosotion);
plot(r_prime,Re_l_Re_G(:,3),'--','LineWidth',1.25,'Color','#686868', ...
    "DisplayName","Laminar")

% lgd1 = legend('Location',"northeastoutside",'Box',"off")
pbaspect([4 3 1])
```

```
% axis padded
%lgd1.NumColumns = 2;
%lgd1.Title.String = '\itRe\rm'
xlabel('$r^\prime=(R_o-r)/(R_o-R_i)$','Interpreter','latex')
ylabel('$Re_{G,l}/Re_{G}$','Interpreter','latex')
set(gca, 'FontName', 'Times New Roman')
set(gca,'FontSize',12)
```

C.5 Plotting axial profiles

Listing C.5: Plot the axial profiles on the basis of the previous .mat file

```
clear all

listing = dir('*RPM660*.mat')

Nor_uphi_TraversePosition = figure;
Nor_uphi_Nor_Height = figure;
Nor_uz_Nor_Height = figure;
TS_uphi_Nor_Height = figure;
TS_uz_Nor_Height = figure;
TI_uphi_Nor_Height = figure;
TI_uz_Nor_Height = figure;

LegendName = strings([1,3]);
LegendName(1) = ('at \it r/(r_o-r_i)=0.25\rm')
LegendName(2) = ('at \it r/(r_o-r_i)=0.5\rm')
LegendName(3) = ('at \it r/(r_o-r_i)=0.75\rm')

IterpStep = 0.2
%%
for ii = 1:length(listing)
    FileName = listing(ii).name;
    load(FileName) % Read data file

    RPM = str2double(extractBetween(FileName,"RPM","_Mid")); % Get RPM info from file
        name
    u_phi_i = (RPM+2)*pi*0.060325/30; % Calculate the inner cylinder speed m/s
    Position = u_phi_Comb_Mean(:,1)
    xq = min(Position):IterpStep:max(Position)
    Interp_Data(:,1) = -interp1(Position,u_phi_Comb_Mean(:,2),xq)
    Interp_Data(:,2) = interp1(Position,u_z_Comb_Mean(:,2),xq)
    Interp_Data(:,3) = interp1(Position,u_phi_Comb_Mean(:,3),xq)
    Interp_Data(:,4) = interp1(Position,u_z_Comb_Mean(:,3),xq)

    Smooth_Data = smoothdata(Interp_Data,1,'sgolay',250)
    xq = xq

%%
 figure(Nor_uphi_TraversePosition)

    plot(xq,Interp_Data(:,1)/u_phi_i, ...
        'DisplayName', LegendName(ii), ...
         'LineWidth',1.5)
    hold on

%%
    figure(Nor_uphi_Nor_Height)

    h=plot(xq/19.05, ...
         Smooth_Data(:,1)/u_phi_i, ...
         'DisplayName',LegendName(ii), ...
         'LineWidth',1.5)
    % normalized u_phi and normalized height
```

```
    hold on
%%
    figure(Nor_uz_Nor_Height)
    h=plot(xq/19.05, ...
        Smooth_Data(:,2)/u_phi_i,...
        'DisplayName',LegendName(ii), ...
        'LineWidth',1.5)
    hold on
%%
    figure(TS_uphi_Nor_Height)
    plot(xq/19.05, ...
        Smooth_Data(:,3)/u_phi_i, ...
        'DisplayName',LegendName(ii), ...
        'LineWidth',1.5)
%TS normalized by uphi_i
    hold on
%%
    figure(TS_uz_Nor_Height)
    plot(xq/19.05, ...
        Smooth_Data(:,4)/u_phi_i,...
        'DisplayName',LegendName(ii), ...
        'LineWidth',1.5)
    hold on

end

figure(Nor_uphi_TraversePosition);
xlabel('\ith\rm (mm)')
ylabel('\itu_{\phi}^\prime=u_{\phi} /u_i\rm')
legend('Interpreter','latex')
set(gca, 'FontName', 'Times New Roman')
set(gca,'FontSize',12)

figure(Nor_uphi_Nor_Height);
% ylim([0.3 0.51])
xlabel('$h/(R_o-R_i)$','Interpreter','latex')
ylabel('$u_\theta(h)/u_{\theta,i}$','Interpreter','latex')
set(gca, 'FontName', 'Times New Roman')
set(gca,'FontSize',12)
Nor_uphi_Nor_Height.Position(3:4) = [36 9]*40
% xline(DashedLines,'--','Color',[105,105,105]/255,'LineWidth',1.25)

figure(Nor_uz_Nor_Height);
xlabel('$h/(R_o-R_i)$','Interpreter','latex')
ylabel('$u_z(h)/u_{\theta,i}$','Interpreter','latex')
set(gca, 'FontName', 'Times New Roman')
set(gca,'FontSize',12)
Nor_uz_Nor_Height.Position(3:4) = [36 9]*40
% xline(DashedLines,'--','Color',[105,105,105]/255,'LineWidth',1.25)

figure(TS_uphi_Nor_Height);
xlabel('$h/(R_o-R_i)$','Interpreter','latex')
ylabel('$\sigma(u_{\theta})/u_{\theta,i}$','Interpreter','latex')
set(gca, 'FontName', 'Times New Roman')
set(gca,'FontSize',12)
TS_uphi_Nor_Height.Position(3:4) = [36 9]*40
% xline(DashedLines,'--','Color',[105,105,105]/255,'LineWidth',1.25)

figure(TS_uz_Nor_Height);
xlabel('$h/(R_o-R_i)$','Interpreter','latex')
ylabel('$\sigma(u_{z})/u_{\theta,i}$','Interpreter','latex')
set(gca, 'FontName', 'Times New Roman')
set(gca,'FontSize',12)
TS_uz_Nor_Height.Position(3:4) = [36 9]*40
% xline(DashedLines,'--','Color',[105,105,105]/255,'LineWidth',1.25)

figure(TI_uphi_Nor_Height);
xlabel('\ith/(r_o-r_i )\rm')
```

```
ylabel('\it\sigma(u_{\phi})/u_{\phi}(h)\rm')
set(gca, 'FontName', 'Times New Roman')
set(gca,'FontSize',12)

figure(TI_uz_Nor_Height);
xlabel('$\mathit{h/(r_o-r_i)}$','Interpreter','latex')
ylabel('$\mathit{\sigma(u_z)/u_z(h)}$','Interpreter','latex')
set(gca, 'FontName', 'Times New Roman')
set(gca,'FontSize',12)
```